# Enhancement of the Thermoelectric Power of TAGS-85 by Distortion of the Electronic Density of States

Safdar Abbas Malik

university of groningen / faculty of mathematics and natural sciences / zernike institute for advanced materials

# Enhancement of the Thermoelectric Power of TAGS-85 by Distortion of the Electronic Density of States

**Safdar Abbas Malik**

*Supervised by*

Dr. Graeme Blake

*Referee*

Dr. Ron Tobey

Solid State Materials for Electronics group

Zernike Institute for Advanced Materials

Faculty of Mathematics and Natural Sciences

University of Groningen

The work described in this thesis was carried out between September 2013 and July 2014 as part of the Top Master Programme in Nanoscience and was performed in the research group Solid State Materials for Electronics, part of the Zernike Institute for Advanced Materials, at the University of Groningen.

Cover:

Image description: Colorado River in the Grand Canyon, Arizona.

Relevance: Resonant levels are like rocks in the river; they trap carriers and enhance the resistivity. But, they are not merely dead rocks - a fountain within - they also provide high energy carriers near the Fermi level and enhance the Seebeck coefficient.

Image courtesy: National Geographic

*To Maria*

# Foreword

Recently, thermoelectric materials have attracted a great deal of attention because of the increasing demands for alternative energy resources and novel energy conversion techniques. The performance of a thermoelectric material is determined by a set of inter-related material properties and the core challenge for the present research in this field is to optimize the conflicts between these properties. The efficiency of a thermoelectric device is characterized by the thermoelectric figure of merit, ZT, which is a function of the electrical and thermal conductivities and the Seebeck coefficient of the material. The ZT value of the current state-of-the-art thermoelectric materials lies close to unity and the aim is to raise this value above 2. In the past decade, considerable advances have been made by reducing the lattice thermal conductivity with the help of structural complexity but in most materials, the amorphous limit has been reached, i.e. the phonon mean free path can not become shorter than the lattice parameter. Relatively less attention has been paid to the electronic part of the figure of merit, more importantly the Seebeck coefficient. Theory has predicted that there are possibilities of enhancing the Seebeck coefficient via a controlled distortion of the electronic density of states. Recently, some successful attempts have been reported.

TAGS-85 has been one of the most widely used thermoelectric materials since the 1960's. Lanthanides have been reported to distort the electronic density of states of some novel Kondo systems in a way desirable for thermoelectrics. The f-orbitals of these elements can be a potential perturbation to the electronic structure of the host materials. In this thesis the improvement of the thermoelectric response of the TAGS-85 system by doping with different concentrations of Holmium and Terbium is reported. In the first chapter, some basic concepts and an overview of the current state of the research has been presented. The second chapter covers a literature review of the TAGS-85 material system. In the third chapter, the synthesis and characterization techniques followed during this research have been described. In the fourth and the fifth chapters the results of the characterization are presented for TAGS-85 samples with different doping types. The sixth chapter contains the concluding remarks and the prospects for future research.

# Contents

Chapter-1

# Thermoelectricity

## 1.1 Introduction

Thermoelectricity is the phenomenon of heat conversion into electricity. When a temperature gradient is applied across a thermoelectric material, the mobile charge carriers diffuse from the hotter end to the colder end. This diffusion of charge carriers produces an electrostatic potential which prevents further diffusion when the equilibrium with the chemical potential is reached.

A schematic of the band diagram of an n-type semiconductor subjected to a temperature gradient is shown in figure 1.1. The concentration of electrons in an n-type semiconductor, n, is given as:

$$n = N_C \, Exp\left(\frac{E_F - E_C}{k_B T}\right) \quad (1.1)$$

and the concentration of holes in a p-type semiconductor, p, is:

$$p = N_V \, Exp\left(\frac{E_V - E_F}{k_B T}\right) \quad (1.2)$$

This implies

$$E_F - E_C = k_B T \ln (n/N_C) \quad (1.3)$$

$$E_V - E_F = k_B T \ln (p/N_V) \quad (1.4)$$

where $N_C$ is the density of states in the conduction band and $N_V$ is the density of states in the valence band. As T increases, the doping becomes less important than the thermal generation of carriers, the Fermi level, $E_F$, tends to the intrinsic Fermi level, $E_{in}$, i.e. a Fermi level gradient is induced due to the temperature gradient.

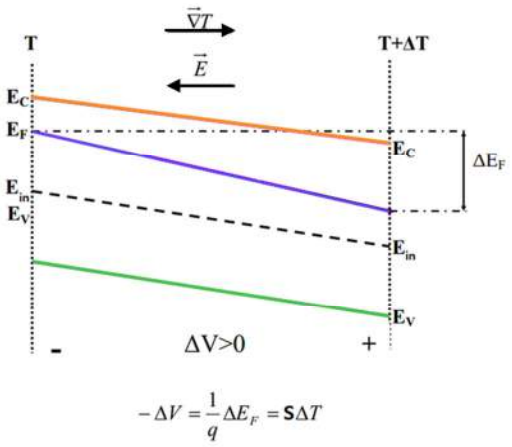


**Fig. 1.1.** Schematic band diagram of an n-type semiconductor with a temperature gradient. Adapted from Ref. [1].

For n-type material, S > 0, the induced electric field and the temperature gradient are in the same direction.

For p-type material, S < 0, the induced electric field and the temperature gradient are in opposite direction.

This effect was first observed by Seebeck [2] in 1823 when he observed the deflection of the compass placed in the vicinity of a closed loop made of two different conductors, when one end of the loop was heated. Seebeck studied this effect for a large number of materials and arranged his results in the order of the product Sσ, where S is the Seebeck coefficient which is usually expressed in the units of μV/K and σ is the electrical conductivity. About 12 years later, Peltier [3] observed a correlative effect where a temperature gradient was observed by application of voltage difference. In 1905 [4] and 1911 [5] Altenkirch gave a satisfactory theory of thermoelectric generation and refrigeration and concluded that the higher the Seebeck coefficient, S, and the electrical conductivity, σ, and the lower the thermal conductivity, k, the better is the thermoelectric performance of the material. He defined a parameter, called the figure of merit, Z, to quantify the thermoelectric performance of a material, defined as:

$$Z = S^2\sigma/k \tag{1.5}$$

A useful dimensionless figure of merit is ZT. Electrical part of the figure of merit is called the power factor, defined as $S^2\sigma$. The efficiency of a thermoelectric device is defined as [6]:

$$\eta = \frac{\text{Energy provided to the load}}{\text{Heat energy absorbed at the hot junction}} = \frac{\Delta T}{T_H}\frac{\sqrt{1+ZT}-1}{\sqrt{1+ZT}+\frac{T_C}{T_H}} \tag{1.6}$$

where $T_H$ is the temperature at the hotter end and $T_C$ is the temperature at the colder end, $\Delta T = T_H - T_C$ and 'ZT' is the dimensionless figure of merit [7]. The efficiency depends upon the temperature difference, ΔT, the temperature of operation, T, and the figure of merit, ZT. It is

the figure of merit that gives both the temperature depression and maximum coefficient of performance. Therefore, it is the large ZT value which is desirable for an efficient thermoelectric device.

Although Seebeck did most of his studies on semiconducting minerals, yet most of the research work till the early 1900's remained focused on metals and metal alloys, for which the ratio 'σ/k' is almost constant. Seebeck coefficient for most metals [8] is less than 10 μV/K with efficiency of the order of 1%. This created an impression that thermoelectricity was not very economical source of power generation. In 1940's, higher Seebeck coefficient values (~100 μV/K) were observed for semiconductors. Telks in 1947 reported [9] to have constructed a thermoelectric generator with an efficiency of 5%. Unluckily, semiconductors have a poor σ/k ratio because of poor electrical conductivity. In 1956, Ioffe et al. observed [10] that the ratio could be improved if the thermoelectric material is alloyed with an iso-morphous element or compound. Motivated by possible military applications, usefulness in the space missions and the need to cope with the energy crisis in the 1970's, the RCA Laboratories in the US and other military research institutions across the world started to work on this idea and discovered a few very useful semiconducting alloys with ZT approaching 1.5.

In the last decade, great progress has been made towards the improvement of the thermoelectric figure of merit, ZT. The core issue in this area of research is that the ZT comprises of a set of conflicting properties, i.e. the Seebeck coefficient and the electrical and thermal conductivities. Most of the mechanisms which improve one of them, recede the others. We can write:

$$ZT = S^2\sigma T/k = (S^2 n)(\mu/k)qT \qquad (1.7)$$

where 'q' denotes the charge of the carriers. The mechanisms that increase μ, the mobility of charge carriers, usually increase the k as well, similarly, the higher the carrier concentration, n, the lower the Seebeck coefficient, S.

However, a revival in the research came in 1990's when it was predicted theoretically that nanostructural engineering could enhance the thermoelectric efficiency [11]. The first generation of bulk thermoelectric materials was produced till a half century ago with ZT of 0.8-1.0 with a device efficiency of 5-6 %. The second generation that came with the idea of nano structuring, has ZT values about 1.3 to 1.7 with 11-15 % device efficiency. At present, the goal is to take the ZT value above 2, thereby making devices with efficiency higher than 20%.

## 1.2 The Inter-related Parameters

The basic challenge faced by the researchers in enhancement of the thermoelectric efficiency of a material is the need to optimize a series of conflicting material properties. Here we discuss each of them briefly:-

### 1.2.1 Carrier Concentration

Ideally, a thermoelectric material should have only one type of charge carriers, either electrons or holes. Mixed conduction would result in both electrons and holes diffusing from the hotter end to the colder end and canceling out the induced Seebeck voltage. Low carrier concentration, n, implies high Seebeck coefficient values, but it also results in low electrical conductivity, σ. The interdependence of the carrier concentration and the Seebeck coefficient can be seen by looking at relatively simple models of carrier transport. For metals, or degenerate semiconductors, the Seebeck coefficient is defined as:

$$S = \frac{dV}{dT} = \frac{8\pi^2 k_B^2}{3eh^2} m^* T \left(\frac{\pi}{3n}\right)^{2/3} \quad (1.8)$$

Here $m^*$ is the density-of-states effective mass. The electrical conductivity and the carrier concentration are related as:

$$\sigma = ne\mu \quad (1.9)$$

Figure 1.2 shows the compromise between the carrier concentration, Seebeck coefficient, electrical and thermal conductivities. The maximum figure of merit is observed at carrier concentration ranging from $10^{19}$ to $10^{21}$ carriers per $cm^3$, which falls between common metals and semiconductors, i.e. heavily doped semiconductors can be promising.

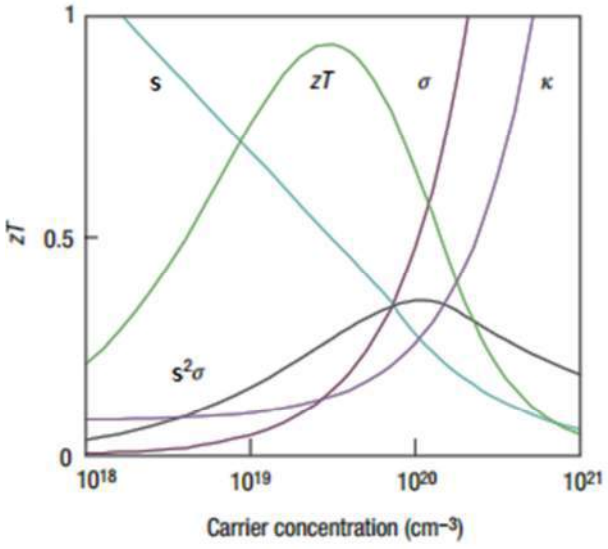


**Fig. 1.2.** Maxima in the figure of merit, ZT, appears as a compromise between the electrical conductivity (σ: 0 to 5000 $\Omega^{-1}cm^{-1}$), Seebeck coefficient (S: 0 to 500 μV/K) and thermal conductivity (k:

0 to 10 $Wm^{-1}K^{-1}$). Good thermoelectrics are typically heavily doped semiconductors with a carrier concentration between $10^{19}$ to $10^{21}$ carriers per $cm^3$. The trends shown were modeled from $Bi_2Te_3$, based on empirical data in ref. [12] by G. J. Snyder and E. S. Toberer. Image adapted from Ref. [6].

## 1.2.2 Thermal Conductivity

For a good thermoelectric material, thermal conductivity, k, should be low so as to increase the temperature difference between the hotter and the colder end. Thermal conductivity has two contributions: (1) electronic thermal conductivity ($k_e$) which comes from electrons (or holes), (2) lattice thermal conductivity ($k_l$) coming from the lattice vibrations called phonons.

$$k = k_e + k_l \tag{1.10}$$

Wiedemann-Franz law relates the electronic contribution to the electrical conductivity and the carrier concentration as:

$$k_e = L\sigma T = ne\mu LT \tag{1.11}$$

Where 'L' is the Lorentz factor, usually constant for metals and highly doped semiconductors, but reduces to as much as 20% when the carrier concentration is lowered. $k_l$ can be calculated once the $k_e$, σ and L are known. Since the improvement in ZT requires high electrical conduction but lower thermal conduction, eq. 1.7 indicates one of the inherent conflicts as $k_e$ and σ are directly proportional to each other.

Now we come to the lattice contribution to the thermal conductivity. Glasses have very low thermal conductivities, the heat transfer is conceived as a random walk of energy through the lattice instead of rapid transport by lattice vibrations. But the problem with the glasses is that they have very poor electrical conduction as well, because they lack the high mobility and low carrier scattering of the crystalline band structure. So we need such a crystalline semiconductor that can manage to sufficiently scatter phonons but provide high mobility to the charge carriers, i.e. a 'phonon-glass electron-crystal'.

The phonons transporting heat through a crystal span a wide spectrum of wavelengths, from less than 1nm to greater than 10µm. Many mechanisms have been suggested to introduce scattering in different regions of phonon spectrum (figure 1.3).

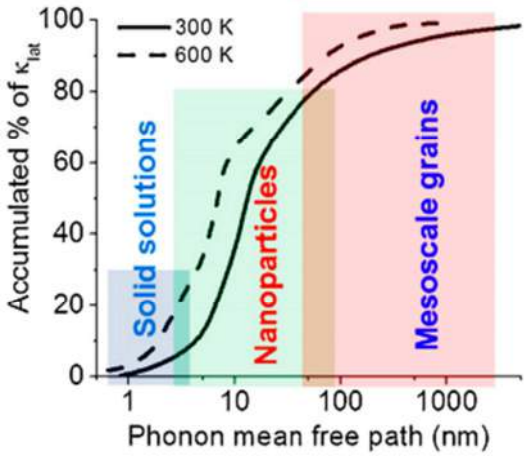


**Fig. 1.3.** Contributions of phonons with varied mean free paths to the accumulated $k_l$ value for PbTe at different temperatures. Phonons with short, medium and long mean free paths can be effectively scattered by atomic-scale point defects, nanoscale precipitates and mesoscale grain boundaries, respectively. Image adapted from Ref. [13].

### 1.2.3 Effective Mass

From eq. 1.8, it is obvious that the larger the effective mass, the higher the Seebeck coefficient. The effective mass given in eq. 1.8 is the density-of-states effective mass, which increases with flat, narrow bands with high density of states at the Fermi surface. However, since this effective mass is also related to the inertial one, the higher it is, the lower would be the velocity, and hence the mobility, of the charge carriers. But, these effective masses can be decoupled in anisotropic crystals [14].

The conflict between the high effective mass, required for high Seebeck coefficient values, and high electrical conductivity has to be managed. High effective masses are usually found in materials with narrow bands, such as ionic compounds. High carrier mobilities are typically observed in the materials made from elements with small electronegativity differences.

## 1.3 Recent Developments

Recently dramatic achievements have been made by introducing different mechanisms to scatter phonons at different length scales or by modifying the electronic band structure. In modern thermoelectric materials, there are two main points of focus: introducing complexity at multiple length scales to improve the scattering of the phonons while preserving the carrier transport, or, using complex crystal structures such that the electron-crystal can be separated from the phonon-glass. Since the thermoelectric technology can be expected to contribute to solving the world energy problems only if it can convert considerable amount of heat waste to electrical energy, therefore we focus on the developments in bulk systems. To achieve these goals, following mechanisms have been adopted so far:-

## 1.3.1 Introducing Defects

Typical defects in crystalline bulk materials are: (i) point defects in the structure arising from missing atoms (vacancies), atoms at the wrong sites or unintended impurities, etc. (ii) planar dislocations caused by some stress (iii) nano-sized grains, twin Boundary defects or disordered solids such as amorphous or polycrystalline materials.

At thermal equilibrium, a certain number of defects is always present in a crystal because they increase the entropy and minimize the free energy, F = U - TS. The probability that a particular lattice site is vacant is proportional to the Boltzmann factor for thermal equilibrium: $P = e^{(-E_V/K_B T)}$, where '$E_V$' is the energy required to create a vacancy by moving an atom from the lattice site to the surface. The equilibrium concentration of the vacancies increases as the temperature increases. The real concentration of the vacancies can be higher than the ideal value if the crystal is grown at elevated temperatures and then suddenly cooled down, freezing the vacancies of the high temperature equilibrium state [15].

Point defects can be of three types: chemical impurities (i.e. substitutions), vacancies (i.e. schottky defects) or extra atoms not in regular lattice positions (e.g. Frenkel defects or the rattling atoms). In a Frenkel defect, an atom is transferred from a lattice site to an interstitial site where there is no lattice point. Demands of charge neutrality may also result in vacancies when an ion is replaced by the one of higher valence. Adding chemical impurities in the semiconductors has been quite common. In doped semiconductors, most of the electrical conduction is attributed to the impurities. Figure 1.4 illustrates some of the point defects.

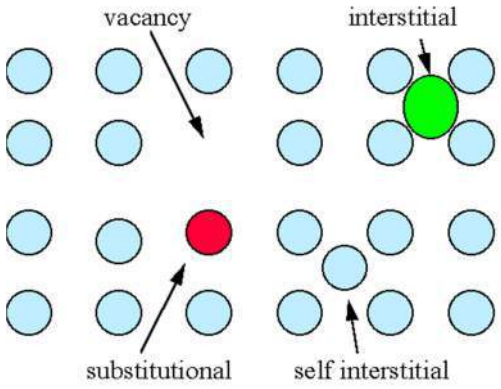


**Fig.1.4.** Point defects. Image adapted from Ref. [16].

Now we come to the thermoelectric consequences of these defects. The vacancies, interstitial substitutions or chemical impurities can act as scattering centers for short wavelength phonons while preserving the electrical conductivity. Alloying the binary tellurides has been an active area of research. Many of recent high ZT materials (e.g. TAGS [17]) have been prepared by alloying to exploit these distortions of the lattice/unit cell. Filling the vacant sites with rare-earth or other heavy atoms can also be a very efficient tool

to reduce the thermal conductivity. A clear correlation between the reduction of thermal conductivity and the size and vibrational motion of the atoms filling the vacancies has been found [18]. Replacing ions with the ones of different valance has also been a successful tool to increase the number of scattering centers for the lattice vibrations.

## 1.3.2 Nanostructuring

As mentioned earlier, the research in thermoelectric materials has undergone a renaissance after theoretical predictions of improvement in the thermoelectric performance because of nanostructuring [11]. The decrease in thermal conductivity was observed in thin-film superlattices in 1980's [19]. Recently, it has been shown that the phonon scattering in thin-films [20] and nanowires [21,22] can make the thermal conductivity approach the $k_{min}$ limit (0.2-0.5 $Wm^{-1}K^{-1}$) [23]. The energy barriers associated with these nano structures can also behave as a kind of energy filter which can scatter low energy charge carriers, hence increasing the Seebeck coefficient. The Seebeck effect requires that the high energy carriers diffuse from the hotter end to the colder end of the material and produce an electric field which stops this diffusion. Low energy carriers diffuse from the colder end to the hotter end and the Seebeck voltage depends on the difference between the chemical potentials of the carriers at the two ends. It is favorable if the carriers with higher energies are scattered less than the ones with lower energies, resulting in a smaller cancellation of the two competing diffusions, thereby increasing the chemical potential gradient.

The three types of quantum confined structures are:

1) Quantum wells (2-D structure) made by techniques of advanced epitaxial crystal growth.

2) Quantum wires (1-D structure) made by lithographic patterning of quantum wells or by epitaxial growth on patterned substrates.

3) Quantum dots (0-D structure) made by lithographic patterning or by spontaneous growth techniques.

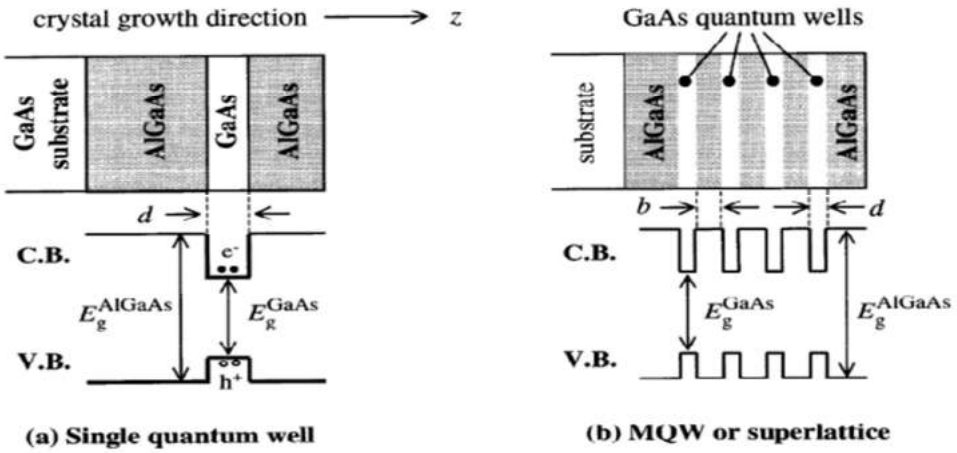


**Fig. 1.5.** (a) Schematic diagram of a single GaAs/AlGaAs 2D quantum well. The quantum well is formed in the thin GaAs layer sandwiched between AlGaAs layers which have a larger band gap. (b) Schematic representation of a GaAs/AlGaAs multiple quantum well (if b is large so that the individual quantum wells are isolated from each other) or superlattice structure (if b is small enough that carriers can tunnel through, forming new extended states in the z-direction). Image adapted from Ref. [24].

Reduction of dimensionality provides a highly structured density of states, as illustrated in figure 1.6. This may lead to abrupt changes in the number of available states at the Fermi energy. The Seebeck coefficient and the electrical conductivity are directly related to the elaborate electronic structure near the Fermi level.

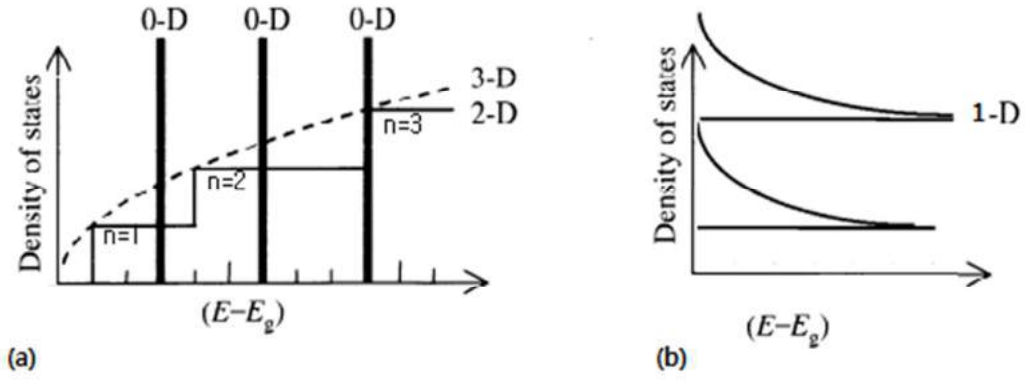


**Fig. 1.6.** (a) Variation of the electron density of states with dimensionality. The dashed line is for a bulk semiconductor with a band gap of 'Eg'. The thin solid line is for a quantum well with infinite barriers. The thick solid lines are for a cubic quantum dot with infinite barriers. (b) Variation of electron density of states for a 1-D quantum wire. Image adapted from Ref. [24, 25].

The scattering of phonons by interfaces in a nanostructured system can reduce the lattice contribution to the thermal conductivity substantially. In undoped Si, about 80% of heat is transported by phonons whose mean free path is less than 10µm and about 40% by the ones with mean free path below 100nm [26]. Phonons will be scattered if spacing between the interfaces is of the order of their mean free paths. In contrast to the case of point defects

which scatter the short wavelength phonons, nanostructured materials can scatter mid to long wavelength phonons.

For large scale commercial applications, we need cost effective macroscopic devices. Kanatzidis et al. discovered the formation of nanoscale precipitates (nano dots) in LAST-m system ($Pb_mAgSbTe_{2+m}$) as an inherent property of this system [27]. For m ≤ 8, phase segregation occurs, while at higher lead contents, powder XRD data shows single rocksalt phase. Figure 1.7 shows that quenching these samples from the melt results in single-phase materials when studied by powder XRD, but when these are annealed at about 400 $^{o}$C, phase segregation occurs.

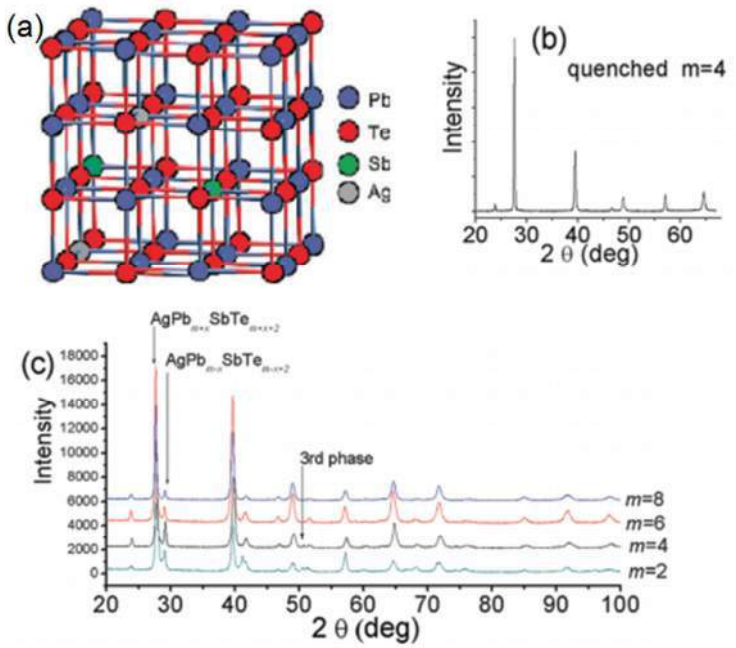


**Fig. 1.7.** (a) Schematic of the rocksalt structure of the LAST-m system. (b) X-ray diffraction pattern of a quenched LAST-m sample consistent with single phase. (c) X-ray diffraction pattern of a slow cooled (or annealed) LAST-m sample showing microscopic phase segregation. The so-called "3$^{rd}$ phase" indicated in (c) is a minor impurity phase. Image adapted from Ref. [27].

For 2 ≤ m ≤ 8, the sample definitely has a biphasic composition since the phase separation gives clear peaks in the XRD pattern. These peaks indicate that the system has large micrometer sized regions belonging to the phases other than the matrix itself. These regions do not contribute to the reduction of the thermal conductivity as their size is many orders of magnitude bigger than the typical wavelength of a phonon.

For m ≥ 10, the powder XRD data indicates again a single phase material, however, a more precise look using TEM reveals the formation of silver and antimony rich nano inclusions within the PbTe matrix. Nano scale regions of chemical composition other than the matrix are formed due to nucleation during cooling and they orient along the {001} planes with a high lattice strain at the interface.

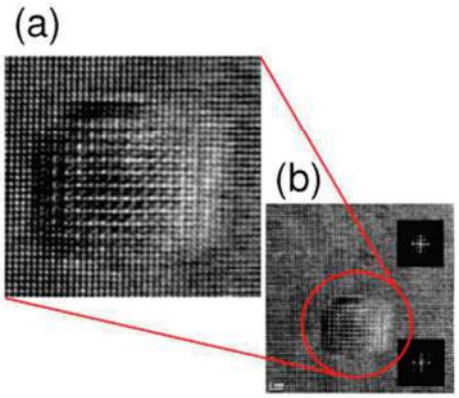


**Fig. 1.8.** (a) High resolution image of an inclusion in $Ag_{0.53}Pb_{18}Sb_{1.2}Te_{20}$ along the [001] zone axis. (b) TEM micrograph of nano scale inclusion in $Ag_{0.53}Pb_{18}Sb_{1.2}Te_{20}$. Image adapted from Ref. [27].

Nano inclusions are also found in systems like LASTT ($Pb_mAgSbSn_nTe_{2+m+n}$), SALT-m ($NaSbPb_mTe_{2+m}$), PLAT-m ($KPb_mSbTe_{2+m}$), PbTe-PbS.

Liquid encapsulation can be a very useful technique to produce bulk crystals with nanostructures embedded in them. To achieve this, the minority phase should be chosen such that it has very low or no solubility in majority phase in the solid state, but it is completely soluble in the liquid state. Moreover, the majority phase should have an equal or higher melting point than the minority phase (which is supposed to form nano precipitates) so that the nucleation of the nano dots starts well before the solidification of the matrix. Mass contrast between the majority phase and the nano inclusions is also important for efficient scattering of the lattice vibrations.

Sootsman et al. reported [28] the intentional preparation of nanometer sized inclusions of Sb, Bi, and InSb in bulk PbTe using liquid encapsulation technique. They observed that the InSb-containing samples, which have the largest atomic mass difference with the PbTe matrix, exhibit the lowest lattice thermal conductivity, ≈45% lower than pristine PbTe at room temperature. The samples with Bi nano inclusions had a thermal conductivity very close to that of PbTe. This is because the Bi nanophase and the PbTe matrix have very little mass contrast since Bi and Pb have nearly the same mass number. The study of samples with Sb nano inclusions showed that the ones with lowest concentration of nano inclusions, i.e. 2%, showed lowest thermal conductivity. This sample had the lowest average nano particle size and no micro meter sized Sb grains. This study reveals that an optimum, not maximum, concentration of the nano inclusions would cause the maximum effect. This can be attributed to the overall high interface area between the Sb nano inclusions and the PbTe host.

Besides liquid encapsulation, there are other approaches to achieve nanostructuring, namely the formation of nano sized polycrystalline samples formed by hot pressing or spark plasma sintering of fine powders. Ball-milled n-type silicon with crystallite sizes ranging from 5nm to

20nm was reported [29] to have dramatic decrease in thermal conductivity as compared with the normal bulk material.

## 1.3.3 Complex Unit Cells

Using materials with complex crystal structure is another realm of advanced thermoelectric material research. Complexity in the unit cell has been reported to be a source of reduction of thermal conductivity and improvement of the Seebeck coefficient. Extremely low thermal conductivities, comparable to most of the state-of-the art thermoelectric materials like PbTe, TAGS, $Bi_2Te_3$, etc, have been observed in complex material systems like $Yb_{14}MnSb_{11}$ [30], $CeFe_3CoSb_{12}$ [31], $Ba_8Ga_{16}Ge_{30}$ [32], $Ag_9TlTe_5$ [33], etc.

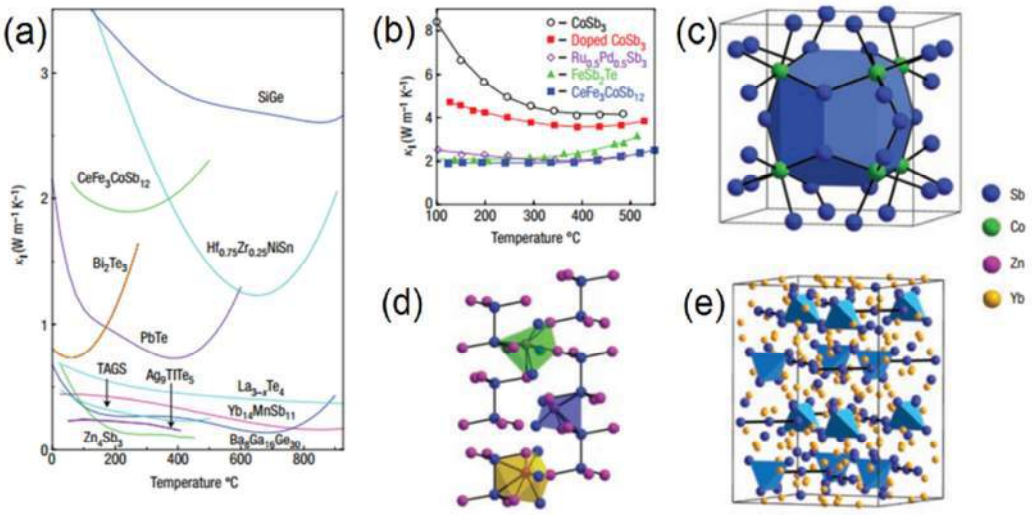


**Fig. 1.9.** (a) Thermal conductivities of complex structure systems compared with most state-of-the art thermoelectric materials. (b) The thermal conductivity of doped $CoSb_3$ and $CeFe_3CoSb_{12}$ is quite less than that of the pure $CoSb_3$. (c) The skutterudite structure is composed of tilted octahedral of $CoSb_3$ with large void space shown in blue. This large void can accommodate relatively large atoms. (d) The room temperature structure of $Zn_4Sb_3$ has a crystalline Sb sublattice (blue) and highly disordered Zn sublattice containing a variety of interstitial sites (in polyhedral) along with the primary sites (purple). (e) The complexity of the $Yb_{14}MnSb_{11}$ unit cell is illustrated, with $[Sb_3]^{7-}$ tri-mers, $[MnSb_4]^{9-}$ tetrahedral, and isolated Sb anions. The Zintl formalism describes these units as covalently bound with electrons donated from the ionic $Yb^{2+}$ sublattice (yellow). Image adapted from Ref. [6].

A good example is $CsBi_4Te_6$, the complex variant of $Bi_2Te_3$ which is reported to have lower thermal conductivity [34]. It has a lamellar structure with slabs of $(Bi_4Te_6)^{1-}$ alternating with layers of $Cs^{1+}$ ions. The layering in the structure makes the effective mass of the carriers anisotropic hence improving the Seebeck coefficient. This material also has additional Bi-Bi bonds which decrease the band gap to nearly half of $Bi_2Te_3$. Appropriately doped $CsBi_4Te_6$ gives rise to a maximum in ZT of 0.8 at 225K, which is among the highest ever ZT values reported below the room temperature. The maxima can be shifted to even lower

temperatures (≈180K) with appropriate choice of dopants [35]. The achievement of ZT maxima at low temperatures is attributed to the narrow band gap in the $CsBi_4Te_6$.

Complex Zintl compounds have combinations of ionic and covalent bonds which lead to complex unit cell structures. One example is $Yb_{14}MnSb_{11}$ which contains $[MnSb_4]^{9-}$ tetrahedral, polyatomic $[Sb_3]^{7-}$, isolated $Sb^{3-}$ anions along with $Yb^{2+}$ cations. In this material, extremely low thermal conductivity has been observed [30].

## 1.3.4 Substructuring

The thermoelectric efficiency can be improved by making a material with different regions of charge and heat transport, this way we can separate the electron-crystal from the phonon glass, much like the charge reservoir region in high-$T_C$ superconductors. In the phonon-glass region, we can introduce all the structural complexities to minimize the thermal conductivity without affecting the charge transport in the electron-crystal zone. The electron-crystal region would be thin, like quantum wells with nano meter thickness. Such thin regions of charge transport may also enhance the Seebeck coefficient because of quantum confinement and electron filtering effects.

A good example is the enhanced thermoelectric power in the $Na_xCoO_2$ material [36]. The Co-O layers form the metallic electron-crystal region. Oxides are usually a bad choice for thermoelectric applications due to their low electrical conductivity and high thermal conductivity, but the high thermopower of this material may well be because of substructuring.

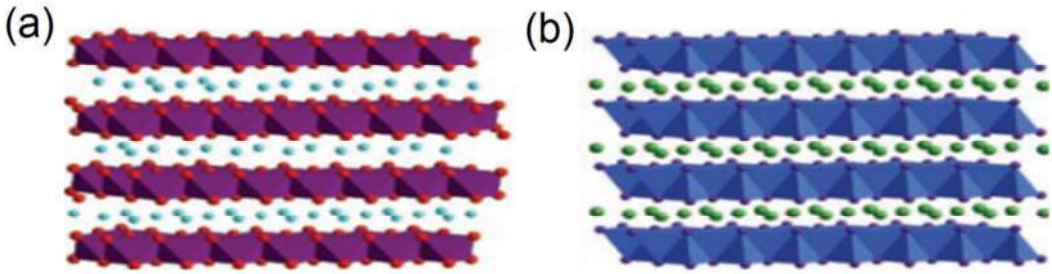


**Fig. 1.10.** Ordered layers (polyhedral) separated by disordered cation monolayers in (a) $Na_xCoO_2$ and (b) $Ca_xYb_{1-x}Zn_2Sb_2$, separating phonon-glass from electron-crystal. Image adapted from Ref. [6].

This separation-of-regions effect can be clearly observed in $Ca_xYb_{1-x}Zn_2Sb_2$ which has sheets of disordered cations between the layers of covalently bonded Zn-Sb [37]. Since Yb is slightly less electropositive than Ca, the carrier concentration can be varied by slightly varying the Yb:Ca ratio. The disorder in the cation layer lowers the thermal conductivity while the electrical conductivity is not affected much since the ordered anion substructure preserves the band gap. Combining this approach with nanostructuring can open new avenues of research.

## 1.3.5 Distortion of the Electronic Density of States

Most of the research in the last decade has been focused on improving the (σ/k) ratio but there is a limit [38] to this route. Band structure engineering can help improve the Seebeck coefficient of materials by distorting the density of states near the Fermi level, hence increasing the ZT by improving the thermoelectric power factor $P = S^2\sigma$. The product $S^2\sigma$ is purely electronic property. Such band structural engineering was reported [39] to increase the ZT in p-type PbTe to above 1.5 at 773K.

The close relationship between the Seebeck coefficient and the distortions in the density of states near the Fermi level is evident from the Mott relation:

$$S = \frac{\pi^2}{3}\frac{k_B}{q}k_B T\left\{\frac{d[\ln(\sigma(E))]}{dE}\right\}\Big|_{E=E_F}$$

$$= \frac{\pi^2}{3}\frac{k_B}{q}k_B T\left\{\frac{1}{n}\frac{dn(E)}{dE} + \frac{1}{\mu}\frac{d\mu(E)}{dE}\right\}\Big|_{E=E_F} \qquad (1.12)$$

Here σ(E) is the electrical conductivity, μ(E) is the electrical mobility, q is the carrier charge, n(E) = g(E)f(E) is the carrier density and S depends upon the energy derivatives of μ(E) and n(E) evaluated at the Fermi energy.

The density of states, g(E), is a measure of the number of available electronic energy states in a unit volume within the interval E to E+dE, expressed in the units of number of states per eV per $cm^3$. Mahan and Sofo derived [40] the ideal mathematical function for the transport distribution that would give the maximum figure of merit, ZT. They found that the conditions for the largest figure of merit were:

1) the transport distribution function, which further depends on the density of states, is a Dirac delta function,

2) the peak of the transport distribution function is within $2.4k_BT$ above or below the Fermi level.

An ideal delta function is not possible to realize in lab. However, the f-orbitals are tightly bound in atoms and bind less to the extended energy levels in solids. The density of states function corresponding to f-orbitals is a lorentzian with a very narrow width. Mahan and Sofo made an estimate of maximum ZT achievable by introducing ideal dopant levels with Dirac delta shaped density of states near the Fermi energy, and they found it to be 14, about 10 times higher than the ZT values of the best known thermoelectric materials to date. Mahan and Sofo found that the presence of electronic density of states other than the Dirac delta shaped function near the Fermi level, which they called the “background”, decreases the figure of merit substantially. They concluded that a background of more than 1% of the integrated contribution of the peak would not be desirable.

One of the ways to achieve this is to add resonant impurity levels to the electronic band structure. Resonant levels involve a coupling between the charge carriers of a dilute impurity and those in the conduction or the valence band of the host material. Resonant impurities increase the effective mass of the carriers and hence increase both the Seebeck coefficient and the electrical resistivity, but the enhancement of Seebeck coefficient dominates in the power factor, $S^2/\rho$. People have successfully improved the thermopower of PbTe [39] by introducing resonant levels in the valence band coming from Thalium doping and of $Bi_2Te_3$ [41] by adding tin.

The resonant levels are different from the states created by the donor or acceptor impurities. A donor impurity would introduce an extra electron in a qusai-local bound state with an energy $E_D$ (a few meV) below the conduction band edge and in the band gap of the semiconductor. This case can be considered as a hydrogen atom with $E_D$ as an effective Rydberg $R^*$. In contrast, a resonant donor level would fall above the conduction band edge. For a p-type material, a resonant accepter level would fall below the valance band edge.

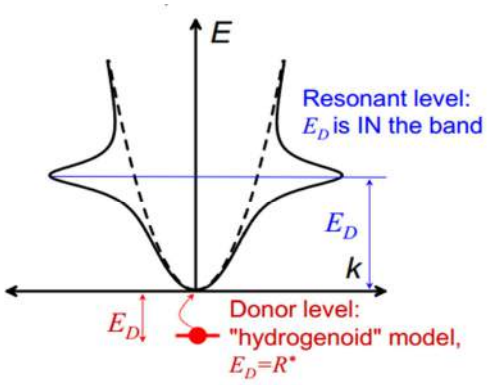


**Fig. 1.11.** Schematic diagram of the conduction band of an n-type semiconductor with a resonant donor level and a trivial donor impurity state. The increase in density of states in the vicinity of the resonant level is evident. Image adapted from Ref. [42].

The resonant impurity state resonates with the extended states of the host solid and develops a certain width 'Γ'. The energy of this state with reference to the band edge, $E_D$, and the width 'Γ' are important parameters in determining ZT.

The electronic band structure is the result of the periodic potential of the host lattice. The resonant impurity atom can be thought of as a local perturbation to this lattice potential. When the charge carriers enter a resonant level, they feel slightly bound there and stay there for a while ($\Delta t \approx \hbar/E_D$) before jumping back to the band with a different momentum. If the broadening of the resonant level, Γ, is not too large, the carriers with energies close to the level will be considerably scattered. Mahan and Sofo calculated [40] that the narrower the Γ, the higher the ZT. Usually the conduction band edge has an s-character and the width, Γ, is small when the angular momentum part of the impurity state has small overlap with those of the extended states, i.e. when the resonant level has a d- or f- character. But for some semiconductors, where the number of carriers up to the Fermi level is too small, of the

order of $10^{-2}$ to $10^{-4}$ electrons per atom, the choice of d- or f-orbitals as resonant levels would result in impractically narrow Γ-values, so one can think of having p-orbitals as resonant levels in these materials, instead of the d- or f- orbitals.

L. A. Fal'kovskii [43] calculated that the narrow band gap semiconductors are more likely to have resonant levels. This is because in the narrow band gap semiconductors or semi-metals, the carriers usually have small effective masses, hence longer de-Broglie wavelengths which make it more likely for their wave functions to overlap with the impurity states.

In 1982, V. I. Kaidanov, et al. reported [44] the existence of quasi-local resonant levels in Tl-doped PbTe. In 2008, J. P. Heremans et al. reported [39] a doubling of ZT in dilute alloys of p-type PbTe with 2% Thallium (Tl-PbTe). Optical measurements indicated that there were several distinct levels associated with Thallium in PbTe, one of which was at ≈0.06eV below the valence band edge. Measurements of electronic specific heat showed an increase in the density of states in the valence band as a function of Tl concentration. The value of ZT was 1.5 at 773K which was double the maximum value for the best conventional PbTe alloy [45] ($ZT_{max.}$ = 0.71 for $Na_{0.01}Pb_{0.99}Te$). Note that the ZT value for the Tl doped sample has not saturated at 773 K and is still increasing.

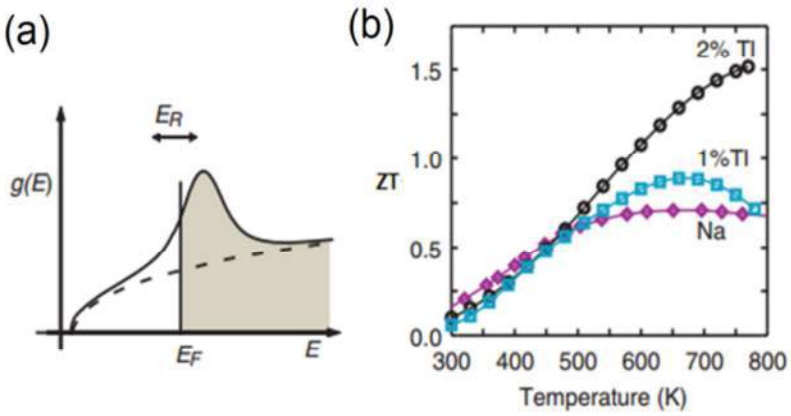


**Fig. 1.12.** (a) Schematic representation of density of states of valence band of Tl-doped PbTe (solid line) compared with that of pure PbTe (dashed line). (b) The ZT values for $Tl_{0.02}Pb_{0.98}Te$ (black squares) and $Tl_{0.01}Pb_{0.99}Te$ (blue circles) compared to that of a reference sample of Na-PbTe (purple diamonds). Image adapted from Ref. [39].

In 2006, S. Ahmed et al. had reported ab initio calculations of the electronic structure of defects in PbTe using density functional theory [46]. In PbTe, the 6s and 5s states are quite deep and the valence and conduction bands are formed primarily out of 6p states of Pb and 5p states of Te. Tl is a trivalent impurity with valence configuration of $6s^2$ $6p^1$ belonging to group III. It showed a strongly bound state below the bottom of the valence band (hyper-deep state) and a state near the band gap region (deep defect state). The deep defect state was seen to increase the density of states near the Fermi level. This meant that it is a

resonant level. This resonant state was created by a hybridization of the s-state of the Tl atom with the p-state of Te atom.

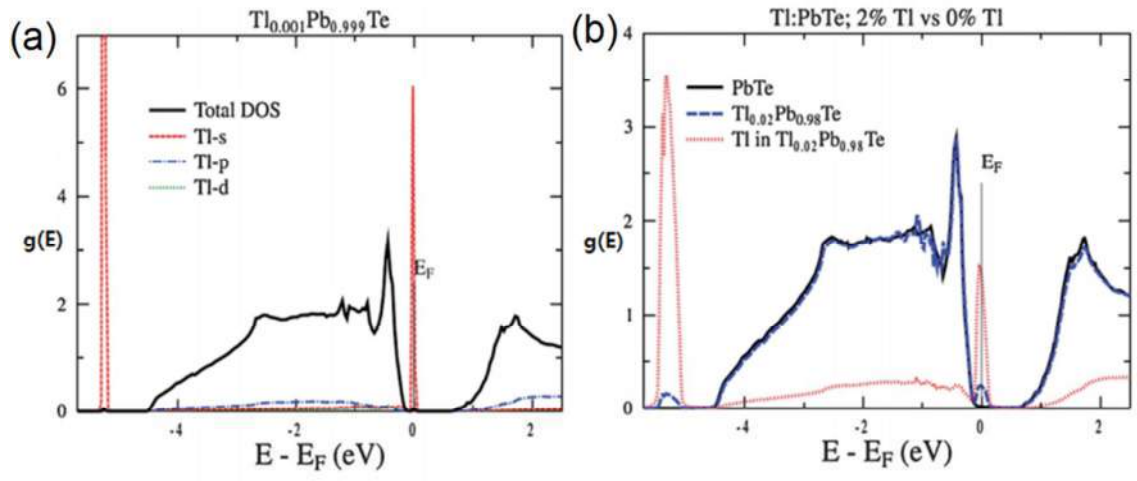


**Fig. 1.13.** Calculated density of states for PbTe with Tl impurity, assuming substitution of Tl atom on Pb site with 0.1% concentration (a) and 2% (b). States located in lower energy range are not shown (6s of Pb and 5s of Te).
(a) Black line is a total density of states per formula unit. Partial Tl densities of states (per Tl atom, not multiplied by concentration) are plotted in red (s), blue (p) and green (d). The most striking feature of the electronic structure is the presence of sharp, semi-core-like DOS peaks from 6s states (the hyper deep and the deep defect states) of Tl in the valence band region. The Tl 6p states are fully integrated into the valence band, crucial for bonding.
(b) For 2% Tl concentration, Tl peak is broadened and hybridization with p orbitals of Te and Pb occurs. This leads to the formation of a DOS 'hump'. Most of the contribution to this hybridized s+p band comes from Te(50%) and Pb (15%) atoms and Tl contributes only 12% to this hump at the Fermi level. Image adapted from Ref. [42].

Another mechanism for meeting the conditions of Mahan and Sofo [40] is to induce the Kondo Effect by adding dilute magnetic impurities. Here again the resonant levels are involved but now with a magnetic moment. Consider a resonant level below the Fermi level, with an energy $E_d$, occupied with a spin-up electron. To put a spin-down electron at the same level would cost Coulomb repulsion energy, U. One may say that the second electron will occupy this level but with energy $E_d$+U. For large enough U, this electron will have to lie above the Fermi level. Consequently, for large U values, the state will not contain two electrons and would have an unpaired electron.

In dilute alloys of magnetic ions in a non-magnetic host, we can ignore the RKKY interaction between the magnetic impurities. At high temperatures, these magnetic moments would behave as free, paramagnetic moments. This situation is theoretically described in the Anderson model for magnetic impurities in metals. Kondo considered higher order terms in the perturbation theory, especially the interaction of the spin at the resonant level and that of the conduction electrons. Below a characteristic temperature, known as the Kondo temperature, $T_K$, the spins of the conduction electrons in the vicinity of the magnetic

impurities interact with the the spin in the resonant level in such a way that they shield its magnetic moment and effectively make it non-magnetic.

To see how it works, let us consider a simple example of a quantum dot embedded in a metal with odd number of electrons, as shown in figure 1.14. The highest state for the electron is doubly degenerate, i.e. it can either have a spin up or down. The addition of a second electron is allowed by the Pauli exclusion principle but is not energetically favorable due to the coulomb repulsion between the carriers. Therefore, the dot has a magnetic moment with S = ½ with double degeneracy. If we consider the coupling of this electron to the ones in the conduction band of the host, the degeneracy would be removed at small temperatures and the ground state would be a linear superposition of the two spin configurations with transition between them possible by a virtual intermediate state involving an exchange of electrons with the conduction band. The local moment now pairs with the electrons in the conduction band of the host metal to create a spin singlet (S = 0).

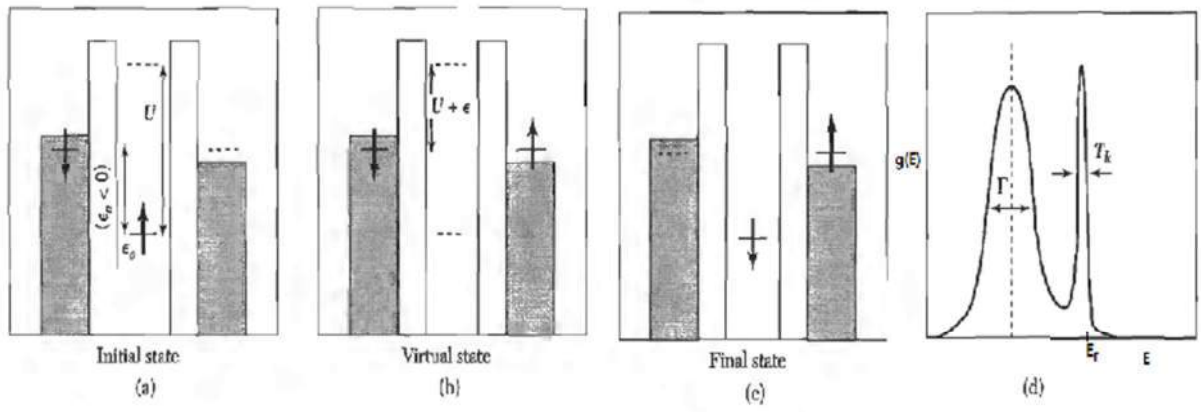


**Fig. 1.14.** For an unpaired spin on the quantum dot, a virtual process (b) can occur to convert the spin up (a) to spin down (c) transferring an electron from one side of the dot to the other. The ground state of the system is a linear superposition of the initial (a) and final (c) states. This is called the Kondo effect, producing a narrow peak of width $k_BT_k$ in the density of states (d) at $E_F$ in addition to the original broadened level. The broadening 'Γ' of the original state comes from the uncertainty principle due to the finite life time of the state. Image adapted from Ref. [15].

Kondo showed that the scattering amplitude for a conduction electron being scattered from a magnetic impurity through the coupling of impurity spin with the spin of conduction electrons diverges logarithmically. He showed that for an antiferromagnetic exchange (J<0), there is a contribution to the resistivity that increases logarithmically with decreasing temperature, given as:

$$\Delta\rho = c\rho_m\left[1 + JN(0)\ln\left(\frac{2k_BT}{D}\right) + \cdots\right] \qquad (1.13)$$

Where 'c' is the impurity concentration, '$\rho_m$' is the resistivity coming from the first order scattering terms due to defects and impurities, 'N(0)' is the density of states in a flat band of

width 'D' and 'J' is the antiferromagnetic exchange integral. Adding to this the phonon contribution (≈ $T^5$), one obtains a resistivity minimum as a function of temperature. The onset of this effect occurs below the Kondo temperature, $T_K$, defined as:-

$$k_B T_K = D \exp[-N/|J|N(0)] \quad (1.14)$$

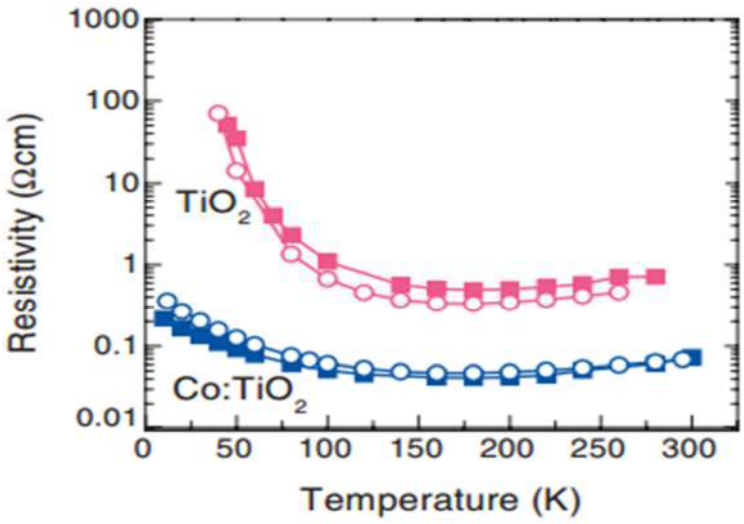


**Fig. 1.15.** Electrical resistivities of two undoped $TiO_2$ thin films (pink) and two Co:$TiO_2$ thin films (blue) grown under same deposition conditions. Kondo effect is evident below $T_K$ = 120K. Image adapted from Ref. [47].

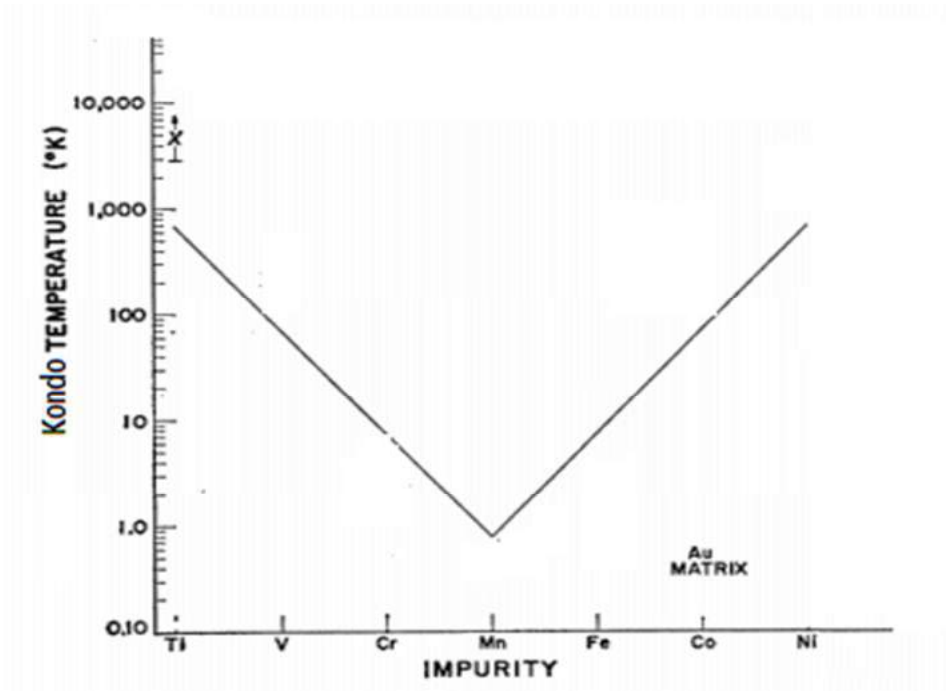


**Fig. 1.16.** Kondo temperatures for first-row transition elements in gold. Values are obtained from data in sufficiently dilute alloys such that impurity-impurity interactions are not important, and therefore are properties of the impurity-matrix interaction itself. Image adapted from Ref. [48].

Kondo effect has two major experimental consequences. First, the magnetization becomes lower than its free-moment value and hence the susceptibility falls below the value given by the Curie's law. Second, the resistivity minimum, as shown in figure 1.15 for $TiO_2$ and Co:$TiO_2$ thin films. The resistivity of metals decreases by decreasing the temperature, because the number of phonons falls but the onset of the Kondo effect below $T_K$ makes the resistivity increase because now the scattering cross section of the moment is strongly enhanced. A peak in the density of states of width $k_BT_K$ occurs at the Fermi energy because of enhanced scattering. The Kondo temperature can be as high as 1000K [48] (See figure 1.16) but the effect of small and positive increase of the Seebeck coefficient of the host is unimportant and has been ignored [49] (See figure 1.17).

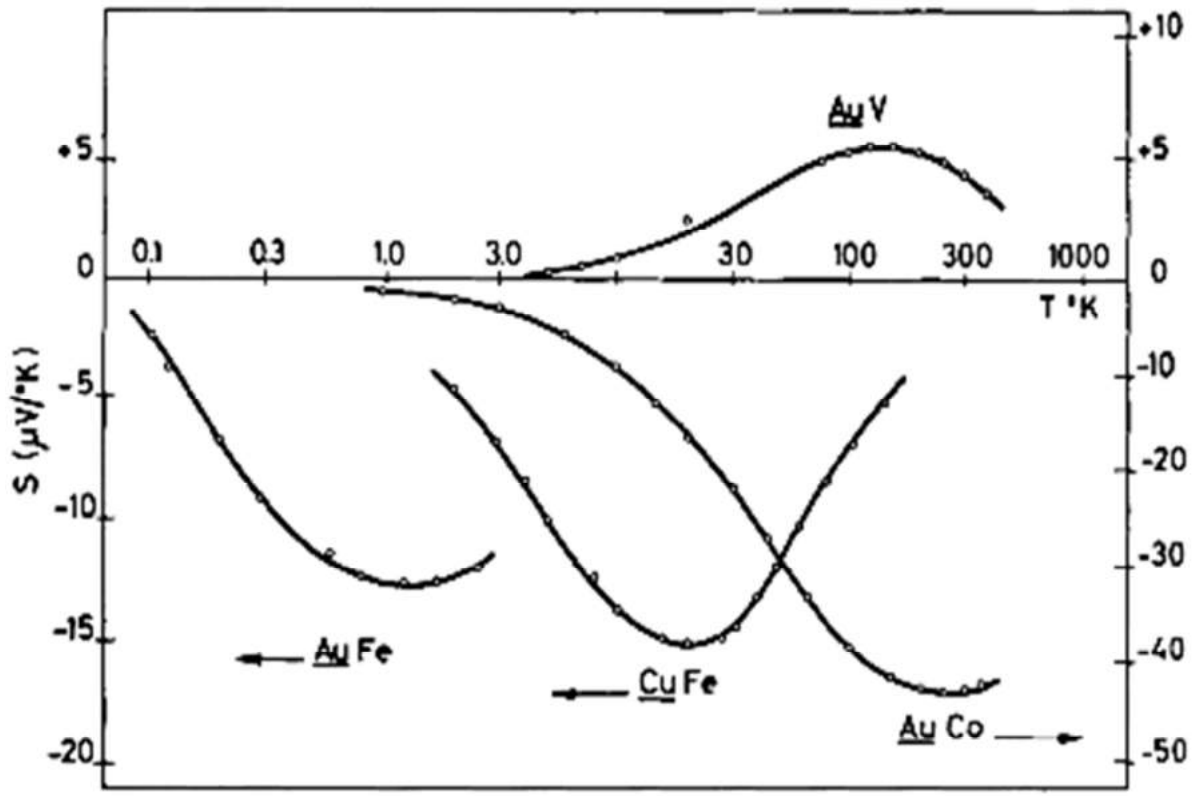


**Fig. 1.17.** Temperature dependence of the Seebeck coefficient of gold and copper containing magnetic impurities from the first row of the d-block elements. The peak occurs near the Kondo temperature. Image adapted from Ref. [49].

Chapter-2

# TAGS-85: A Literature Review

Germanium Telluride (GeTe) based semiconducting alloys have been used for thermoelectric applications since the 1960's. $(AgSbTe_2)_{15}(GeTe)_{85}$ or TAGS-85 is a p-type small band gap semiconductor with ZT values of 1.4 to 1.7 at elevated temperatures. Skrabek et al. say [17] that this material is normally synthesized by solid state reaction method by mixing the pure powders of the constituents and heating up to 800$^{o}$C for one hour, then slowly cooling down to 525$^{o}$C and annealing for 16 hours before quenching to the room temperature. Minor phases consisting of silver and antimony tellurides and also of pure antimony and germanium with varying content have been reported [50] some of which reduce size upon annealing. It is also reported that, upon heating, sublimation (thermal etching) starts to occur just above 516$^{o}$C. Therefore, this material is best for applications below 510$^{o}$C temperature. Common materials used for making contacts, like Cu, Fe, Ni, etc., react with TAGS around 500$^{o}$C, therefore, for high temperature measurements, it is recommended that a layer of some semiconducting material be inserted between the TAGS leg and the metallic strap [17].

## 2.1 Microstructure study of TAGS-85

Snykers et al. [51] performed detailed microstructural studies on GeTe and concluded that the material undergoes a transition from a rhombohedral to cubic structure when heated. At high temperatures, Te atoms occupy the (0, 0, 0) positions while Ge atoms go to the (1/2, 1/2, 1/2) positions. In the TAGS composition, the Sb and Ag atoms go to the Ge sites. Upon cooling through the transition temperature, the lattice deforms into a rhombohedral one due to thermal strain in the cubic lattice which shifts the Te and Ge atoms a little bit within the (220) planes. This deformation is manifested in an elongation along the [111] direction, i.e. the body diagonal of the unit cell. Since there are four [111] directions, this transition causes the twinning, an important phonon scattering mechanism. As a consequence of this structural transformation from cubic to rhombohedral, the (220) Bragg peak splits into a doublet. The transition temperature depends primarily on the ratio of GeTe to $AgSbTe_2$. Abrikosov et al. [52] did a detailed study of the TAGS-m systems and concluded that the structural transition occurs in the temperature range of 177$^{o}$C to 302$^{o}$C (450 to 525K).

Cook et al. performed [53] transmission electron microscopy on TAGS-85 samples prepared by heating the mixture of the constituent elements up to 825$^{o}$C for one hour and then annealing for 48 hours at 500$^{o}$C. Figure 2.1 shows a TEM bright field micrograph of the as-

solidified microstructure of TAGS-85, which shows extensive twinning within the (220) planes.

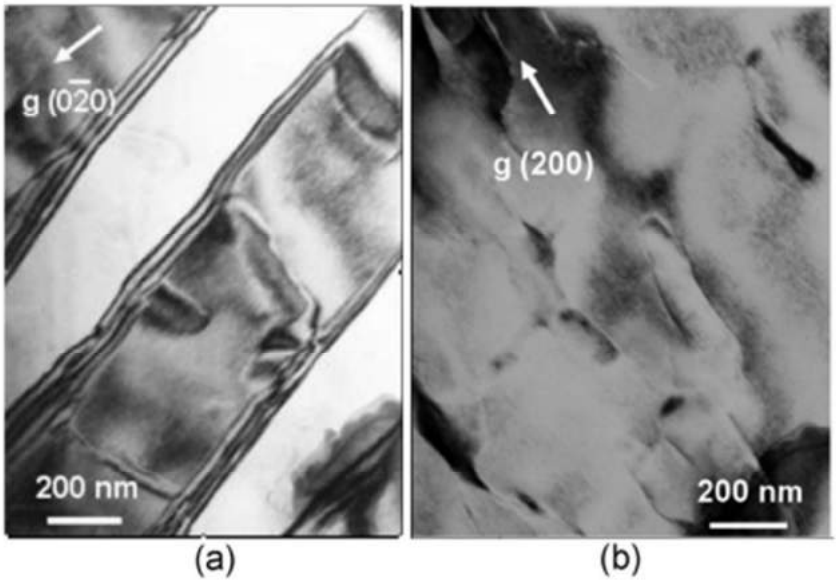


**Fig. 2.1.** TEM bright field image of twinning in (a) as-solidified TAGS-85, (b) antiphase domains are seen as continuous across twin boundaries by tilting the sample stage, which brings the twins out of contrast. Image adapted from Ref. [53].

The twins were reported to have a characteristic spacing ranging from 450 to 500 nm and spread throughout the material. These twin boundary defects can scatter mid-wavelength phonons. Numerous antiphase domains were also observed throughout the material. These antiphase domains were of 250 x 100 $nm^2$ dimensions with an average separation of ≈ 1 µm. The existence of these antiphase domains may also contribute to the low thermal conductivitiy of TAGS-85.

Cook et al. also studied the ice-bath quenching of the samples heat treated at temperatures ranging from 300$^{o}$C to 600$^{o}$C and the X-ray diffraction patterns they obtained for these samples looked pretty much the same as for the samples cooled slowly to the room temperature, i.e. they observed the (220) doublet corresponding to the room temperature rhombohedral phase (figure 2.2). They concluded that there may not exist a thermodynamic barrier to the rhombohedral to cubic transformation because of which the transformation is non-quenchable. They concluded that it was a second order phase transition.

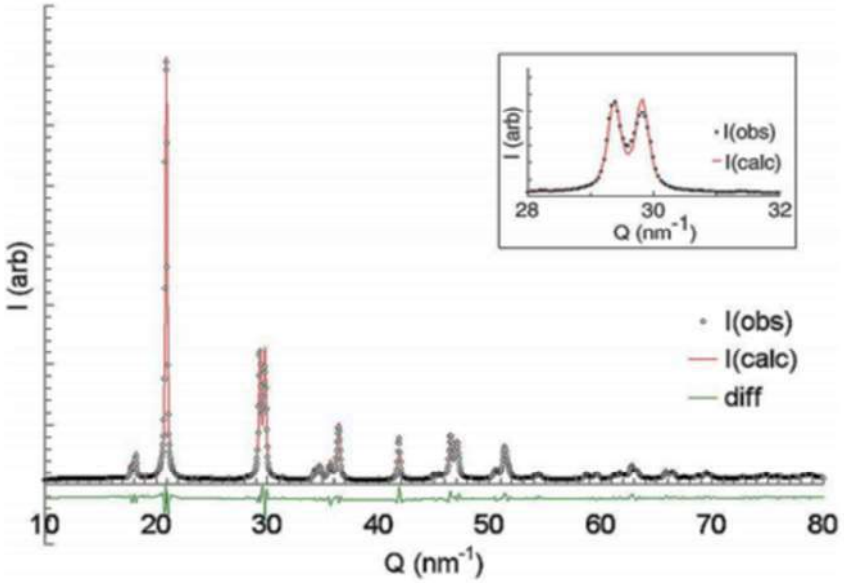


**Fig. 2.2.** X-ray diffraction pattern of as-solidified TAGS-85 at 300K. Note the (220) doublet shown in the inset at Q=29.5 nm$^{-1}$, characteristic of the $R_{3m}$ structure. Image adapted from Ref. [53].

They also did high-temperature X-ray diffraction studies of the as-solidified TAGS-85 powder. The result they obtained is shown in figure 2.3, whereby the (220) peak is studied over the temperature range of 300K to 600K (27$^{o}$C to 327$^{o}$C). The phase transition seems to have completed at 600K.

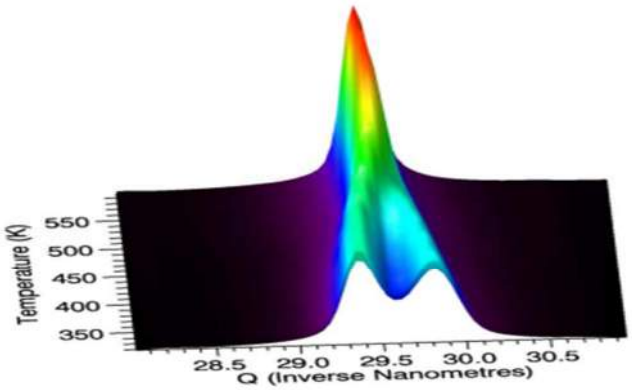


**Fig. 2.3.** The rhombohedral to cubic structural transformation seems to occur over a wide range of temperatures, starting from room temperature to about 510K. Image adapted from Ref. [53].

Yang, et al. performed [54] HRTEM and SAED on TAGS-80 and TAGS-90 materials. Their results clearly display the formation of nano domains of about 10 nm size in TAGS-80 with different atomic spacings and crystalline orientations. They report that such nano inclusions were largely absent in TAGS-90 which they were not sure if it was because of the lower lattice strain in this material?

## 2.2 Thermoelectric Properties of TAGS-85

Strabek et al. [17] studied TAGS-85 along with many other TAGS-m compositions. TAGS-85 was observed to have very low thermal conductivity, high power factor, as well as better mechanical strength and stability. The basic thermoelectric properties of TAGS-85 as reported by Skrabek et al. are given in figure 2.4.

Zhu, et al. recently reported [55] that the carrier mean free path of TAGS-85 materials is comparable to the lattice parameters indicating that the electrical mobility of this material system has almost reached the Ioffe-Regel limit for this material. This indicates that the grain size reduction will not affect the power factor, while it can reduce the thermal conductivity due to increased phonon scattering at grain boundaries. They prepared their samples by solid state reaction at 1000$^{o}$C and then air-cooled to room temperature. The samples were then separated in two parts. One part was directly crushed to make fine powder and then hot pressed in a graphite die at 500$^{o}$C under 70 MPa pressure for 30 min in vacuum. The other part was treated with melt-spinning followed by the same hot pressing process adopted for the first part. They reported to have enhanced the figure of merit up to 1.6 as a result of increased phonon scattering because of grain refinement. They also observed that the electrical mobility and mean free path of fine grained samples produced by melt spinning are comparable with those in coarse-grained samples prepared by slow cooling.

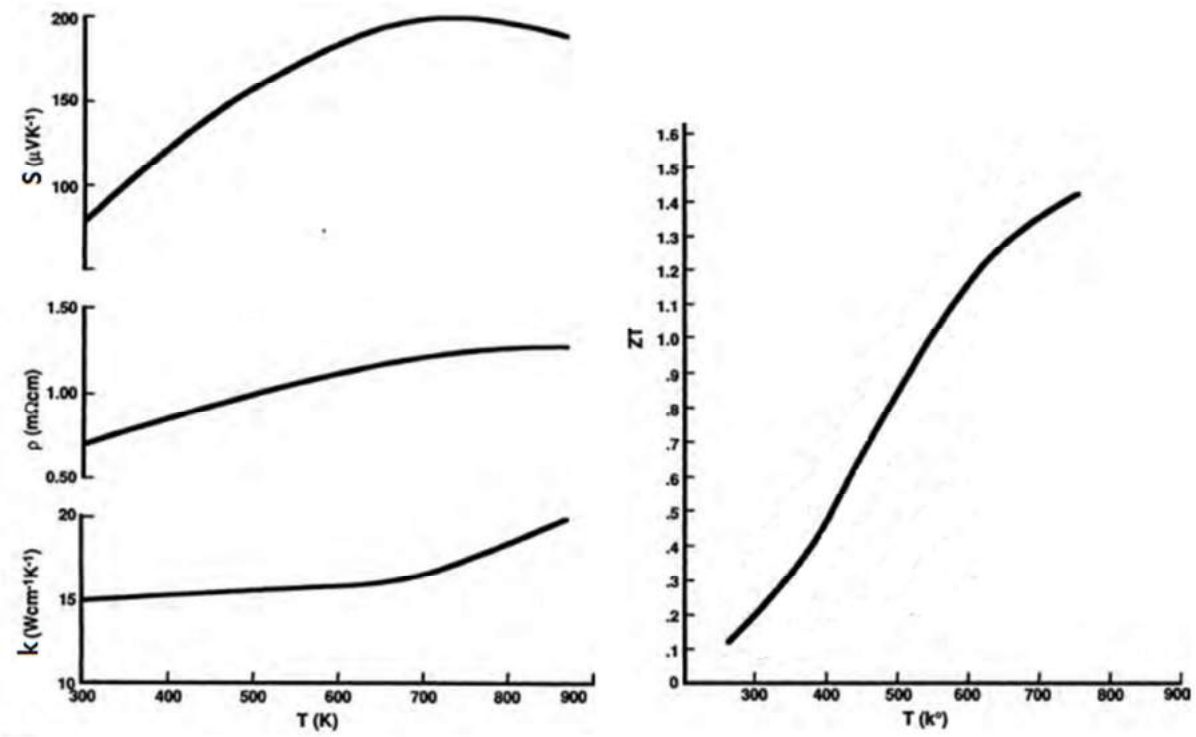


**Fig. 2.4.** Thermal conductivity, electrical resistivity, Seebeck coefficient and dimensionless figure of merit plotted against temperature for TAGS-85. Image adapted from Ref. [17].

# 2.3 Doping TAGS-85 with Rare Earths

## 2.3.1 Motivation

As discussed in the previous chapter, attempts are being made to improve the electronic part of the figure of merit by distorting the density of states as suggested by Mahan and Sofo's model of the best thermoelectric [40]. Doping with rare earth elements can affect transport properties of a thermoelectric material because of three mechanisms:-

1) by introducing Dirac delta function like sharp peak in the density of states near the Fermi level, hence improving the Seebeck coefficient,
2) by causing substitutional defects and strains because of mass contrast, thereby increasing the phonon scattering,
3) by increasing carrier scattering or inducing the Kondo effect due to localized magnetic moments.

Bredl et al. studied [56] the low temperature specific heat as a function of magnetic field in $CeAl_3$, $CeCu_2Si_2$ and some alloys with Ce as a major constituent. The specific heat was observed to rise as we go below the Kondo temperature as for the case of dilute magnetic impurities, but once below a characteristic temperature, it falls again. At this temperature a transition from single ion Kondo regime to Kondo lattice regime occurs. This effect was attributed to the coherent coupling of the Kondo resonances at the Ce sites. This coherence leads to structure developing in the Kondo resonance density of states g(E) at the Fermi energy (figure 2.5).

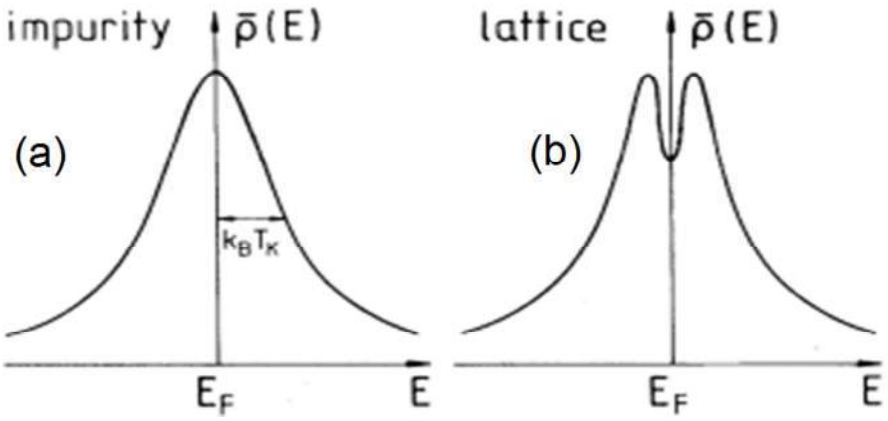


**Fig. 2.5.** Schematic drawings of the resonance density of states near the Fermi energy for the spin-1/2 Kondo problem with B = 0: (a) impurity case; (b) the form indicated by the experiment for the present Kondo lattices. Image adapted from Ref. [56].

Streglich et al. studied [57] the low-temperature Seebeck coefficient of the $CeAl_3$, $CeCu_{2.02}Si_{1.98}$ and $Ce_{0.9}Y_{0.1}Cu_2Si_2$ with magnetic field B = 0 and B = 4T. A peak was observed near the Kondo temperature as shown in figure 2.6. These results indicate that Ce can be a potential dopant for structuring the electronic density of states near Fermi level.

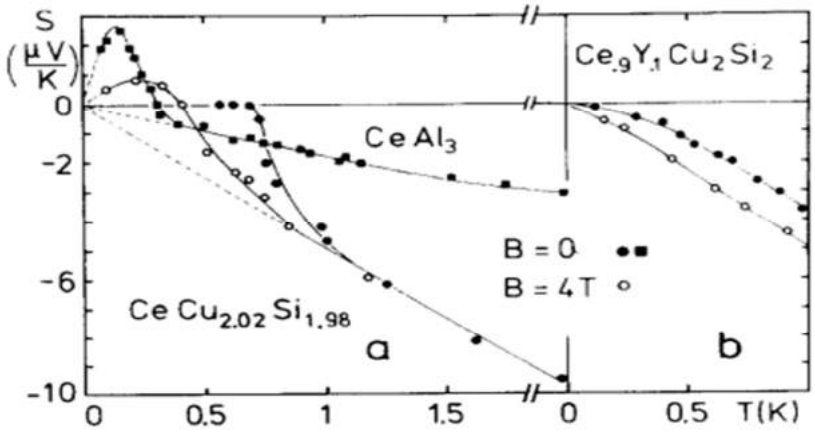


**Fig. 2.6.** Seebeck coefficient of (a) $CeAl_3$ and $CeCu_{2.02}Si_{1.98}$ and (b) $Ce_{0.9}Y_{0.1}Cu_2Si_2$. The dashed line in (a) is extrapolation from data at elevated temperatures to T = 0K. Image adapted from Ref. [57].

Levin et al. [58] studied the solid solutions based on $EuM_2Si_2$ ternary compounds (M stands for transition metals). They reported that the transition from $Eu^{2+}$ magnetic state to the interconfiguration fluctuation state ($Eu^{2.1+}$) may be realized through the state of a concentrated Kondo system when substituting Ge for Si. They said that this was due to the f-level approaching the Fermi level, decreasing the gap between the f-states and the Fermi level. They proposed that if this gap is small enough (few meV), resonant scattering mechanisms can influence the electronic structure parameters considerably.

## 2.3.2 Progress

The observation of Kondo effect in Ce and Eu doped alloys inspired Levin and co-workers [59] to investigate the possibility of creating resonant levels in TAGS-85 with the help of rare earth dopants. The composition of the samples they studied was $Ag_{6.52}Sb_{6.52}Ge_{36.96}Te_{49.00}Ce_{1.00}$ and $Ag_{6.52}Sb_{6.52}Ge_{36.92}Te_{49.00}Yb_{1.00}$. The X-ray diffraction patterns they obtained showed the rhombohedral TAGS-85 structure with some small impurity phase peaks which they attributed to the CeTe, $CeTe_2$ and YbTe precipitates.

Figure 2.7 shows the magnetic response of TAGS-85 + 1% Yb. The effective magnetic moment per Yb atom was calculated to be $0.88\mu_B$, less than the value of $4.50\mu_B$ for $Yb^{3+}$. Figure 2.8 shows the magnetic properties of TAGS-85 + 1% Ce as reported by Levin et al. The effective magnetic moment per Ce atom was calculated to be $1.21\mu_B$, less than the value of $2.54\mu_B$ for $Ce^{3+}$.

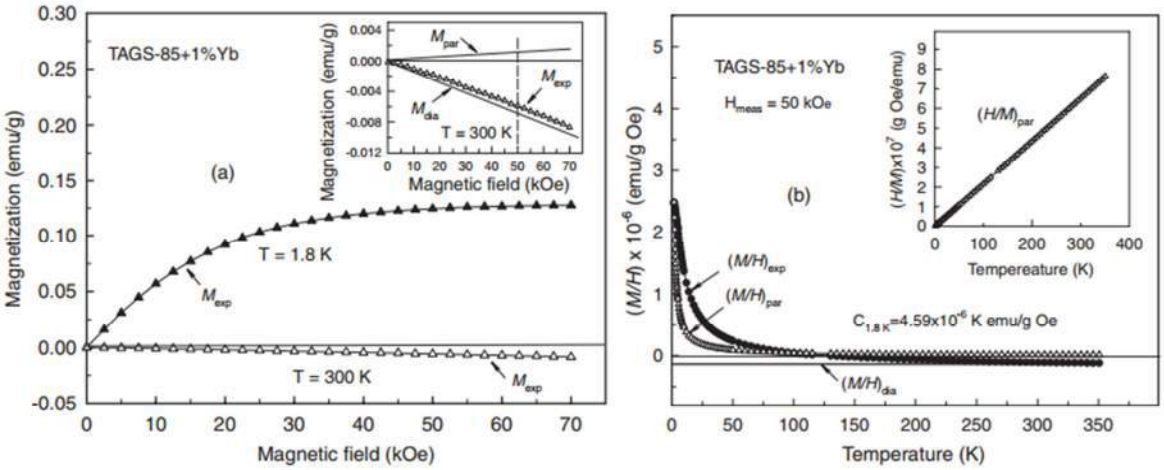


**Fig. 2.7.** (a) Magnetization, $M_{exp}$, versus magnetic field measured at T = 1.8K and T = 300K. The inset in (a) shows the calculated paramagnetic contribution, $M_{para}$, and diamagnetic contribution, $M_{dia}$, at T = 300K. (b) temperature dependence of $(M/H)_{exp}$ ratio and the paramagnetic and diamagnetic contributions. The inset in (b) shows the calculated $(H/M)_{para}$ ratio vs temperature. Image adapted from Ref. [59].

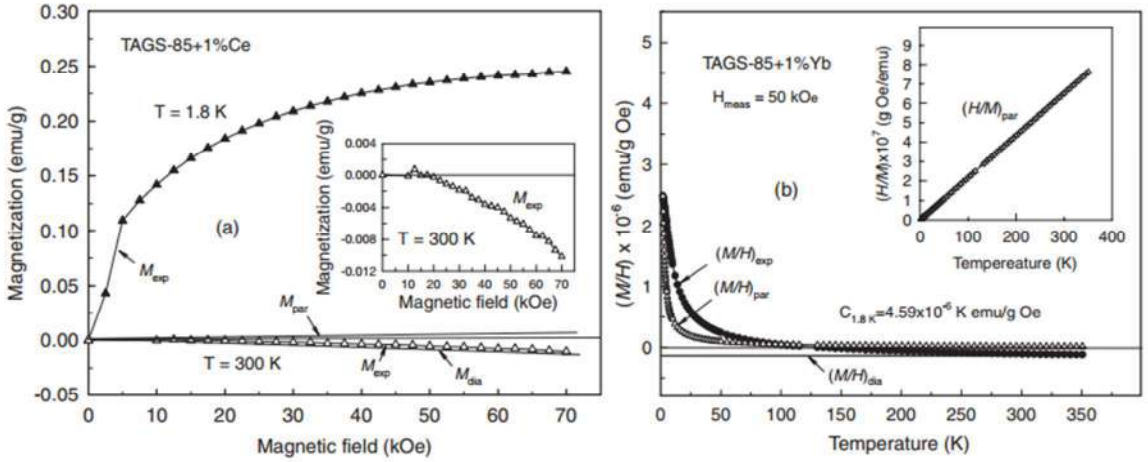


**Fig. 2.8.** (a) Magnetization, $M_{exp}$, versus magnetic field measured at T = 1.8K and T = 300K. The inset in (a) shows the $M_{exp}$ measured at T = 300K. (b) temperature dependence of $(M/H)_{exp}$ ratio and the paramagnetic and diamagnetic contributions. The inset in (b) shows the calculated $(H/M)_{para}$ ratio vs temperature. Image adapted from Ref. [59].

The Seebeck coefficient, S, electrical conductivity, σ, and the thermal conductivity, k, of pure TAGS-85 along with the doped samples as reported by Levin et al. are shown in figure 2.9. It was observed that the electrical conductivity remains essentially the same as that for the pure TAGS-85 samples, but the Seebeck coefficients were improved by almost 13% at T = 300K and 16% at T = 700K.

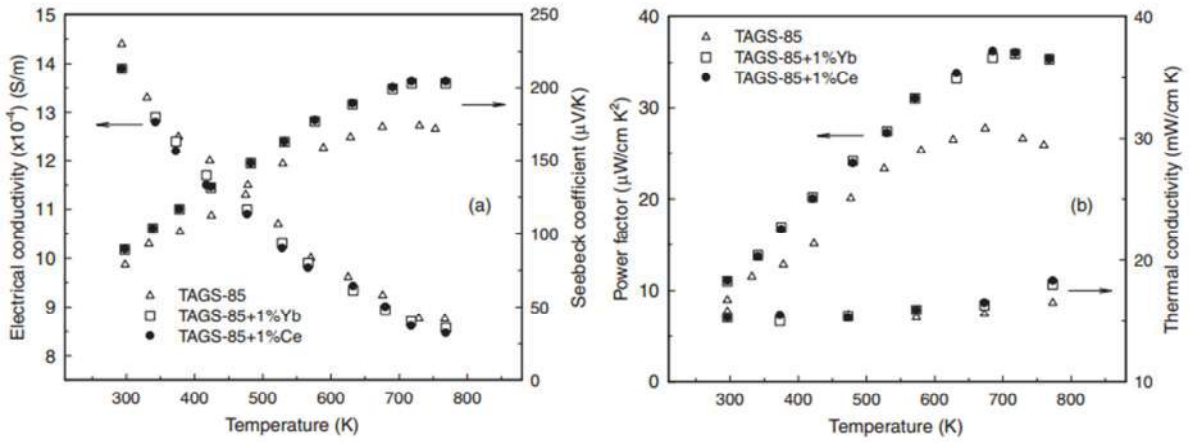


**Fig. 2.9.** Temperature dependencies of (a) electrical conductivity and Seebeck coefficient, (b) thermal conductivity and thermoelectric power factor of TAGS-85, TAGS-85 + 1% Yb and TAGS-85 + 1% Ce.

Although the improvement in the figure of merit for the Yb and Ce doped TAGS-85 as reported by Levin et al. is not as fascinating as in the case of Tl doped PbTe [39] reported by Heremans et al. where it was almost 100% higher than the pure PbTe values, yet it is still very encouraging. Levin et al. rule out the chance of improvement in Seebeck coefficient due to a decrease in the carrier concentration, because they did not see much difference in carrier concentrations of pure and doped samples after the Te NMR and Hall effect measurements. They suggest that this increase could be because of resonant levels, electron filtering due to lattice distortions or magnetic scattering. Since the electrical resistivity of these samples did not increase, the idea of resonant level scattering does not seem to fit here.

A year later [60], Levin et al. published the results of doping the TAGS-85 material with Dy, another rare earth element from the Lanthanides. The X-ray diffraction results and magnetic response of the material did not differ much from the Yb and Ce doped samples, but this time they got a much higher values for the effective magnetic moment per dopant atom, which were $10.7\mu_B$ for $Ag_{6.52}Sb_{6.52}Ge_{36.96}Te_{49}Dy_1$ (TAGS-85 + 1% Dy for Te), $9.5\mu_B$ for $Ag_{6.52}Sb_{6.52}Ge_{35.96}Te_{50}Dy_1$ (TAGS-85 + 1% Dy for Ge) and $10.1\mu_B$ for $Ag_{6.52}Sb_{6.52}Ge_{34.96}Te_{50}Dy_1$ (TAGS-85 + 2% Dy for Ge). These values were pretty close to the theoretical value ($10.64\mu_B$) for the magnetic moment of $Dy^{3+}$ ion.

Figure 2.10 shows the thermoelectric properties of Dy doped TAGS-85 as reported by Levin et al. It was evident that the Seebeck coefficient of the samples where Dy replaced Ge was larger than that for Dy replacing Te. The Seebeck coefficient for all the samples had a linear increase with temperature but with two distinct regions of different slopes. Around T = 525K, i.e. 302$^{o}$C, the slope decreases substantially which can be attributed to the transition from rhombohedral to cubic phase.

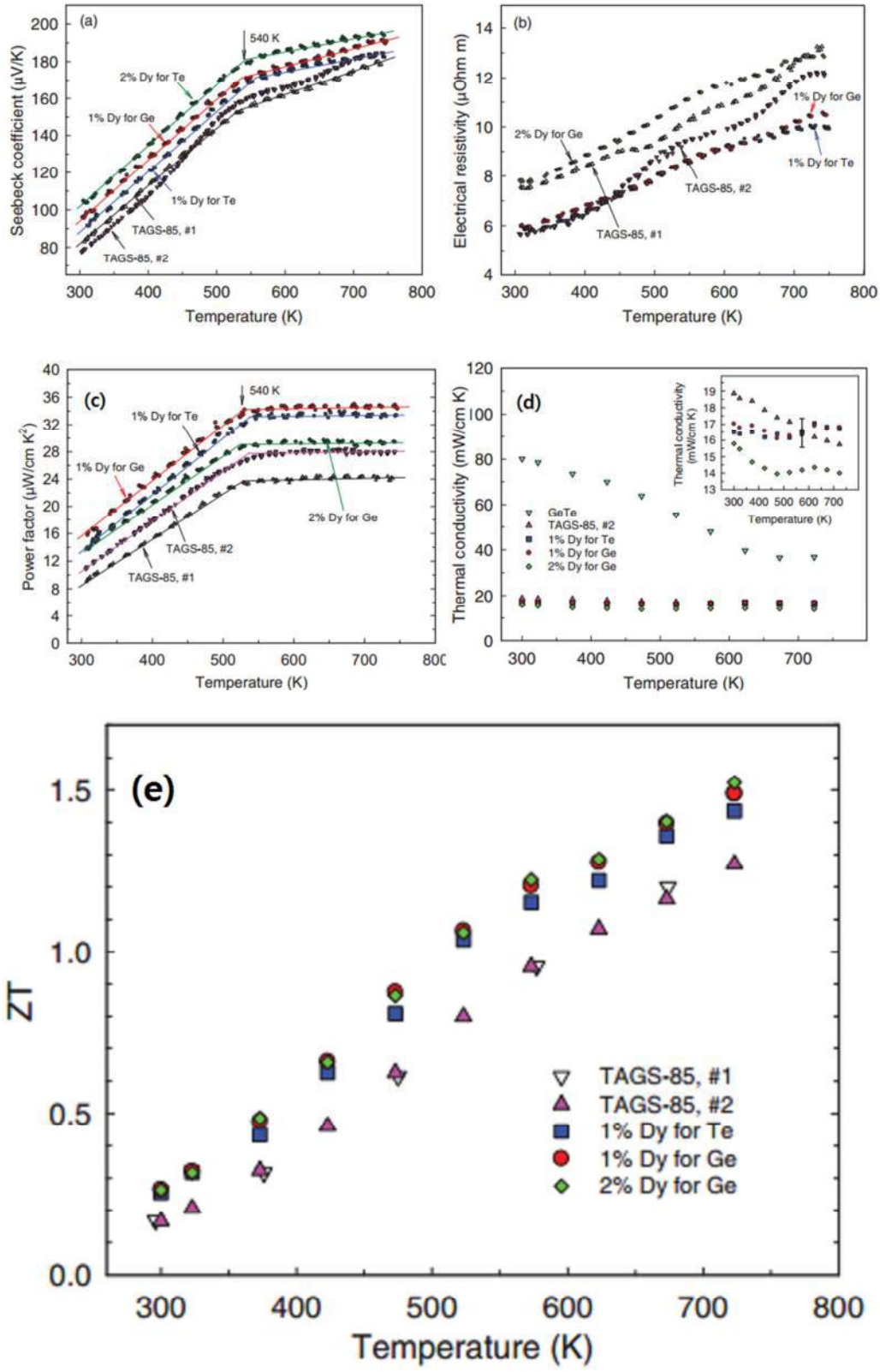


**Fig. 2.10.** Temperature dependence of (a) Seebeck coefficient, S, (b) electrical resistivity, ρ, (c) power factor, $S^2/\rho$, (d) thermal conductivity, k, and (e) figure of merit, $ZT = S^2T/\rho k$, of TAGS-85 #1, TAGS-85 #2, TAGS-85 + 1% Dy for Te, TAGS-85 + 1% Dy for Ge and TAGS-85 + 2% Dy for Ge. The results given for TAGS-85 #1 are the ones reported in the paper on Yb and Ce doping [59]. TAGS-85 #2 samples were prepared for this study. Image adapted from Ref. [60].

The temperature dependence of the electrical resistivity is typical of degenerate semiconductors where the increase is mostly attributed to the electron(hole)-phonon scattering. The power factor and the thermoelectric figure of merit (ZT) were also reported to have improved by doping. Levin et al. say that for the Dy doped samples, the resonant level peak in the density of states is not very probable since the 4f-electrons of the Dy atom are located deeply in the valance band although a small increase in the density of states of TAGS-85 can not be excluded. It is suggested that potential barriers can occur due to the lattice mismatched atomic sizes and the large magnetic moment of the Dy ions present in the lattice. These potential barriers can hinder the diffusion of low energy carriers from the colder end to the hotter end, hence increasing the seebeck coefficient.

## 2.4 Electronic Structure Calculations

Ab initio calculations on TAGS-85 have not been reported so far, but it would be useful to have a look at the DFT calculations on Ag and Sb doped GeTe [61] performed by Hoang, et al. They assumed cubic structure for GeTe, the structure of the high temperature phase. They concluded that the monovalent and trivalent impurities tend to come close to one another and form impurity-rich clusters and the electronic structure of the host material is strongly perturbed by these impurities. There were impurity-induced bands associated with the trivalent impurities that split off from the conduction-band bottom with large shifts towards the valence band top. Figure 2.11 shows the band structure of doped and undoped GeTe along different high symmetry directions of the simple cubic Brillouin zone as reported by Hoang, et al.

The calculated band gap (at the Γ point) is 0.243 eV (larger than the experimental value [62] of ≈ 0.20 eV). Ag substituting Ge in GeTe results in a p-type system with Fermi level below the valance band maxima. Ag-induced band is the one that splits off from the valence band top represented by the dash-dotted curve in figure 2.11(b). On the other hand, Sb substitution of Ge results in an n-type system. Impurity-induced band associated with Sb substitution is the one that splits off from the conduction band bottom reducing the band gap as shown in figure 2.11(c). Simultaneous doping of Ag and Sb also help lift the impurity-induced band associated with Sb up in energy and increase the gap as is evident from figure 2.11(e). The non-degenerate band (ignoring spin degeneracy) is now at a lower energy than the nearly three-fold degenerate band. The splitting between the three-fold degenerate conduction band minima and the impurity induced band is 82.8 meV and 143.8 meV at the second (figure 2.11(d)) and fifth (figure 2.11(e)) nearest neighbor distances, respectively.

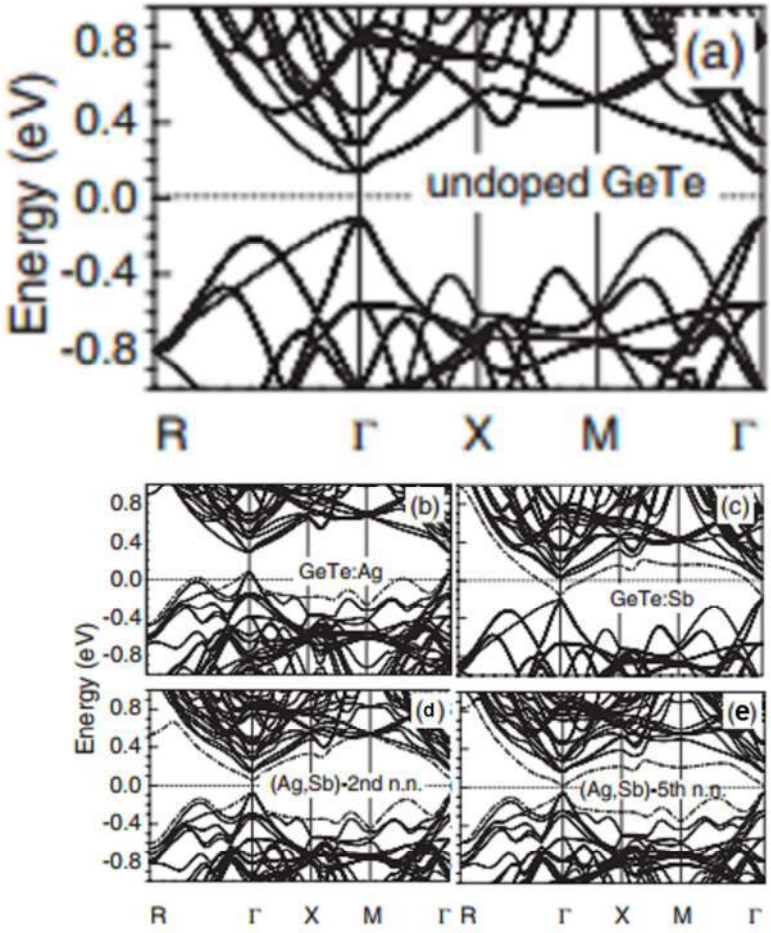


**Fig. 2.11.** Band structure of undoped GeTe and (Ag, Sb) doped GeTe. The Fermi level (0 eV) is set to the highest occupied states or in the band gap. Image adapted from Ref. [61].

Chapter-3

# Synthesis and Characterization

## 3.1. Sample Preparation

The sample materials were prepared by solid state reaction method. About 99.99% pure elemental ingredients were carefully weighed and mixed and then treated with heat in evacuated, sealed glass ampules. At high enough temperature, the elements react chemically to form the alloy.

The heat treatment plan is as follows:-

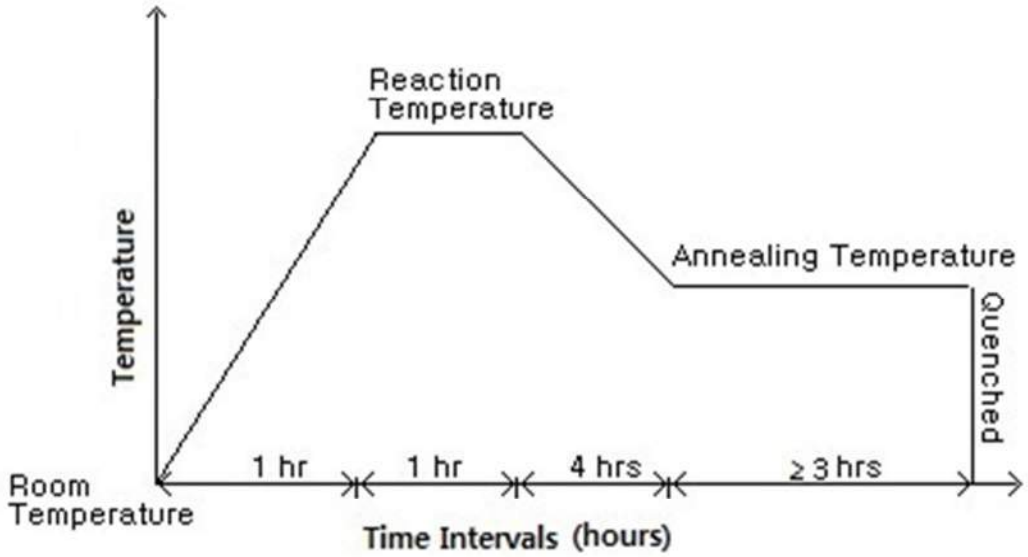


**Fig. 3.1.** Heat treatment plan for material synthesis.

The mixtures were heated from room temperature to the reaction temperature in one hour and kept at that temperature for another one hour while rotated so that the elements mix and react. Then for the next four hours, they were made to cool down to the annealing temperature. The samples were then annealed at that temperature for at least 3 hours before they were quenched to the room temperature.

The reaction temperature for most of the samples was 850$^{o}$C, but some samples were prepared at higher temperatures to see if it was possible to make the constituent elements mix and react better at those temperatures such that the impurity phases could be avoided. The X-ray diffraction patterns obtained showed that raising the reaction temperature did not help get rid of the impurity phases. No further measurements were done on those samples.

The annealing temperature for most of the samples was 600°C, but some samples were annealed at lower temperatures as well and minor fluctuations from the behavior of samples annealed at 600°C were observed. The annealing time was also altered for some samples to improve the grain size and it had considerable consequences which shall be reported in the results.

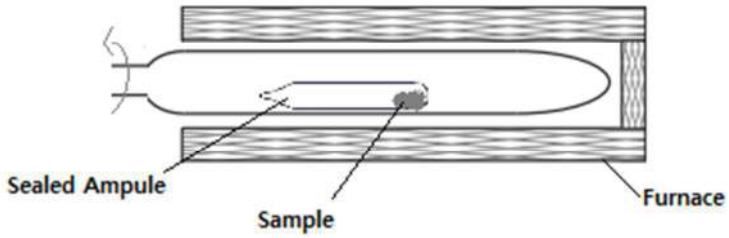


**Fig. 3.2.** Schematic diagram of heat treatment. At 850°C, the quartz tube was rotated slowly to help the elements mix and react chemically.

The prepared samples were then ground in an agate mortar and pestle to make fine powder of them which was used for the X-ray powder diffraction and to make cold pressed pellets for the Seebeck coefficient and electrical resistivity measurements.

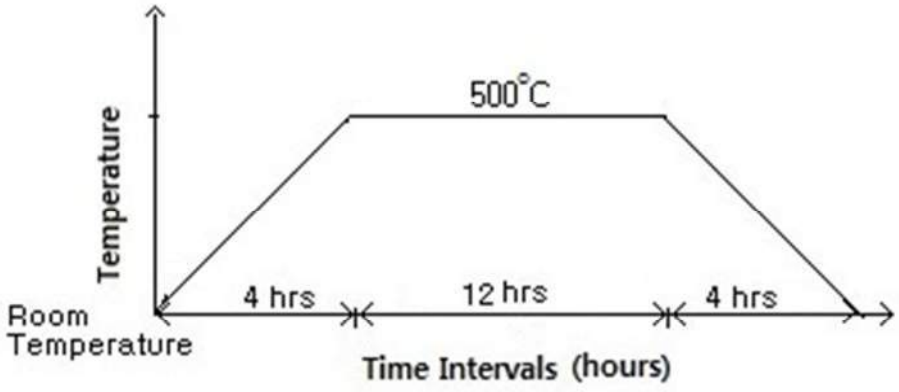


**Fig. 3.3**. Heat treatment plan for pellet sintering.

Pellets were made by application of 1 ton pressure and kept at 500°C for 12 hours in an evacuated, sealed quartz tube. For some samples, the sintered pellets were also characterized by X-ray diffraction to see if the small pressure and the heat treatment caused any change of phase.

## 3.2. X-ray Powder Diffraction

X-ray powder diffraction was used for phase analysis and studying the crystallographic properties of the samples. In our laboratory, the X-ray diffractometer (D8 Advance) has a tungsten filament in its X-ray tube to produce high energy electrons and copper as target

metal. When these high energy electrons collide with the copper target, they produce X-rays whose wavelength is a characteristic of the target metal, namely 1.5406A$^{o}$ for the $K_{\alpha 1}$ line of copper. The samples were scanned over a range of $2\theta = 20^{o} - 120^{o}$. The samples were scanned for long time (14 hours) to have less background noise and to see if there was some extra phase? The grains of TAGS-85 have [111] as preferred direction. The powdered samples were rotated at a frequency of 30 cycles per minute to provide a better statistical averaging of grain orientations and to avoid biased intensities due to the preferred orientation.


**Fig. 3.4.** D8 Advance X-ray diffractometer in Solid State Materials for Electronics group.

The data was refined by using the GSAS (General Structure Analysis System) software. ICSD (inorganic crystal structure database) was used to compare the diffraction pattern of the samples with the standard diffraction pattern of TAGS-85 material. Extra phase identification was performed by looking at the Chemical Open Database (COD 2013) using the EVA software.

The X-ray diffraction pattern of the sample holder showed peaks at $2\theta = 27.2^{o}$, $28.4^{o}$ and $29.2^{o}$.

## 3.3. Seebeck Coefficient Measurement

The seebeck coefficient measurement was performed on bar-shaped cold pressed pellets using the Quantum Design PPMS (Physical Properties Measurement System).

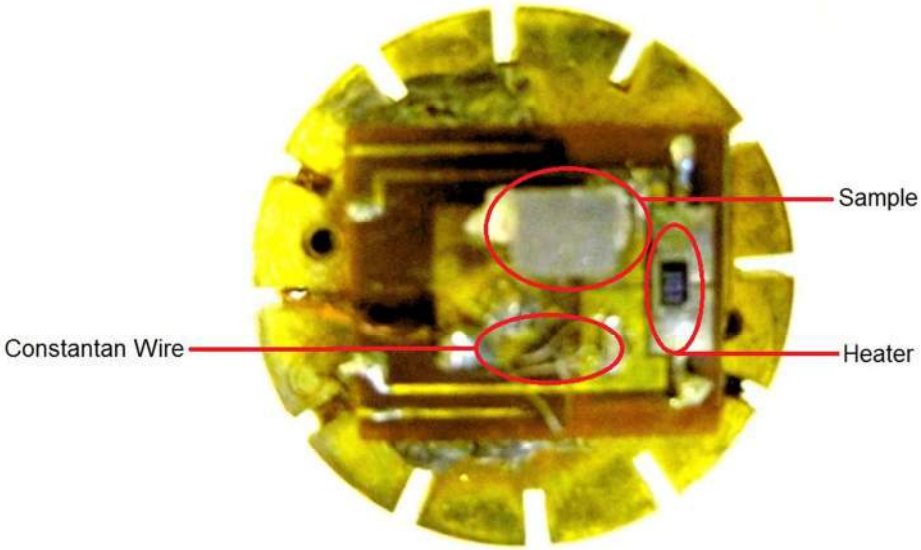


**Fig. 3.5.** Bar-shaped cold pressed pellet mounted on the sample holder for Seebeck coefficient measurement.

Seebeck coefficient values were measured over 50K to 300K temperature range with a step of 25K without applying any magnetic field. The system is computer controlled by the LabView software. Temperature difference of 1-2% was applied through the heater at the sample holder. Constantan wire was used as a reference material whose seebeck is known. Voltage build up across the samples was measured using the HEWLETT 3458A multimeter while across the constantan wire the voltage was measured by using the Agilent 3458A multimeter. Current to the heater was supplied by KEITHLEY 237 nanovoltmeter.

The voltages measured across the reference material and the sample were plotted against time. The data was fitted using the Origin8 software. The seebeck coefficient is related to voltage and temperature difference as:-

$$S = \Delta V/\Delta T \qquad (3.1)$$

From the known Seebeck coefficient of constantan wire, at every temperature step, ΔT was calculated. Then by dividing the voltage difference built across the sample at that particular temperature by the temperature difference, ΔT, the seebeck coefficient of the sample was calculated. The ratio ΔT/T was kept within 0.01-0.02. ΔT can be controlled by the voltage applied to the heater.

**Fig. 3.6.** Quantum Design PPMS in Solid State Materials for Electronics group.

## 3.4. Electrical Resistivity Measurement

Electrical resistivity of the samples was also measured on the same pellets by using the Quantum Design PPMS following the Kelvin method. Ohmic contacts were made with the sample holder using platinum wires and silver paint. A homogeneous current was applied across the length of the bar using the KEITHLEY 237 nanovoltmeter. The voltage between two closely spaced thin lines drawn by silver paint in the middle of the top surface was measured using the Agilent 3458A multimeter. At least 10 data points were obtained for each temperature by changing the applied current in the linear regime of the IV curve. The voltage measured at the surface was plotted against the current applied along the length of the bar to obtain the resistance (i.e. the slope of the linear IV curve) between the two lines at the top surface of the bar-shaped pellet.

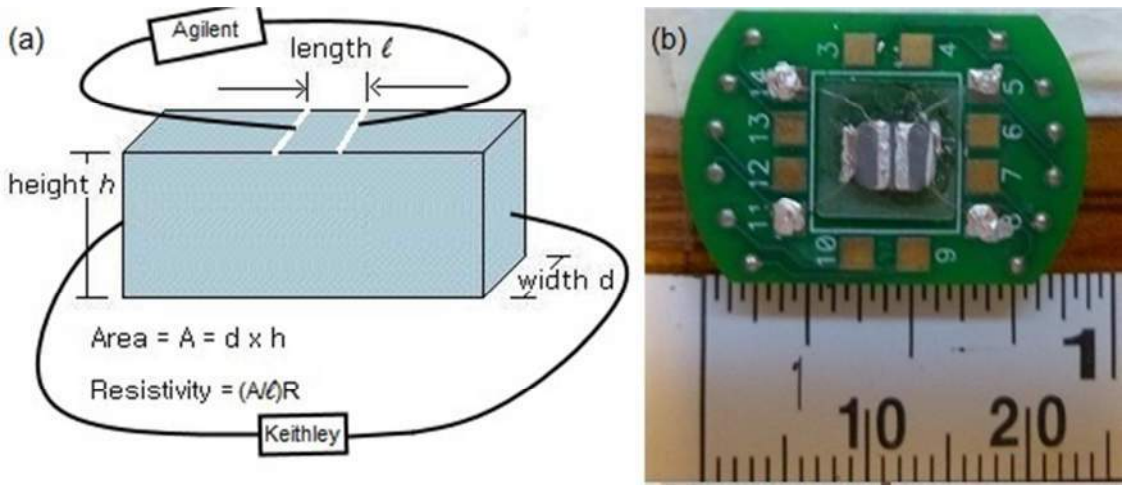


**Fig. 3.7.** (a) Schematic diagram of the bar-shaped pellet, (b) pellet on the sample holder.

The resistance values (R) measured at the temperatures ranging from 50K to 300K with a 5K temperature step were multiplied by the area of the  of the side faces and divided by the distance between the lines to get the resistivity ($\rho$ = RA/$\ell$).

## 3.5. Magnetic Susceptibility Measurement

Magnetic susceptibility was measured by using the Quantum Design MPMS-XL7 SQUID magnetometer. The SQUID is highly sensitive in detecting magnetic signals. It can detect magnetic moments down to 5 x $10^{-9}$emu.

**Fig. 3.8.** Quantum Design MPMS-XL7 in Solid State Materials for Electronics (SSME) group.

The Reciprocating Sample Option (RSO) [63] was used for measuring the magnetic moment. The RSO option is primarily used for samples with small magnetic moments. The measurement is done by moving the sample rapidly and sinusoidally through the SQUID pickup coils. The high quality servo motor and a digital signal processor (DSP) allow rapid measurements. During an RSO measurement, a shaft encoder on the servo motor tracks the position of the sample. While the sample moves through the coils, the MPMS MultiVu measures the SQUID's response to the magnetic moment of the sample.

The maximum standard size of the sample is 3mm in diameter x 3mm in height. Samples of this size or smaller effectively imitate a point dipole to an accuracy of 0.1%. The RSO sample rod assembly consists of one long, graphite sample rod; one short, graphite sample rod; and two centering plugs. RSO sample rods are specially designed to insert a drinking straw, which holds the sample, into the sample chamber. The centering plugs help keep a loose sample inside the straw and protect the straw from rubbing against the inside wall of the sample chamber. The RSO option includes a separate airlock because the RSO transport does not include a built-in airlock. The RSO transport is the mounting base for the airlock. The RSO airlock allows more rapid installation and removal of samples.

**Fig. 3.9.** Sample mounted inside a drinking straw attached to the centering plug, ready for MPMS RSO measurement.

The accuracy of an RSO sample measurement is determined by how well the sample is centered within the SQUID pickup coils. Before starting the measurement, it is advisable to first center the sample. The RSO centering measurement is faster and has greater sensitivity. If the sample is not centered well, the coils read only part of the magnetic moment of the sample.

The samples were weighed before the measurements. A field of 1000 Oe (sometimes 5000 Oe) was applied and the samples were cooled down to 5K then scanned with a 5K step up to 300K. From the measured data, the values for the magnetic moment of the samples were obtained. These values were divided by the number of moles calculated from the mass and the chemical formula of the samples, to obtain the magnetization. The measured susceptibility, $\chi$, was calculated by dividing this magnetization by the strength of the applied magnetic field. The measured susceptibility has a diamagnetic contribution, $\chi_{dia}$, as well which needs to be subtracted to get the paramagnetic susceptibility, $\chi_{para}$.

$$\chi_{para} = \chi - \chi_{dia} \qquad (3.2)$$

The diamagnetic susceptibility of the sample was calculated by following the approach of G. A. Bain and J. F. Berry as described in ref. [64]. The reciprocal of the slope of the plot $1/\chi_{para}$ vs T gives the Curie constant, C. The effective magnetic moment was determined by the formula:-

$$\mu_{eff.} = \sqrt{8C}\ \mu_B \qquad (3.3)$$

Chapter-4

# Results and Discussions – I

## 4.1 Pure TAGS-85

Chemical formula: $Te_{50}Ag_{6.52}Ge_{36.92}Sb_{6.52}$

Molecular weight: 242.92 amu

The details of the synthesis and characterization of the sample are the following:-

### i) Material Synthesis

Reaction temperature: 850$^{o}$C
Annealing temperature: 600$^{o}$C
Annealing time: 3 hours

### ii) X-ray Powder Diffraction

The X-ray powder diffraction showed that the sample contains only one phase and has a rhombohedral structure. The splitting of the (220) peak at $2\theta \approx 43^{o}$ is evident.

### iii) Seebeck Coefficient

The Seebeck coefficient was measured over 50K to 300K temperature range with a step of 25K without applying any magnetic field. The value at room temperature seems to be a bit less than the literature value given in section-2.2 for the samples prepared with fast cooling rates and higher density of defects. The focus of this project was on the electronic part of the figure of merit, so the cooling rate was kept low.

### iv) Electrical Resistivity

The electrical resistivity of the pure TAGS-85 was measured over 50K to 300K temperature range with a step of 5K without applying any magnetic field. The IV-curves obtained for each temperature point were linear. The room temperature value of the resistivity seems to be one order of magnitude higher than the expected value (as given in section-2.2). This can be some kind of instrumental error which appeared in all the electrical resistivity measurements. The resistivity shows a minimum around $T \approx 240K$.

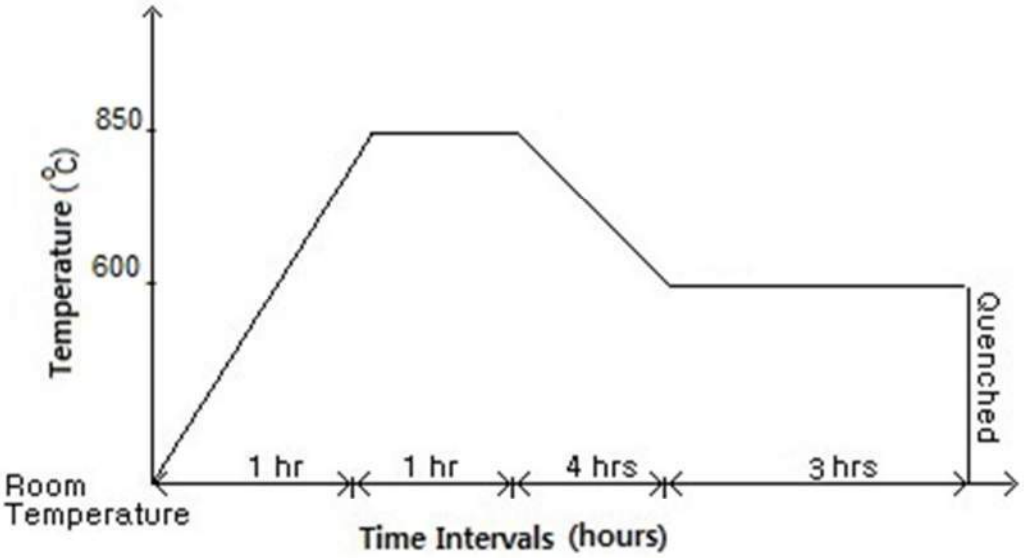


**Fig. 4.1.** Heat treatment plan for the pure TAGS-85 sample.

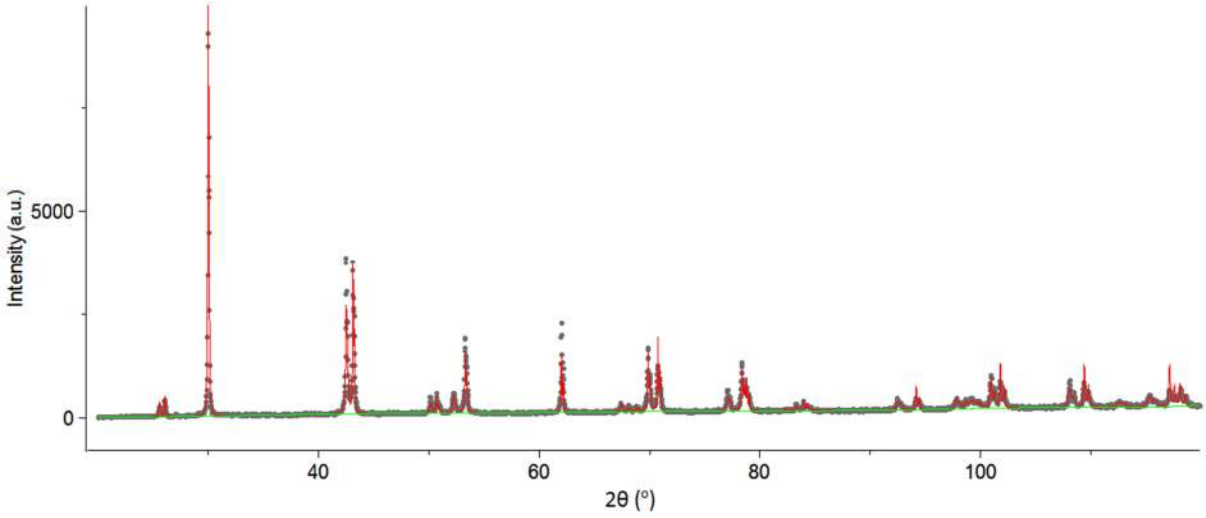


a = 4.27668(8)Å, α = 59.077(1)°

**Fig. 4.2.** X-ray diffraction of pure TAGS-85. The gray dots correspond to the measured data points. The fitted curve is plotted in red. “a” is the lattice parameter, “α” is the rhombohedral angle.

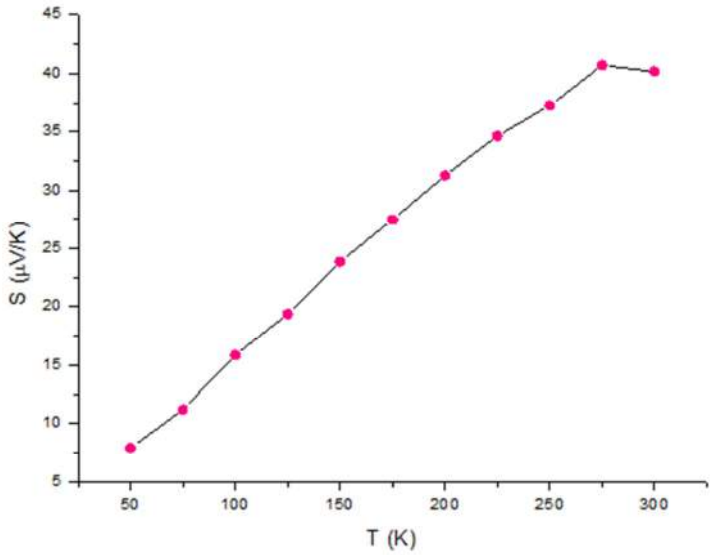


**Fig. 4.3.** Seebeck coefficient plotted against temperature for pure TAGS-85.

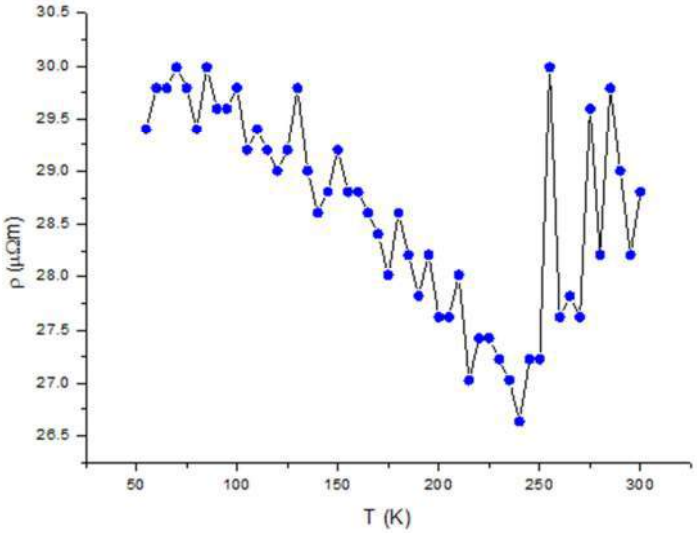


**Fig. 4.4.** Electrical resistivity of pure TAGS-85 plotted against temperature.

# 4.2 TAGS-85 + 1% Ho for Te

Chemical formula: $Te_{49}Ag_{6.52}Ge_{36.92}Sb_{6.52}Ho_1$

Molecular weight: 243.763 amu

The details of the synthesis and characterization of the samples are the following:-

## 4.2.1 Sample-1

### i) Material Synthesis

Reaction temperature: 850$^{o}$C
Annealing temperature: 600$^{o}$C
Annealing time: 3 hours

### ii) X-ray Powder Diffraction

The X-ray powder diffraction showed that the sample contains only one phase and has a rhombohedral structure. The splitting of the (220) peak at $2\theta \approx 43^{o}$ is evident.

### iii) Seebeck Coefficient

The Seebeck coefficient was measured over 50K to 300K temperature range with a step of 25K without applying any magnetic field. The values and behavior are pretty much similar to that of the pure TAGS-85 (figure 4.3).

### iv) Electrical Resistivity

The electrical resistivity of the sample was measured over 50K to 300K temperature range with a step of 5K without applying any magnetic field. The IV-curves obtained for each temperature point were linear. The electrical resistivity of this sample is higher than that of the pure TAGS-85 sample (figure 4.4). This could be because of scattering from magnetic impurities. We also see a minimum in resistivity around T ≈ 245K. A good fit of the resistivity data below T = 250K to the equation 1.13 was obtained to be $\rho \approx 48 - 1.4 \ln(0.6\,T)$.

### v) Magnetic Response

Magnetic measurements were performed on small piece of the sample material weighing 82.8mg, over the temperature range of 5 to 300K. The magnetic susceptibility of the sample did not show any diamagnetic contribution below 300K. This means that the effect of the magnetic impurities dominates.

The effective magnetic moment of the sample was calculated to be 1.06$\mu_B$. The atomic value of the magnetic moment of $Ho^{3+}$ ion is 10.4$\mu_B$.

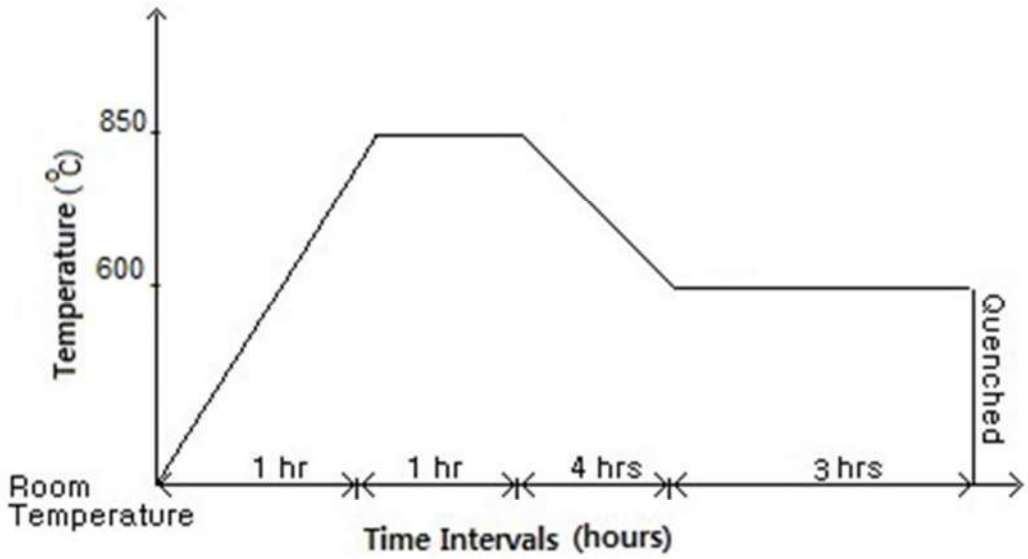


**Fig. 4.5.** Heat treatment plan for TAGS-85 + 1% Ho for Te, sample-1.

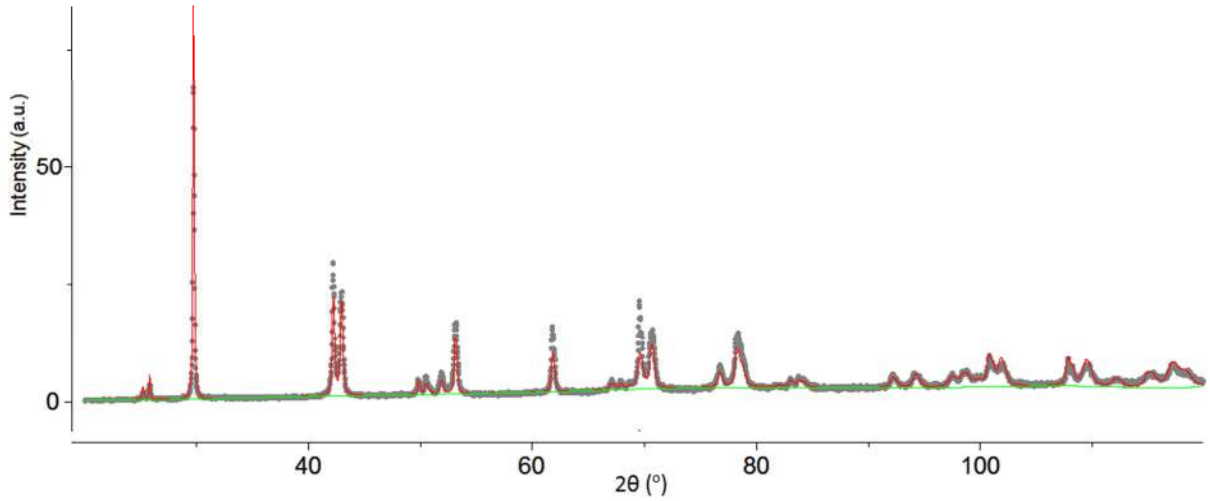


a = 4.2776(2)Å, α = 58.904(3)°

**Fig. 4.6.** X-ray diffraction of pure TAGS-85 + 1% Ho for Te, sample-1. The gray dots correspond to the measured data points. The fitted curve is plotted in red. "a" is the lattice parameter, "α" is the rhombohedral angle.

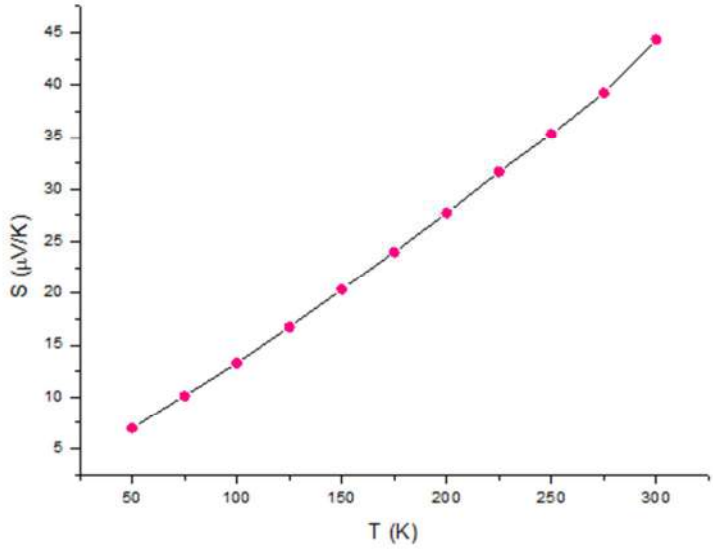


**Fig. 4.7.** Seebeck coefficient plotted against temperature for TAGS-85 + 1% Ho for Te, sample-1.

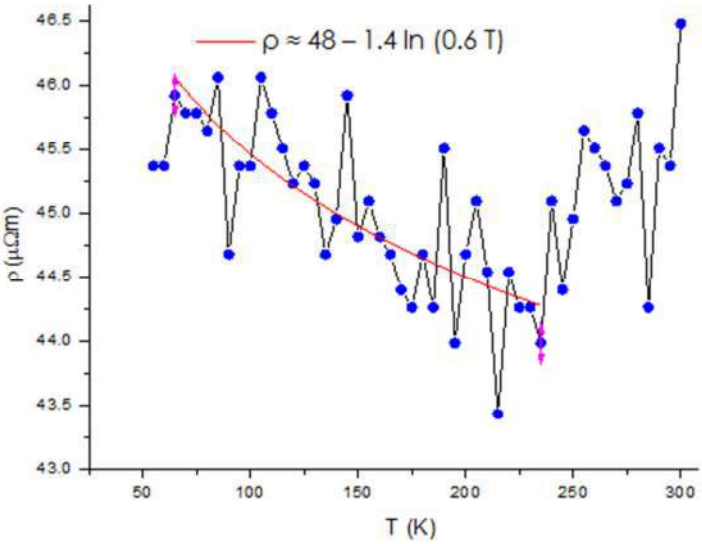


**Fig. 4.8.** Electrical resistivity of TAGS-85 + 1% Ho for Te, sample-1 plotted against temperature.

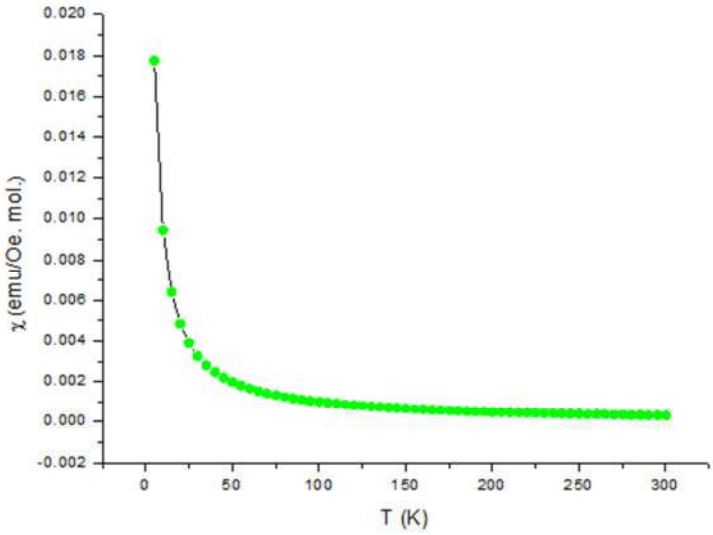

**Fig. 4.9.** Temperature dependence of the magnetic susceptibility of TAGS-85 + 1% Ho for Te, sample-1.

## 4.2.2 Sample-2

### i) Material Synthesis

Another sample of the same material but with a different heat treatment plan was prepared to see if it was possible to quench the high temperature cubic phase?

Reaction temperature: 850$^{o}$C
Annealing temperature: 500$^{o}$C
Annealing time: 3 hours
The cooling time from the reaction temperature to the annealing temperature was 3 hours.

### ii) X-ray Powder Diffraction

The X-ray powder diffraction showed that the sample contains two phases. It has a rhombohedral structure as is evident from splitting of the (220) peak at $2\theta \approx 42.7^{o}$. If we have a closer look, there is another single peak at $2\theta \approx 42.9^{o}$ which indicates existence of a cubic phase alongside the rhombohedral phase.

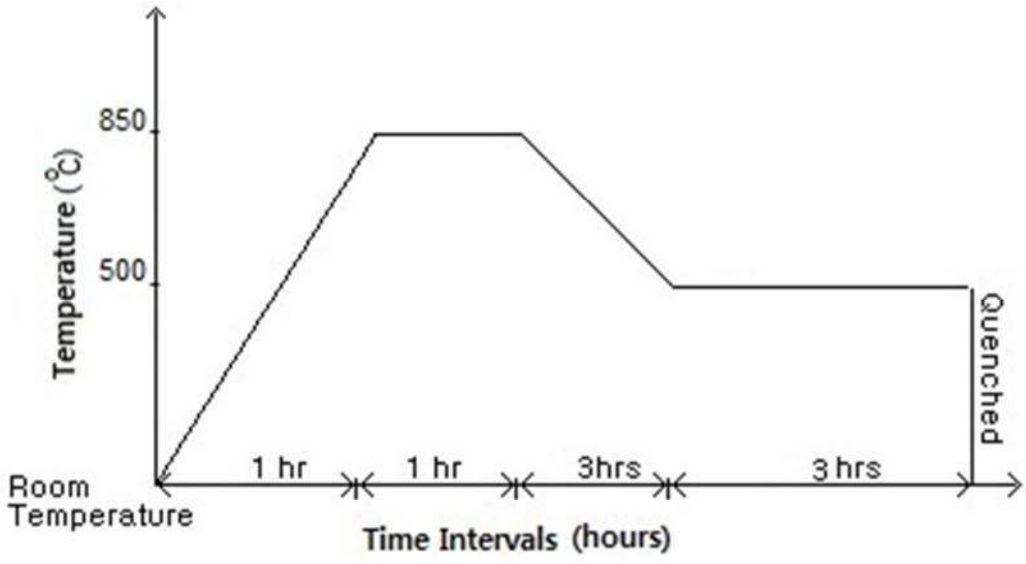


**Fig. 4.10.** Heat treatment plan for TAGS-85 + 1% Ho for Te, sample-2.

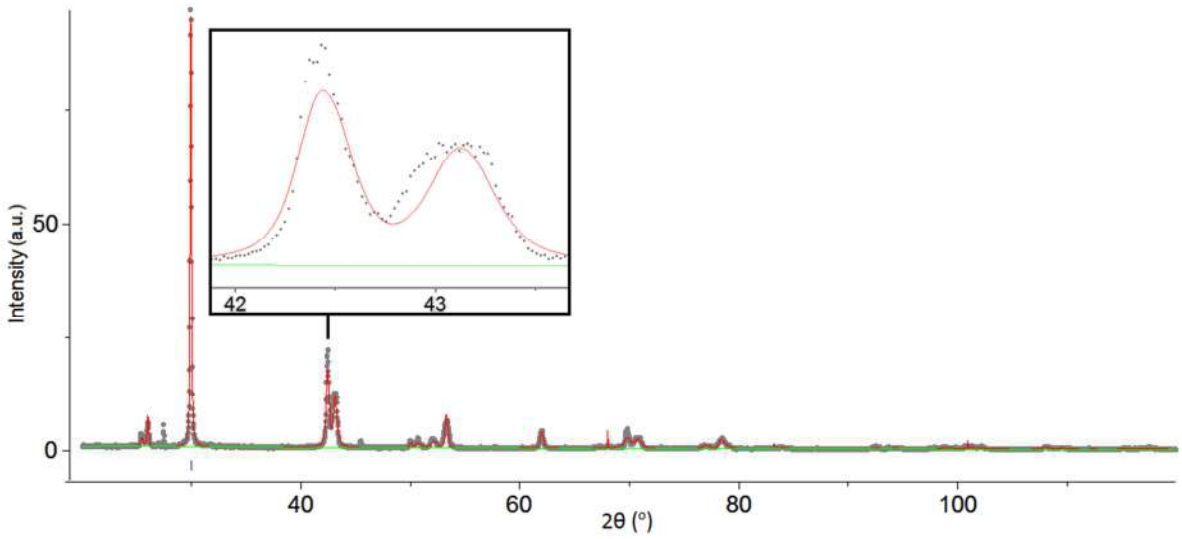


a = 4.27655(2)Å, α = 58.979(0)°

**Fig. 4.11.** X-ray diffraction of pure TAGS-85 + 1% Ho for Te, sample-2. The gray dots correspond to the measured data points. The fitted curve is plotted in red. The inset shows the splitting of the peak at 2θ ≈ 42.7° and the extra single peak at 2θ ≈ 42.9°. "a" is the lattice parameter, "α" is the rhombohedral angle.

# 4.3 TAGS-85 + 0.5% Ho for Te

Chemical formula: $Te_{49.5}Ag_{6.52}Ge_{36.92}Sb_{6.52}Ho_{0.5}$

Molecular weight: 243.4954 amu

The details of the synthesis and characterization of the sample are the following:-

## i) Material Synthesis

Reaction temperature: 850$^{o}$C
Annealing temperature: 600$^{o}$C
Annealing time: 10 hours

## ii) X-ray Powder Diffraction

The X-ray powder diffraction showed that the sample contains only one phase and has a rhombohedral structure. The splitting of the (220) peak at $2\theta \approx 43^{o}$ is evident.

## iii) Seebeck Coefficient

The Seebeck coefficient was measured over 50K to 300K temperature range with a step of 25K without applying any magnetic field. The Seebeck coefficient at room temperature is almost 55% higher than that of the pure TAGS-85 (figure 4.3).

## iv) Electrical Resistivity

The electrical resistivity of the sample was measured over 50K to 300K temperature range with a step of 5K without applying any magnetic field. The IV-curves obtained for each temperature point were linear.

Unlike the case of the pure TAGS-85 or the 1% Ho for Te doped sample, the resistivity of this sample has no minimum. It keeps on increasing slowly. If we combine this result with the enhancement of the Seebeck coefficient and compare them with the behavior of Tl doped PbTe discussed in section-1.3.5, we can say that there can be non-magnetic resonant levels in this sample.

## v) Magnetic Response

Magnetic measurements were performed on small piece of the sample material weighing 35.2mg, over the temperature range of 5 to 300K. The magnetic susceptibility of the sample did not show any diamagnetic contribution below 300K. This means that the effect of the magnetic impurities dominates.

The effective magnetic moment of the sample was calculated to be $0.68\mu_B$. The atomic value of the magnetic moment of $Ho^{3+}$ is $10.4\mu_B$.

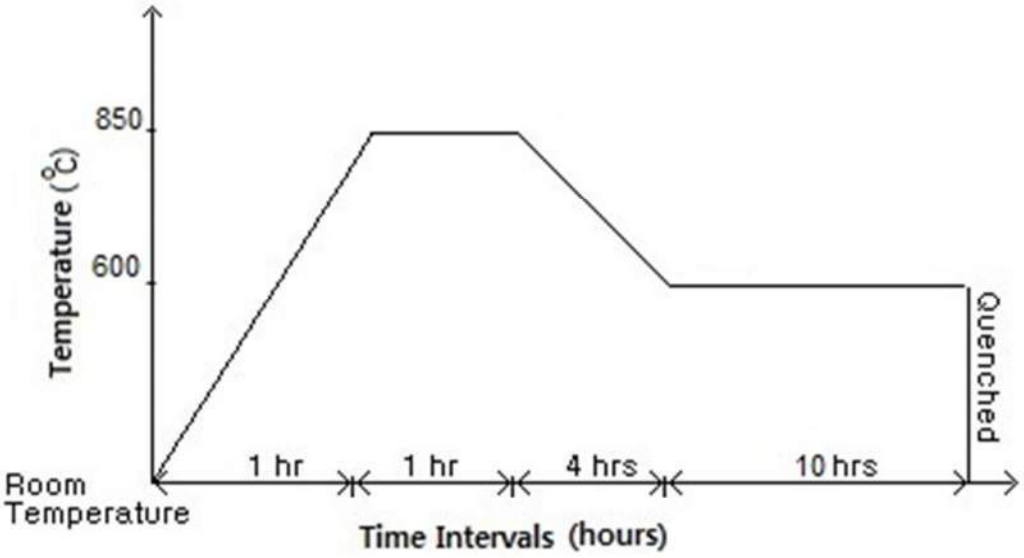


**Fig. 4.12.** Heat treatment plan for TAGS-85 + 0.5% Ho for Te.

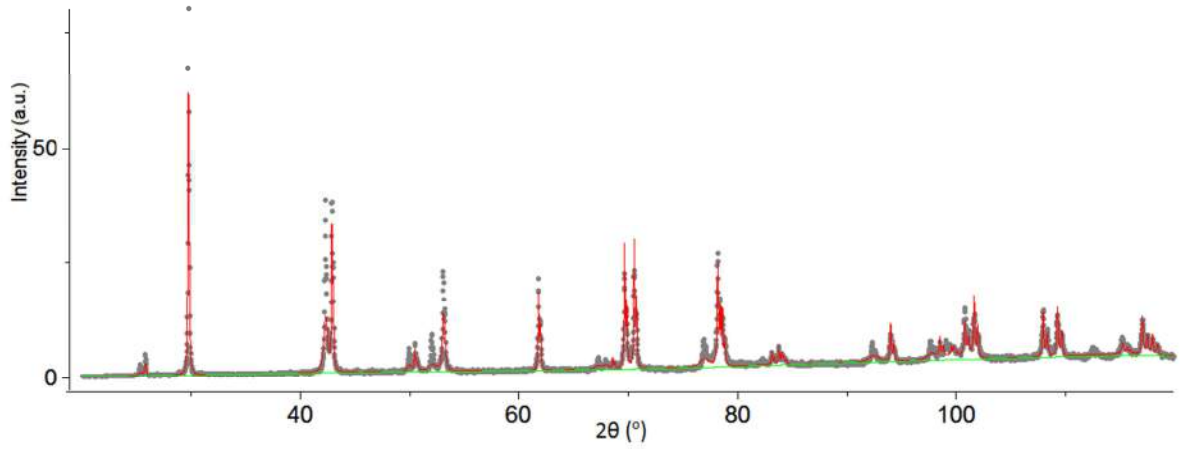


a = 4.27314(9)Å, α = 59.088(1)°

**Fig. 4.13.** X-ray diffraction of pure TAGS-85 + 0.5% Ho for Te. The gray dots correspond to the measured data points. The fitted curve is plotted in red. “a” is the lattice parameter, “α” is the rhombohedral angle.

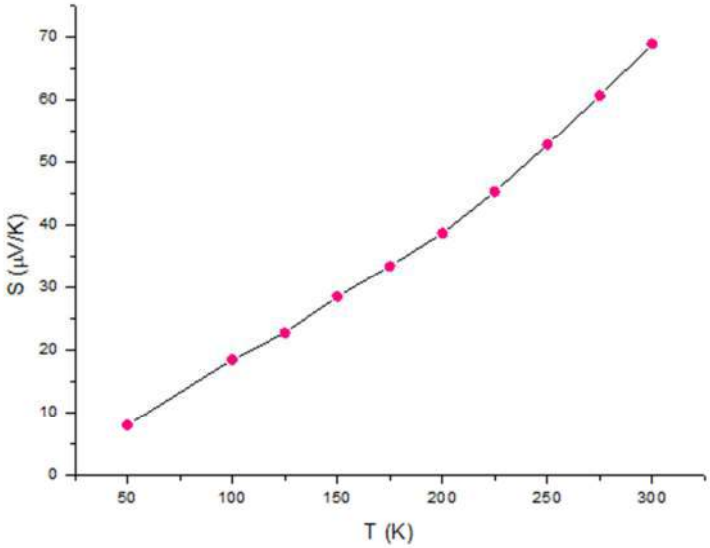


**Fig. 4.14.** Seebeck coefficient plotted against temperature for TAGS-85 + 0.5% Ho for Te.

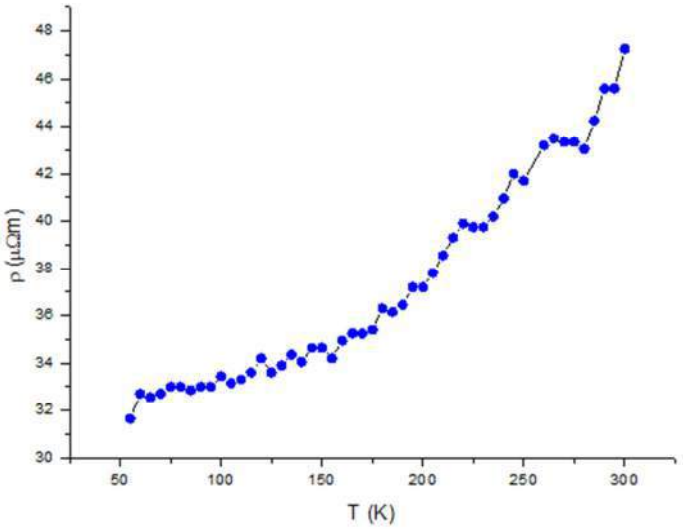


**Fig. 4.15.** Electrical resistivity of TAGS-85 + 0.5% Ho for Te plotted against temperature.

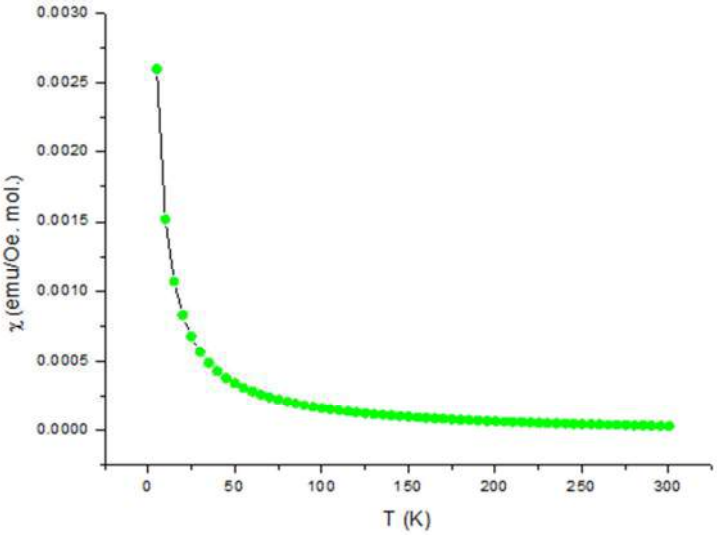


**Fig. 4.16.** Temperature dependence of the magnetic susceptibility of TAGS-85 + 0.5% Ho for Te.

# 4.4 TAGS-85 + 1% Tb for Te

Chemical formula: $Te_{49}Ag_{6.52}Ge_{36.92}Sb_{6.52}Tb_1$

Molecular weight: 243.6036 amu

The details of the synthesis and characterization of the samples are the following:-

## 4.4.1 Sample-1

### i) Material Synthesis

Reaction temperature: 850$^{o}$C
Annealing temperature: 600$^{o}$C
Annealing time: 12 hours

### ii) X-ray Powder Diffraction

The X-ray powder diffraction showed that the sample contains only one phase and has a rhombohedral structure. The splitting of the (220) peak at $2\theta \approx 43^{o}$ is evident.

### iii) Seebeck Coefficient

The Seebeck coefficient was measured over 50K to 300K temperature range with a step of 25K without applying any magnetic field. The Seebeck coefficient at room temperature is 33% higher than that of the pure TAGS-85 (figure 4.3).

### iv) Electrical Resistivity

The electrical resistivity of the sample was measured over 50K to 300K temperature range with a step of 5K without applying any magnetic field. The IV-curves obtained for each temperature point were linear.

Unlike the case of the pure TAGS-85 or the 1% Ho doped sample, the resistivity of this sample has no minimum. It keeps on increasing slowly. The electrical resistivity at room temperature for this sample is double that of the pure TAGS-85 sample (figure 4.4), this, along with the improvement in the Seebeck coefficient can be a signature of the existence of non-magnetic resonant levels in the conduction band.

### v) Magnetic Response

Magnetic measurements were performed on small piece of the sample material weighing 101.6mg, over the temperature range of 5 to 300K. The magnetic susceptibility of the

sample did not show any diamagnetic contribution below 300K. This means that the effect of the magnetic impurities dominates.

The effective magnetic moment of this sample was calculated to be $3\mu_B$. The atomic value of the magnetic moment of $Tb^{3+}$ ion is $9.77\mu_B$.

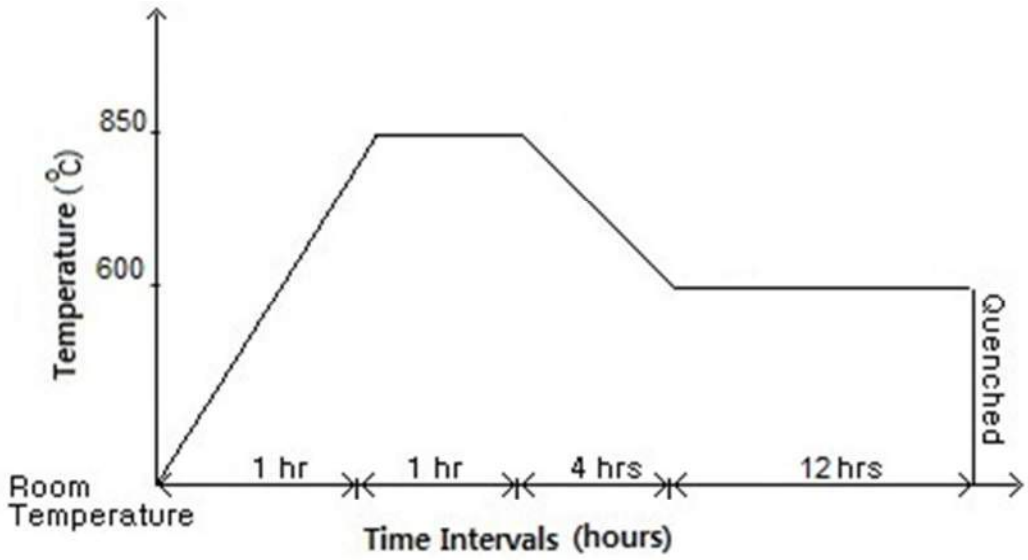


**Fig. 4.17.** Heat treatment plan for TAGS-85 + 1% Tb for Te, sample-1.

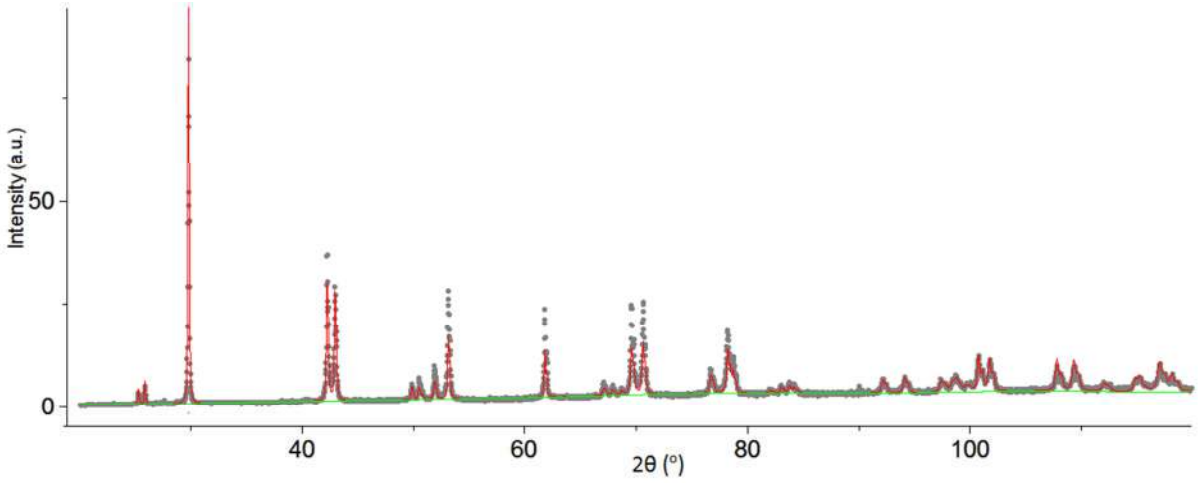


a = 4.2804(1)Å, α = 58.930(2)°

**Fig. 4.18.** X-ray diffraction of pure TAGS-85 + 1% Tb for Te, sample-1. The gray dots correspond to the measured data points. The fitted curve is plotted in red. "a" is the lattice parameter, "α" is the rhombohedral angle.

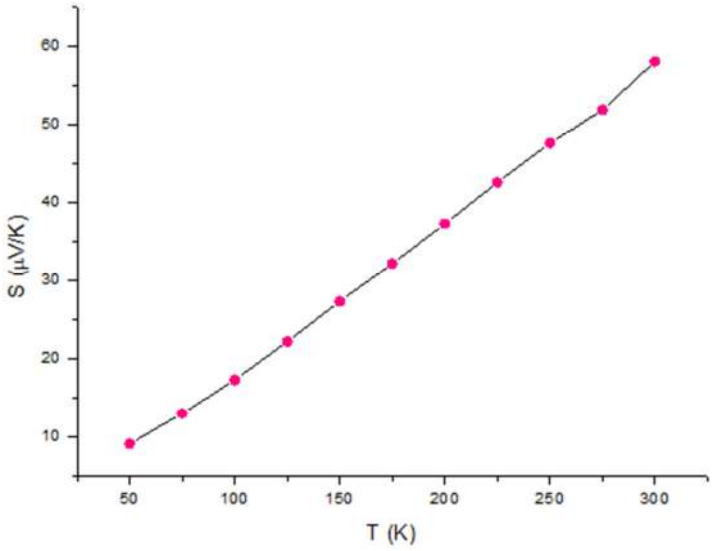


**Fig. 4.19.** Seebeck coefficient plotted against temperature for TAGS-85 + 1% Tb for Te, sample-1.

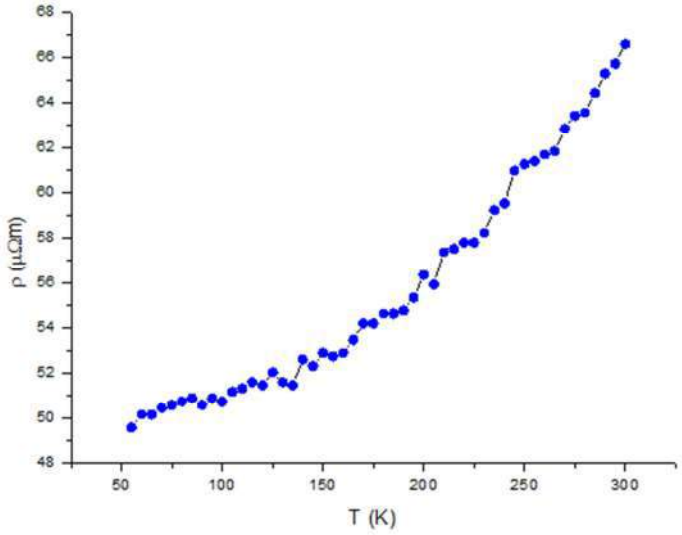


**Fig. 4.20.** Electrical resistivity of TAGS-85 + 1% Tb for Te, sample-1 plotted against temperature.

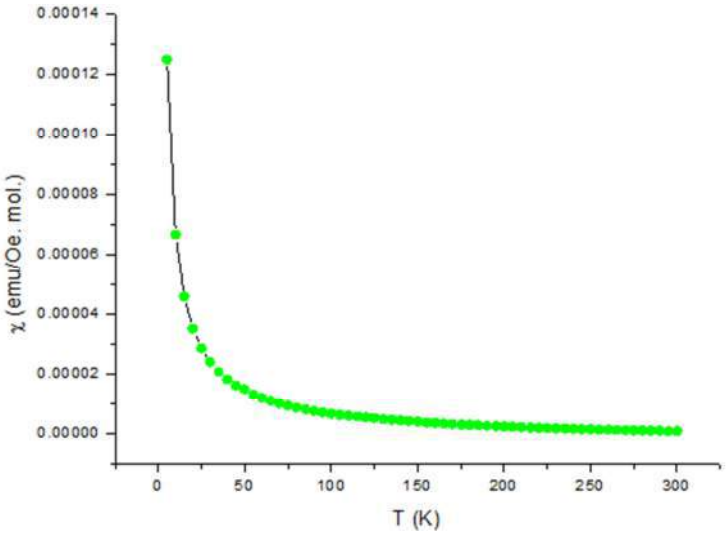


**Fig. 4.21.** Temperature dependence of the magnetic susceptibility of TAGS-85 + 1% Tb for Te, sample-1.

## 4.4.2 Sample-2

### i) Material Synthesis

The melting point of Ge is 938.25°C and that of Ag is 961.78°C. To see if raising the temperature above these values makes any difference, the elemental mixture was heated up to 970°C.

Reaction temperature: 970°C
Annealing temperature: 600°C
Annealing time: 3 hours

### ii) X-ray Powder Diffraction

The X-ray powder diffraction showed that the sample contains only one phase and has a rhombohedral structure. The splitting of the (220) peak at $2\theta \approx 43^{o}$ is evident.

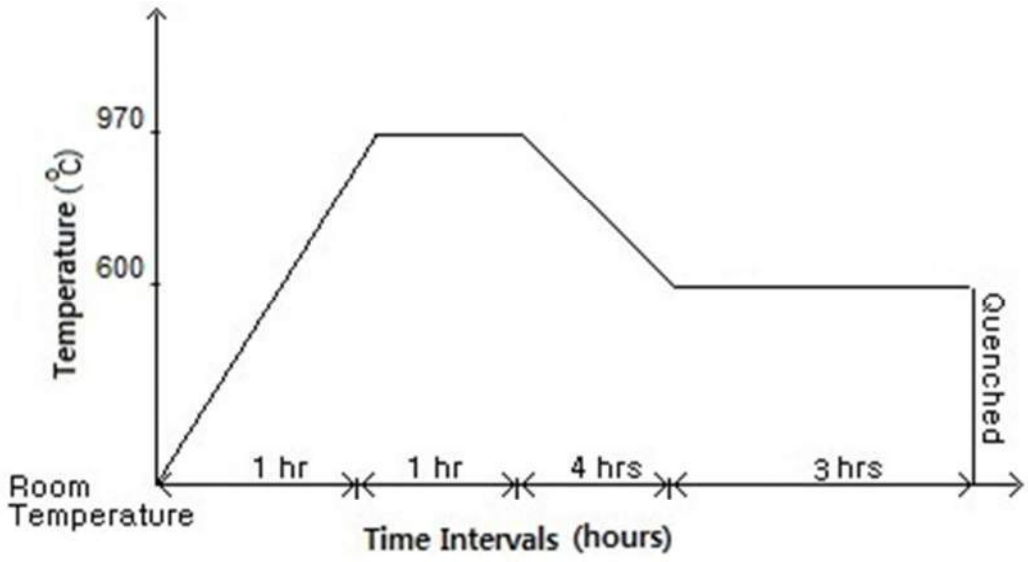


**Fig. 4.22.** Heat treatment plan for TAGS-85 + 1% Tb for Te, sample-2.

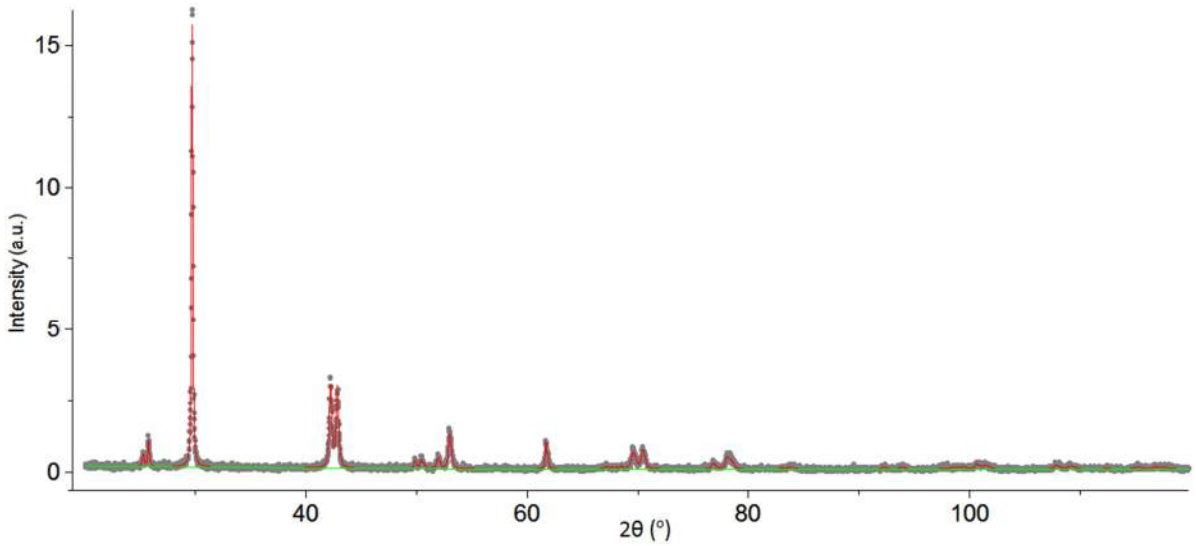


a = 4.27569(23)Å, α = 59.093(3)$^{o}$

**Fig. 4.23.** X-ray diffraction of pure TAGS-85 + 1% Tb for Te, sample-2. The gray dots correspond to the measured data points. The fitted curve is plotted in red. “a” is the lattice parameter, “α” is the rhombohedral angle.

## 4.4.3 Sample-3

### i) Material Synthesis

Another sample of the same material but with a different heat treatment plan was prepared to see if it was possible to quench the cubic phase?

Reaction temperature: 850$^{o}$C
Annealing temperature: 500$^{o}$C
Annealing time: 3 hours
The cooling time from reaction temperature to annealing temperature was 3 hours.

### ii) X-ray Powder Diffraction

The X-ray powder diffraction showed that the sample only one phase. It has a rhombohedral structure as evident from splitting of the (220) peak at $2\theta \approx 42.7^{o}$. No traces of cubic phase were observed.

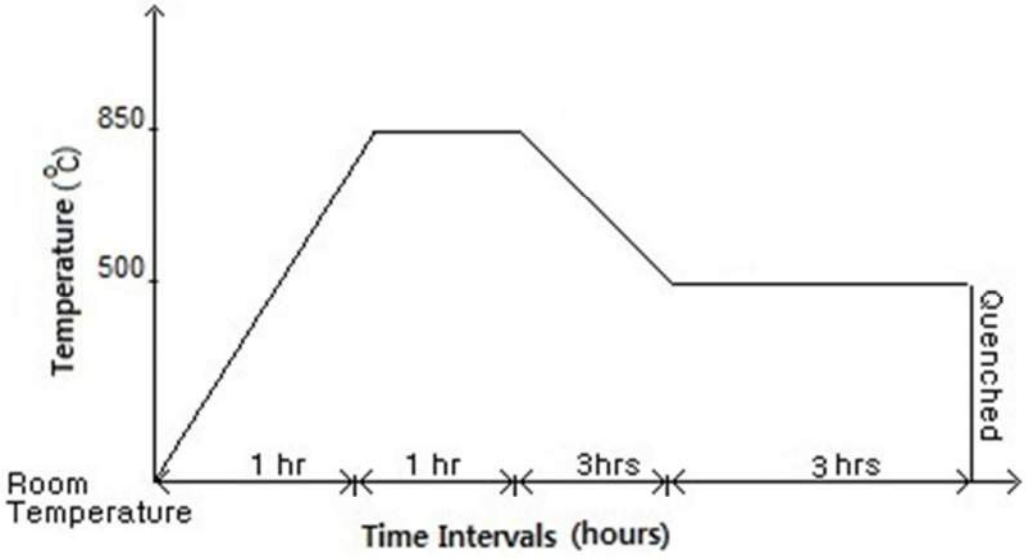


**Fig. 4.24.** Heat treatment plan for TAGS-85 + 1% Tb for Te, sample-3.

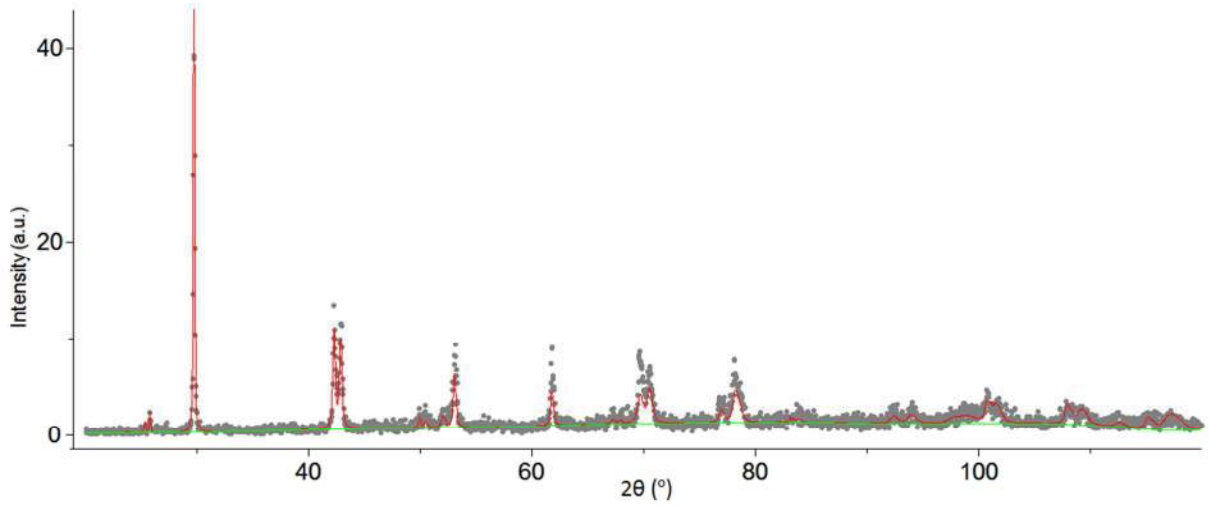


a = 4.2736(6)Å, α = 59.125(7)$^{o}$

**Fig. 4.25.** X-ray diffraction of pure TAGS-85 + 1% Tb for Te, sample-3. The gray dots correspond to the measured data points. The fitted curve is plotted in red. “a” is the lattice parameter, “α” is the rhombohedral angle.

# 4.5 TAGS-85 + 0.5% Tb for Te

Chemical formula: $Te_{49.5}Ag_{6.52}Ge_{36.92}Sb_{6.52}Tb_{0.5}$

Molecular weight: 243.427 amu

The details of the synthesis and characterization of the sample are the following:-

## i) Material Synthesis

Reaction temperature: 850$^{o}$C
Annealing temperature: 600$^{o}$C
Annealing time: 3 hours

## ii) X-ray Powder Diffraction

The X-ray powder diffraction showed that the sample contains has a rhombohedral structure of TAGS-85 material but it also contains $Ag_2Te$ impurity phase. The splitting of the (220) peak at $2\theta \approx 43^{o}$ is evident. The high intensity $Ag_2Te$ peaks appear at $2\theta \approx 31.2^{o}$, $38.8^{o}$, $39.25^{o}$ and $40.25^{o}$. The chances are high that the dopant atoms have gone to the Ag sites.

## iii) Seebeck Coefficient

The Seebeck coefficient was measured over 50K to 300K temperature range with a step of 25K without applying any magnetic field. The Seebeck coefficient at room temperature is almost 55% higher than that of the pure TAGS-85 (figure 4.3), like the case of TAGS-85 + 0.5% Ho for Te (figure 4.14).

## iv) Electrical Resistivity

The electrical resistivity of the sample was measured over 50K to 300K temperature range with a step of 12.5K without applying any magnetic field. The IV-curves obtained for each temperature point were linear.

Like the 0.5% Ho for Te doped sample, the resistivity of this sample has no minimum. It keeps on increasing slowly. If we combine this result with the enhancement of the Seebeck coefficient, we can say that there can be non-magnetic resonant levels in this sample.

## iv) Magnetic Response

Magnetic measurements were performed on small piece of the sample material weighing 21.6mg, over the temperature range of 5 to 300K. The magnetic susceptibility of the sample has diamagnetic behavior from 65K to 300K. This means that the diamagnetic contribution of the TAGS-85 matrix dominates.

The effective magnetic moment of the sample was calculated to be 0.42$\mu_B$. The atomic value of the magnetic moment of $Tb^{3+}$ ion is 9.77$\mu_B$.

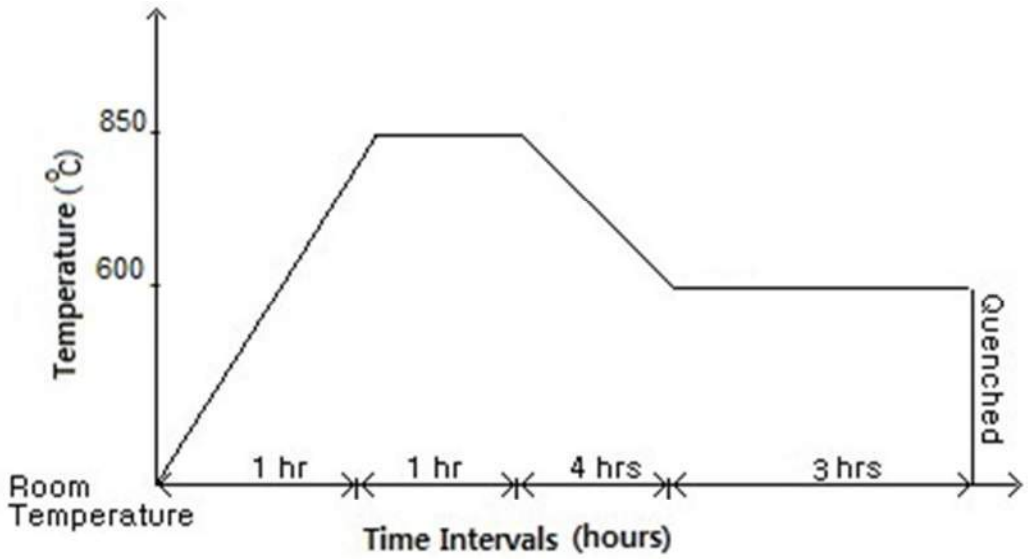


**Fig. 4.26.** Heat treatment plan for TAGS-85 + 0.5% Tb for Te.

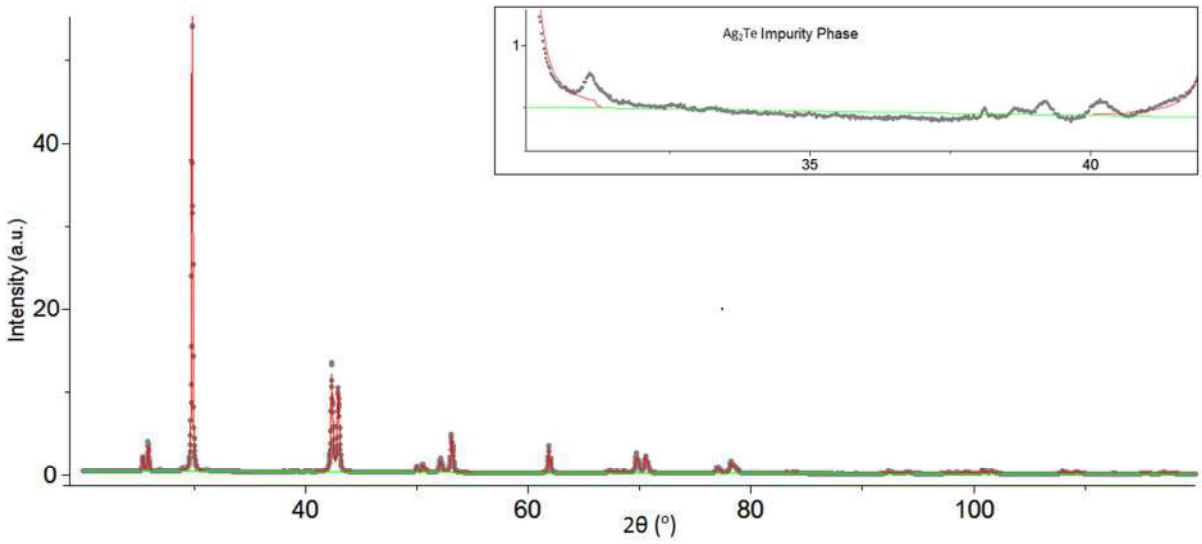


a = 4.27389(6)Å, α = 59.135(1)°

**Fig. 4.27.** X-ray diffraction of pure TAGS-85 + 0.5% Tb for Te. The gray dots correspond to the measured data points. The fitted curve is plotted in red. "a" is the lattice parameter, "α" is the rhombohedral angle. In the inset are some small peaks corresponding to the $Ag_2Te$ impurity phase.

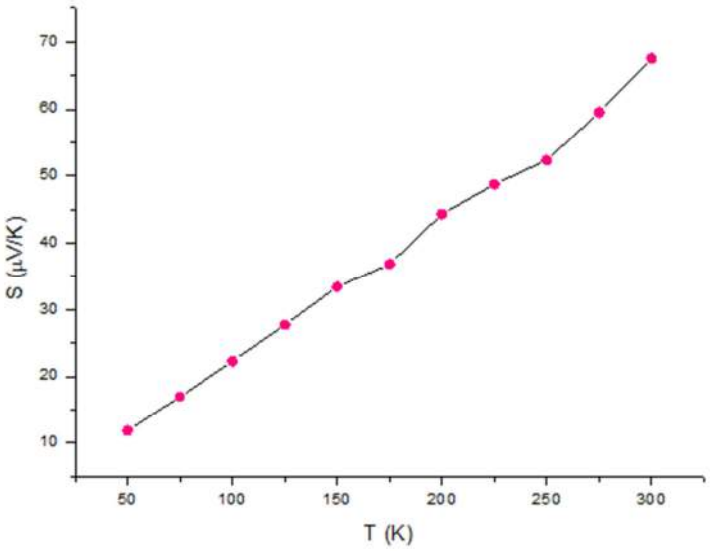


**Fig. 4.28.** Seebeck coefficient plotted against temperature for TAGS-85 + 0.5% Tb for Te.

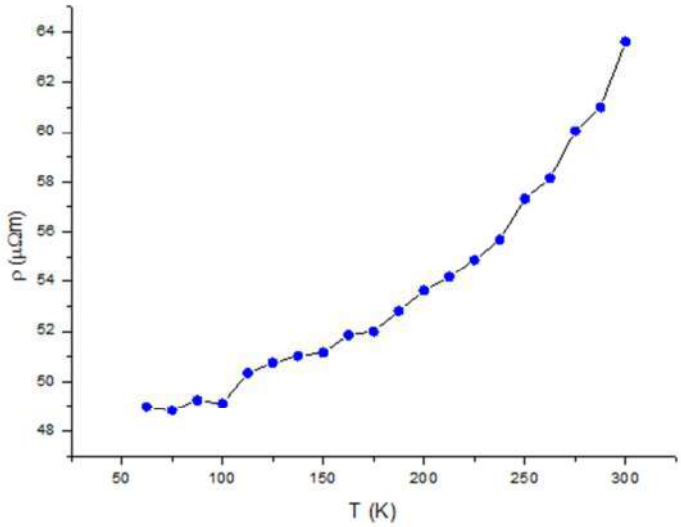


**Fig. 4.29.** Electrical resistivity of TAGS-85 + 0.5% Tb for Te plotted against temperature.

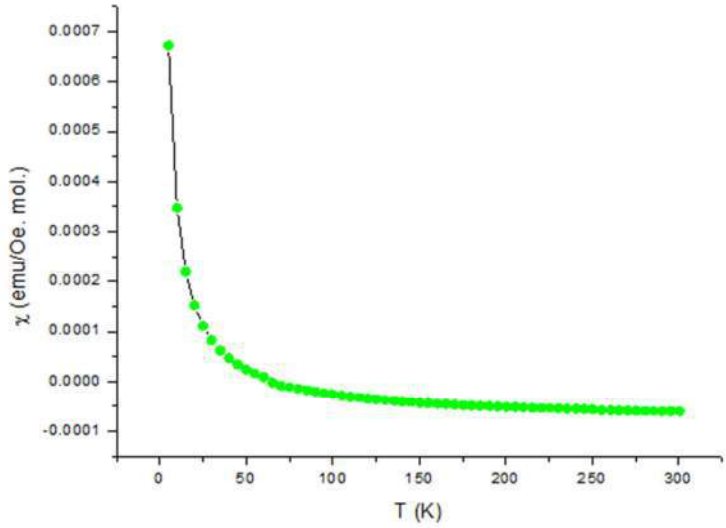


**Fig. 4.30.** Temperature dependence of the magnetic susceptibility of TAGS-85 + 0.5% Tb for Te.

Chapter-5

# Results and Discussions – II

Electrical properties of GeTe material emerge from a non-stoichiometric composition. It has been observed [65] that perfect stoichiometry can not be reached in GeTe samples prepared at high temperature and normal pressures. Damon, et al. reported [66] that each Ge vacancy in germanium telluride acts as doubly charge acceptor, hence providing two holes. Based on these reports, it was speculated that reducing the Ge content to add dopants in TAGS-85 could give rise to interesting consequences.

## 5.1 TAGS-85 + 1% Ho for Ge

Chemical formula: $Te_{50}Ag_{6.52}Ge_{35.92}Sb_{6.52}Ho_1$

Molecular weight: 244.853 amu

The details of the synthesis and characterization of the samples are the following:-

### 5.1.1 Sample-1

#### i) Material Synthesis

Reaction temperature: 850$^{o}$C
Annealing temperature: 600$^{o}$C
Annealing time: 14 hours

#### ii) X-ray Powder Diffraction

The X-ray powder diffraction showed that the sample has a rhombohedral structure but contains few traces of $Ag_2Te$ and $Ho_2O_3$ (space group $Ia\bar{3}$). The splitting of the (220) peak at $2\theta \approx 43^{o}$ is evident. The existence of silver telluride grains can be attributed to the deficiency of Ge which could have increased the probability of Te atoms reacting with Ag atoms to form telluride. The high intensity $Ag_2Te$ peaks appear at $2\theta \approx 31.2^{o}$, $38.8^{o}$, $39.25^{o}$ and $40.25^{o}$. The chances are high that the dopant atoms have gone to the Ag sites.

The peaks at $2\theta \approx 29.3^{o}$, $33.8^{o}$ and $48.6^{o}$ seem to correspond to $Ho_2O_3$ impurity phase which might have formed because of some oxygen left in the quartz ampule, but since no other element seemed to have oxidized, therefore, this explanation is not very satisfactory. These peaks were missing from other samples.

## iii) Seebeck Coefficient

The Seebeck coefficient was measured over 50K to 300K temperature range with a step of 25K without applying any magnetic field. The values and behavior are pretty much similar to that of the pure TAGS-85 (figure 4.3).

## iv) Electrical Resistivity

The electrical resistivity of the sample was measured over 50K to 300K temperature range with a step of 5K without applying any magnetic field. The IV-curves obtained for each temperature point were linear.

The electrical resistivity of this sample is higher than that of the pure TAGS-85 sample (figure 4.4). This could be because of scattering from magnetic impurities. We also see a minimum in resistivity around T ≈ 215K.

## v) Magnetic Response

Magnetic measurements were performed on small piece of the sample material weighing 10.5mg, over the temperature range of 5 to 300K. The magnetic susceptibility of the sample did not show any diamagnetic contribution below 300K. This means that the effect of the magnetic impurities dominates.

The effective magnetic moment of the sample was calculated to be 1.93$\mu_B$. The atomic value of the magnetic moment of $Ho^{3+}$ ion is 10.4$\mu_B$.

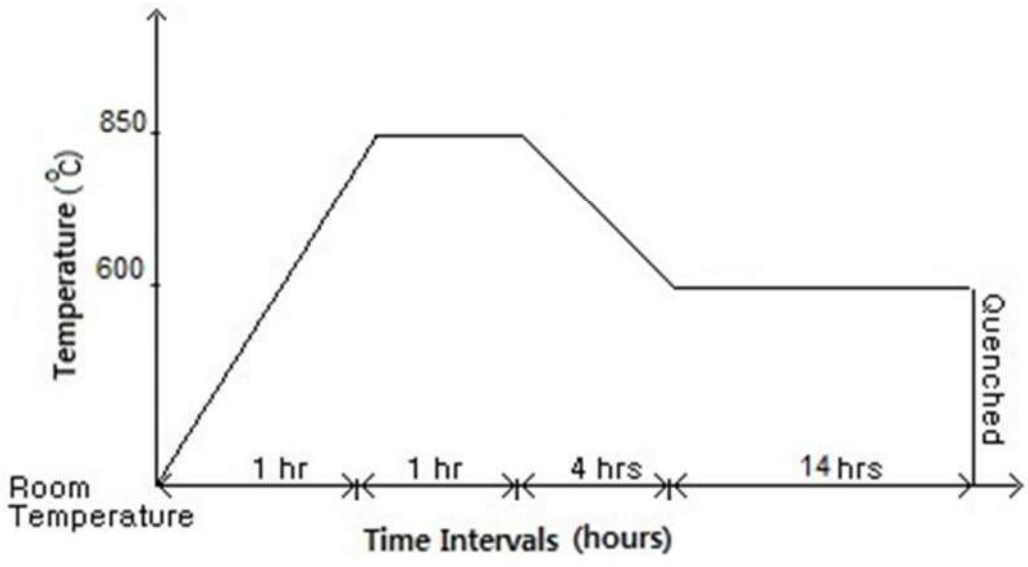


**Fig. 5.1.** Heat treatment plan for TAGS-85 + 1% Ho for Ge, sample-1.

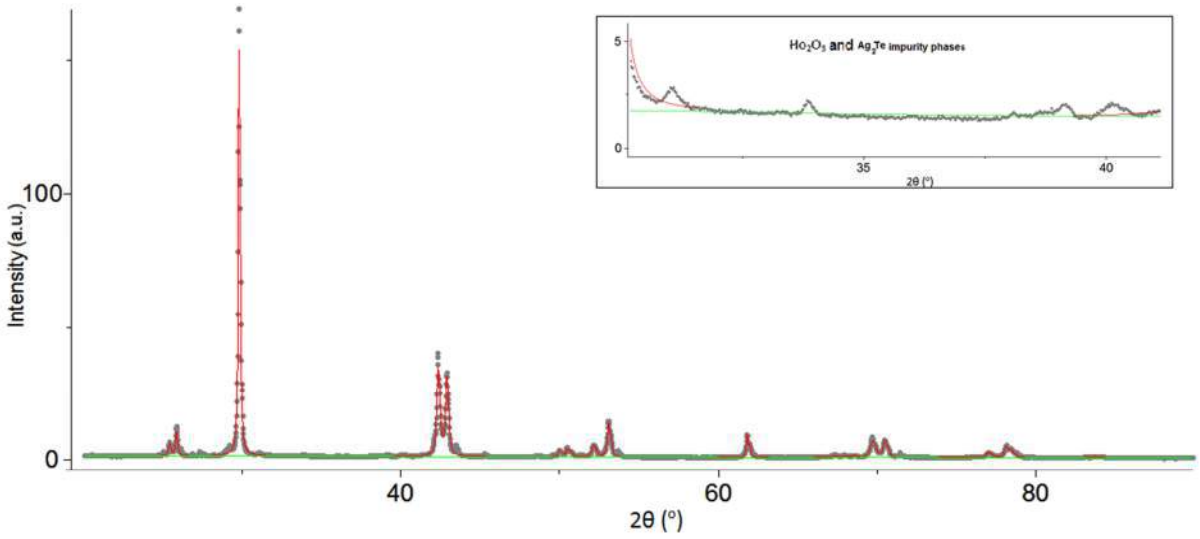


a = 4.27218(15)Å, α = 59.190(1)°

**Fig. 5.2.** X-ray diffraction of pure TAGS-85 + 1% Ho for Ge, sample-1. The gray dots correspond to the measured data points. "a" is the lattice parameter, "α" is the rhombohedral angle. The fitted curve is plotted in red. In the inset are some small peaks corresponding to the $Ag_2Te$ impurity phase and the 33.8° peak for the $Ho_2O_3$ impurity phase.

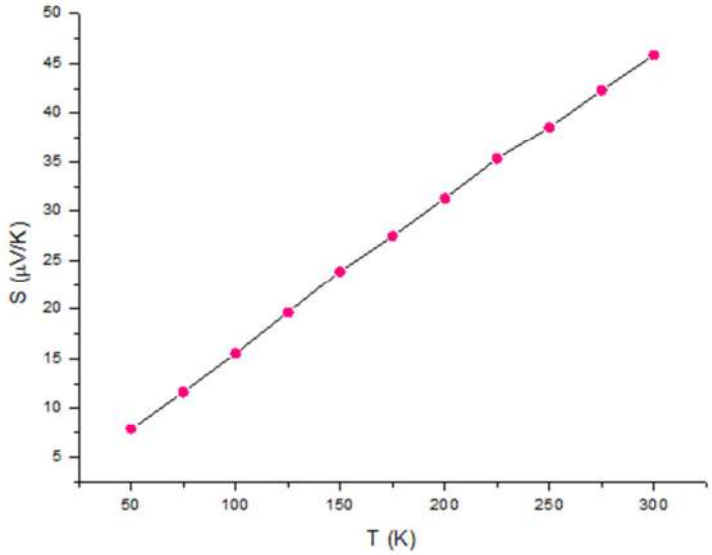


**Fig. 5.3.** Seebeck coefficient plotted against temperature for TAGS-85 + 1% Ho for Ge, sample-1.

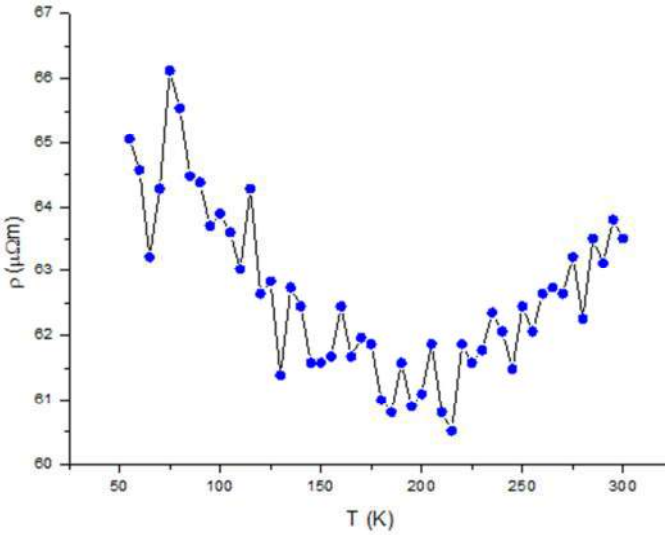


**Fig. 5.4.** Electrical resistivity of TAGS-85 + 1% Ho for Ge, sample-1 plotted against temperature.

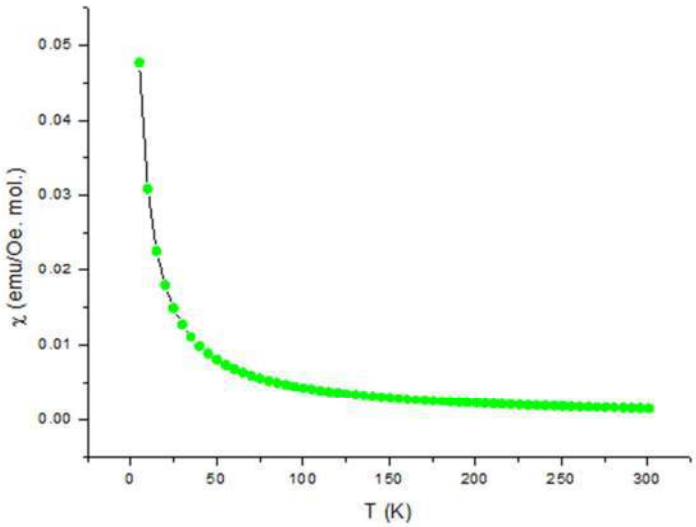


**Fig. 5.5.** Temperature dependence of the magnetic susceptibility of TAGS-85 + 1% Ho for Ge, sample-1.

## 5.1.2 Sample-2

### i) Material Synthesis

Reaction temperature: 850$^{o}$C
Annealing temperature: 600$^{o}$C
Annealing time: 3 hours

### ii) X-ray Powder Diffraction

The X-ray powder diffraction showed that the sample contains only one phase and has a rhombohedral structure. The splitting of the (220) peak at $2\theta \approx 43^{o}$ is evident.

### iii) Seebeck Coefficient

The Seebeck coefficient was measured over 50K to 300K temperature range with a step of 25K without applying any magnetic field. The values and behavior are pretty much similar to that of the pure TAGS-85 (figure 4.3).

### iv) Electrical Resistivity

The electrical resistivity of the sample was measured over 50K to 300K temperature range with a step of 12.5K without applying any magnetic field. The IV-curves obtained for each temperature point were linear.

The electrical resistivity of this sample is higher than that of the pure TAGS-85 sample (figure 4.4). This could be because of scattering from magnetic impurities. We do not see a minimum in resistivity but there is a plateau of constant resistivity.

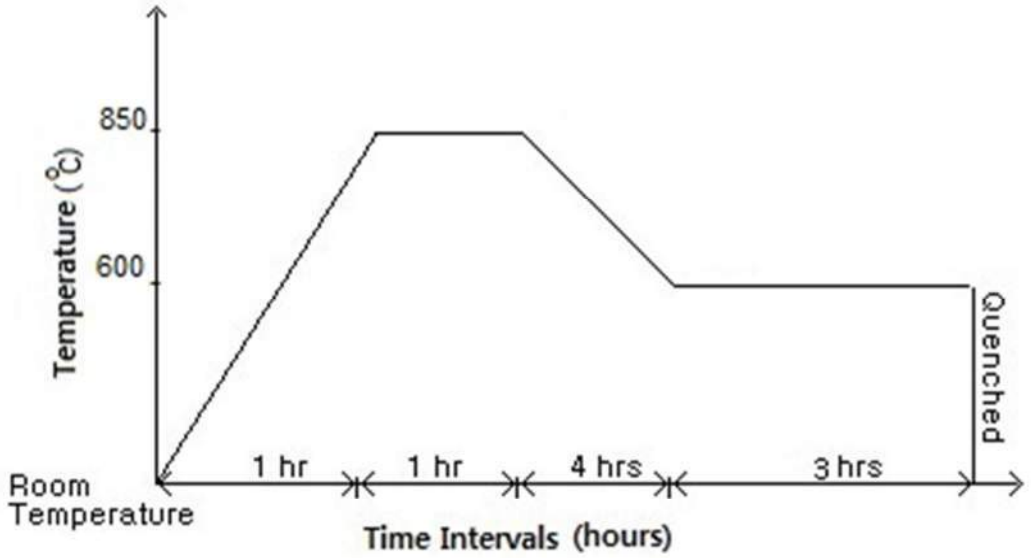


**Fig. 5.6.** Heat treatment plan for TAGS-85 + 1% Ho for Ge, sample-2.

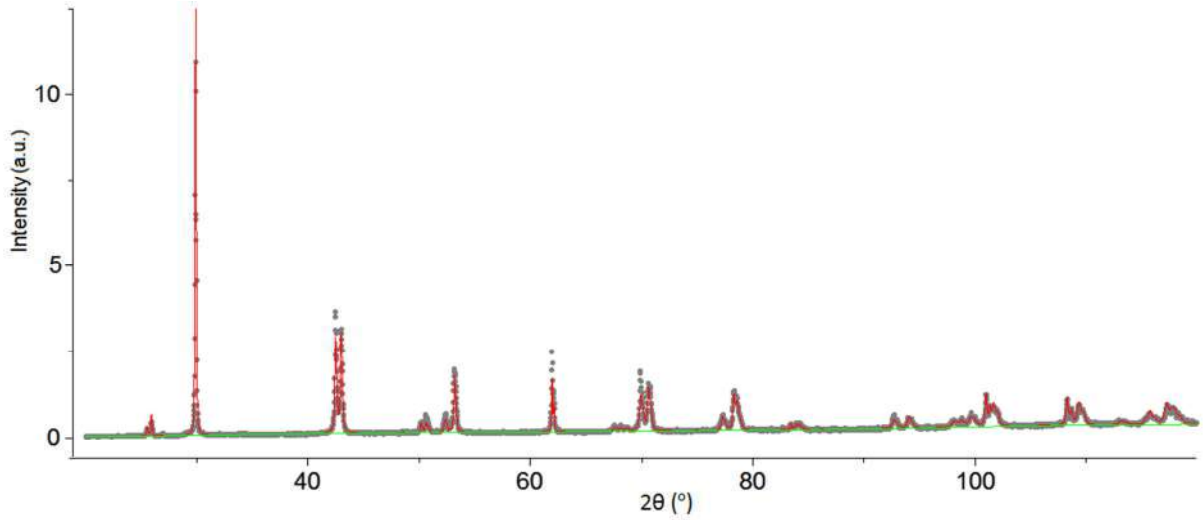


a = 4.26471(8)Å, α = 59.264(1)°

**Fig. 5.7.** X-ray diffraction of pure TAGS-85 + 1% Ho for Ge, sample-2. The gray dots correspond to the measured data points. The fitted curve is plotted in red. “a” is the lattice parameter, “α” is the rhombohedral angle.

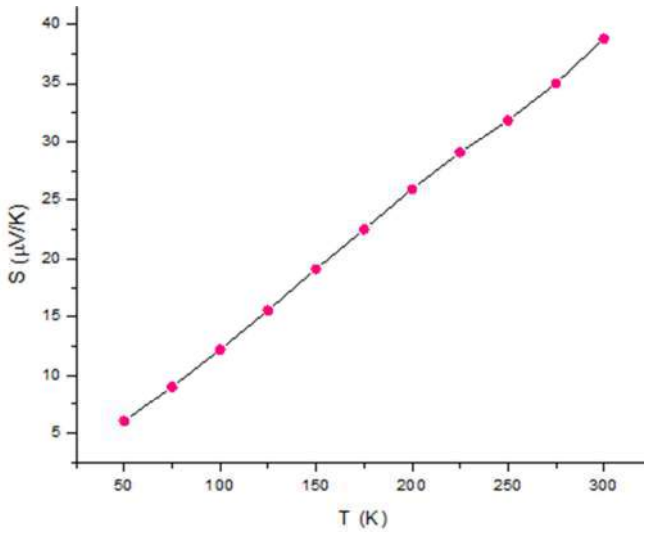


**Fig. 5.8.** Seebeck coefficient plotted against temperature for TAGS-85 + 1% Ho for Ge, sample-2.

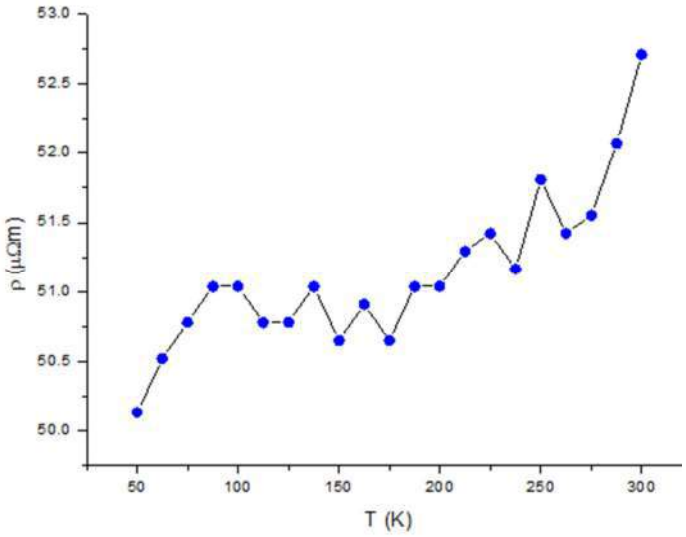


**Fig. 5.9.** Electrical resistivity of TAGS-85 + 1% Ho for Ge, sample-2 plotted against temperature.

# 5.2 TAGS-85 + 0.5% Ho for Ge

Chemical formula: $Te_{50}Ag_{6.52}Ge_{36.42}Sb_{6.52}Ho_{0.5}$

Molecular weight: 243.9215 amu

The details of the synthesis and characterization of the sample are the following:-

## i) Material Synthesis

Reaction temperature: 850$^{o}$C
Annealing temperature: 600$^{o}$C
Annealing time: 3 hours

## ii) X-ray Powder Diffraction

The X-ray powder diffraction showed that the sample contains only one phase and has a rhombohedral structure. The splitting of the (220) peak at $2\theta \approx 43^{o}$ is evident.

## iii) Seebeck Coefficient

The Seebeck coefficient was measured over 50K to 300K temperature range with a step of 25K without applying any magnetic field. The values and behavior are pretty much similar to that of the pure TAGS-85 (figure 4.3).

## iv) Electrical Resistivity

The electrical resistivity of the sample was measured over 50K to 300K temperature range with a step of 5K without applying any magnetic field. The IV-curves obtained for each temperature point were linear.

The room temperature value of electrical resistivity of this sample is almost the same as that of the pure TAGS-85 sample (figure 4.4). We also see a minimum in resistivity around T ≈ 250K. A good fit of the resistivity data below T = 250K to the equation 1.13 was obtained to be $\rho \approx 38.5 - 2.72 \ln (0.2\ T)$.

## v) Magnetic Response

Magnetic measurements were performed on small piece of the sample material weighing 28.5mg, over the temperature range of 5 to 300K. The magnetic susceptibility of the sample did not show any diamagnetic contribution below 300K. This means that the effect of the magnetic impurities dominates.

The effective magnetic moment of this sample was calculated to be $0.8\mu_B$. The atomic value of the magnetic moment of $Ho^{3+}$ ion is $10.4\mu_B$.

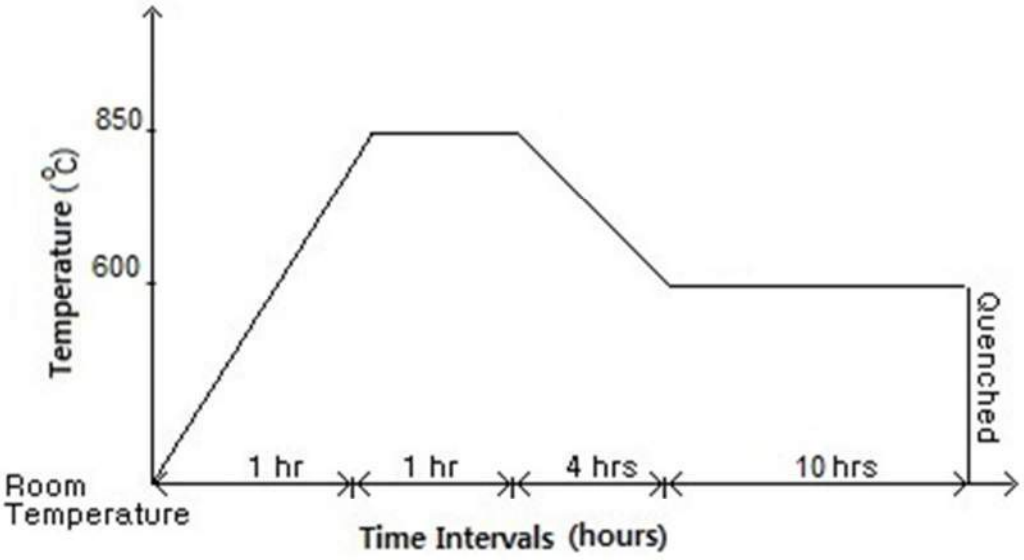


**Fig. 5.10.** Heat treatment plan for TAGS-85 + 0.5% Ho for Ge.

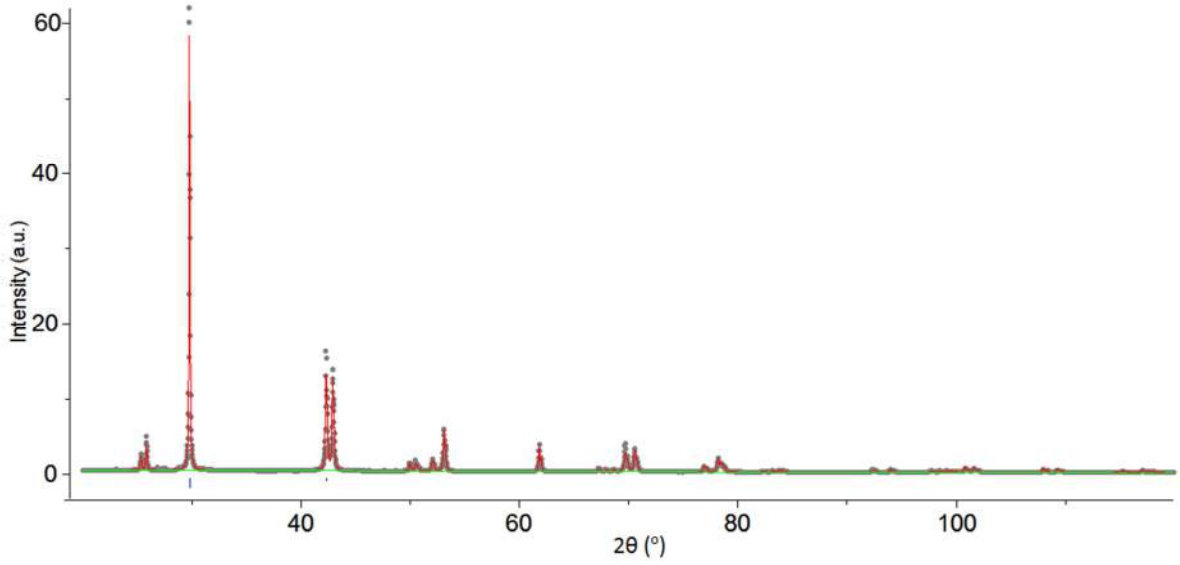


a = 4.27313(6)Å, α = 59.094(1)°

**Fig. 5.11.** X-ray diffraction of pure TAGS-85 + 1% Ho for Ge, sample-2. The gray dots correspond to the measured data points. The fitted curve is plotted in red. “a” is the lattice parameter, “α” is the rhombohedral angle.

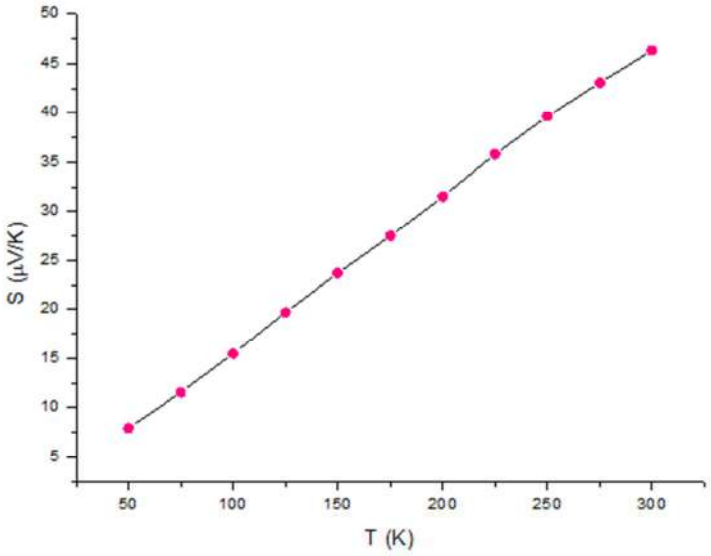


**Fig. 5.12.** Seebeck coefficient plotted against temperature for TAGS-85 + 1% Ho for Ge.

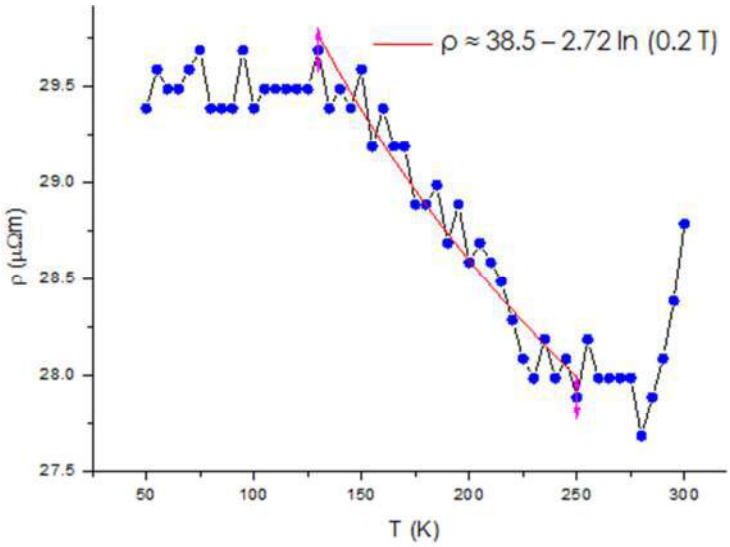


**Fig. 5.13.** Electrical resistivity of TAGS-85 + 0.5% Ho for Ge plotted against temperature.

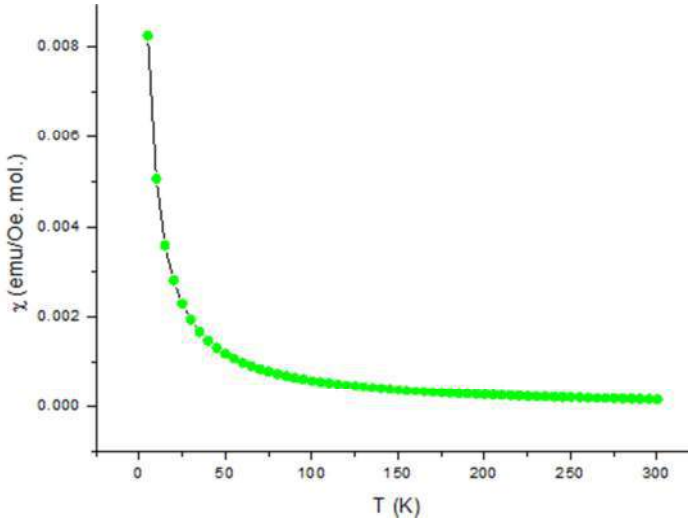


**Fig. 5.14.** Temperature dependence of the magnetic susceptibility of TAGS-85 + 0.5% Ho for Ge.

# 5.3 TAGS-85 + 1% Tb for Ge

Chemical formula: $Te_{50}Ag_{6.52}Ge_{35.92}Sb_{6.52}Tb_1$

Molecular weight: 244.7153 amu

The details of the synthesis and characterization of the samples are the following:-

## 5.3.1 Sample-1

### i) Material Synthesis

Reaction temperature: 850$^{o}$C
Annealing temperature: 600$^{o}$C
Annealing time: 14 hours

### ii) X-ray Powder Diffraction

The X-ray powder diffraction showed that the sample has a rhombohedral structure but contains few traces of $Ag_2Te$. The splitting of the (220) peak at $2\theta \approx 43^{o}$ is evident. The silver telluride impurity phase can be attributed to the deficiency of Ge which could have increased the probability of Te atoms reacting with Ag atoms to form telluride. The high intensity $Ag_2Te$ peaks appear at $2\theta \approx 31.2^{o}$, $38.8^{o}$, $39.25^{o}$ and $40.25^{o}$. The chances are high that the dopant atoms have gone to the Ag sites.

### iii) Seebeck Coefficient

The Seebeck coefficient was measured over 50K to 300K temperature range with a step of 25K without applying any magnetic field. The values of the Seebeck coefficient were almost four times that of the pure TAGS-85 (figure 4.3). Since this was a big breakthrough, the measurement was repeated after a couple of weeks and the Seebeck coefficient was observed to be three times higher than that for the pure TAGS-85 (figure-4.3). These values were not comparable with the first measurement. This observation raised questions about the reproducibility of the results. The measurement was repeated again and this time it reproduced the results of the second measurement. The measurement was performed on another pellet of the same sample, and the results agreed with those of the second and the third measurements.

### iv) Electrical Resistivity

The electrical resistivity of the sample was measured over 50K to 300K temperature range with a step of 5K without applying any magnetic field. The IV-curves obtained for each temperature point were linear.

The resistivity of this sample has no minimum. It keeps on increasing almost linearly. It is pretty higher than that of the pure TAGS-85 (figure 4.4). If we combine this result with the tripling of the Seebeck coefficient and compare them with the behavior of Tl doped PbTe discussed in section-1.3.5, we can say that there can be non-magnetic resonant levels in this sample. Although both the resistivity and the Seebeck coefficient are almost three times higher than the pure TAGS-85 values, the tripling of the Seebeck dominates since the electronic part of the figure of merit, i.e. the power factor, $S^2/\rho$, varies as the square of the Seebeck coefficient.

## v) Magnetic Response

Magnetic measurements were performed on small piece of the sample material weighing 31.5mg, over the temperature range of 5 to 300K. The magnetic susceptibility of the sample did not show any diamagnetic contribution below 300K.

The effective magnetic moment of the sample was calculated to be $0.616\mu_B$. The atomic value of the magnetic moment of $Tb^{3+}$ ion is $9.77\mu_B$.

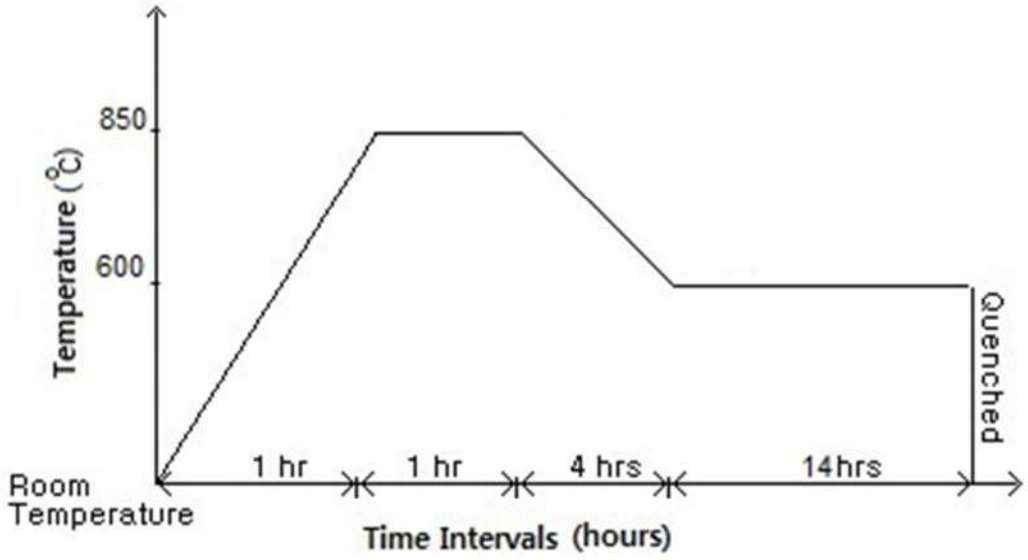


**Fig. 5.15.** Heat treatment plan for TAGS-85 + 1% Tb for Ge, sample-1.

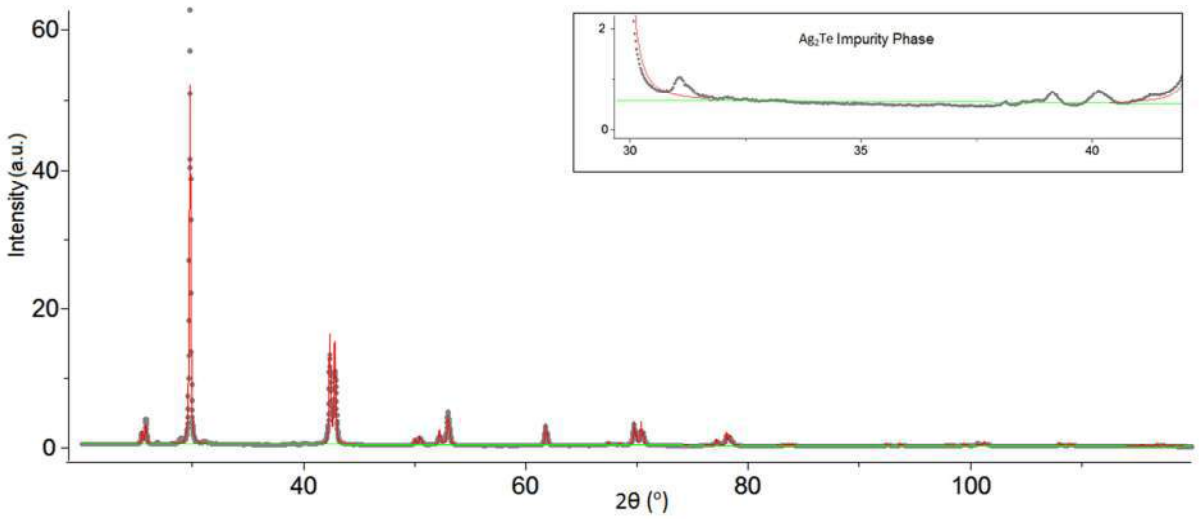


a = 4.26918(7)Å, α = 59.340(1)°

**Fig. 5.16.** X-ray diffraction of pure TAGS-85 + 1% Tb for Ge, sample-1. The gray dots correspond to the measured data points. "a" is the lattice parameter, "α" is the rhombohedral angle. The fitted curve is plotted in red. In the inset are some small peaks corresponding to the $Ag_2Te$ impurity phase.

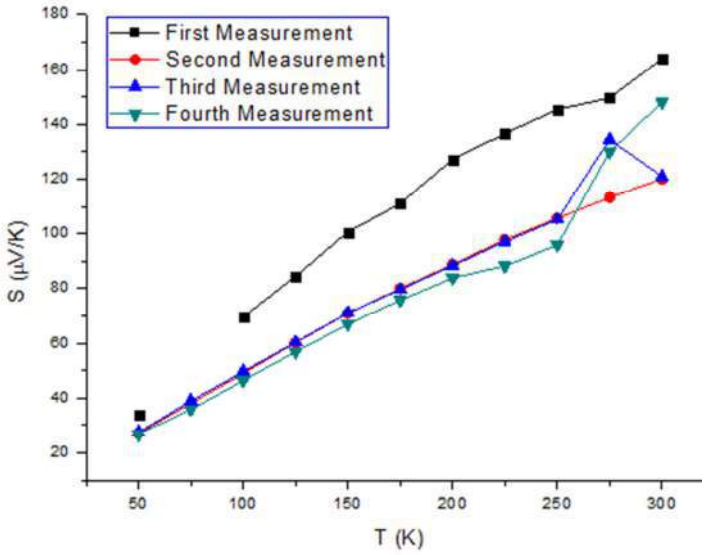


**Fig. 5.17.** Seebeck coefficient plotted against temperature for TAGS-85 + 1% Tb for Ge, sample-1.

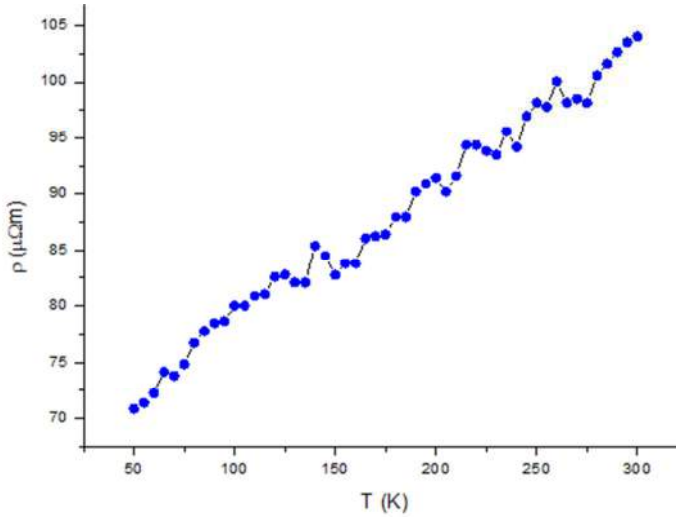


**Fig. 5.18.** Electrical resistivity of TAGS-85 + 1% Tb for Ge, sample-1 plotted against temperature.

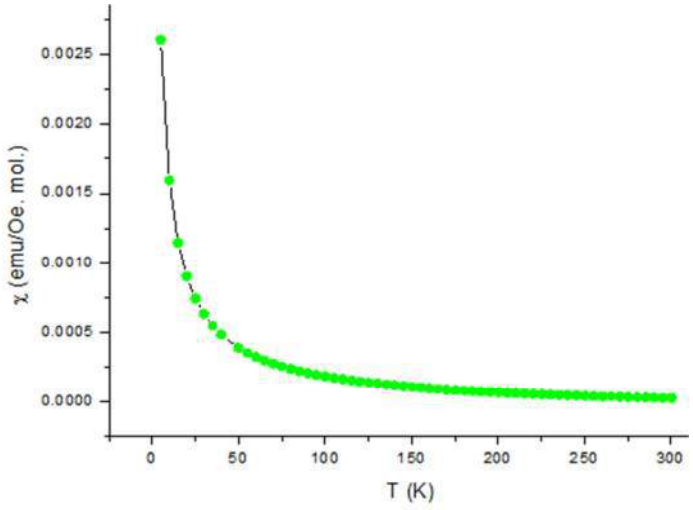


**Fig. 5.19.** Temperature dependence of the magnetic susceptibility of TAGS-85 + 1% Tb for Ge, sample-1.

## 5.3.2 Sample-2

### i) Material Synthesis

Reaction temperature: 850$^{o}$C
Annealing temperature: 600$^{o}$C
Annealing time: 3 hours

### ii) X-ray Powder Diffraction

The X-ray powder diffraction showed that the sample has a rhombohedral structure but also contains $Ag_2Te$ impurity phase. The peaks were quite broad, which means that the grain size is very small. The grain size was estimated to be around 13.2nm using the Scherrer formula. This can be an indication of absence of long range order in the lattice potential which can have interesting consequences. The splitting of the (220) peak at $2\theta \approx 43^{o}$ can be observed by zooming the plot. The existence of silver telluride impurity phase can be attributed to the deficiency of Ge which could have increased the probability of Te atoms reacting with Ag atoms to form telluride. The high intensity $Ag_2Te$ peaks appear at $2\theta \approx 31.2^{o}$, $38.8^{o}$, $39.25^{o}$ and $40.25^{o}$. The chances are high that the dopant atoms have gone to the Ag sites.

### iii) Seebeck Coefficient

The Seebeck coefficient was measured over 50K to 300K temperature range with a step of 25K without applying any magnetic field. The values of the Seebeck coefficient are one order of magnitude lower than that of the first sample (figure 5.17).

### iv) Electrical Resistivity

The electrical resistivity of the sample was measured over 50K to 300K temperature range with a step of 5K without applying any magnetic field. The IV-curves obtained for each temperature point were linear.

The resistivity values are also about one order of magnitude lower than those for the first sample (figure 5.18). This drop can be attributed to the broadening of the X-ray diffraction peaks, smaller grain size and increased number of vacancies and antiphase domains due to the much shorter annealing time.

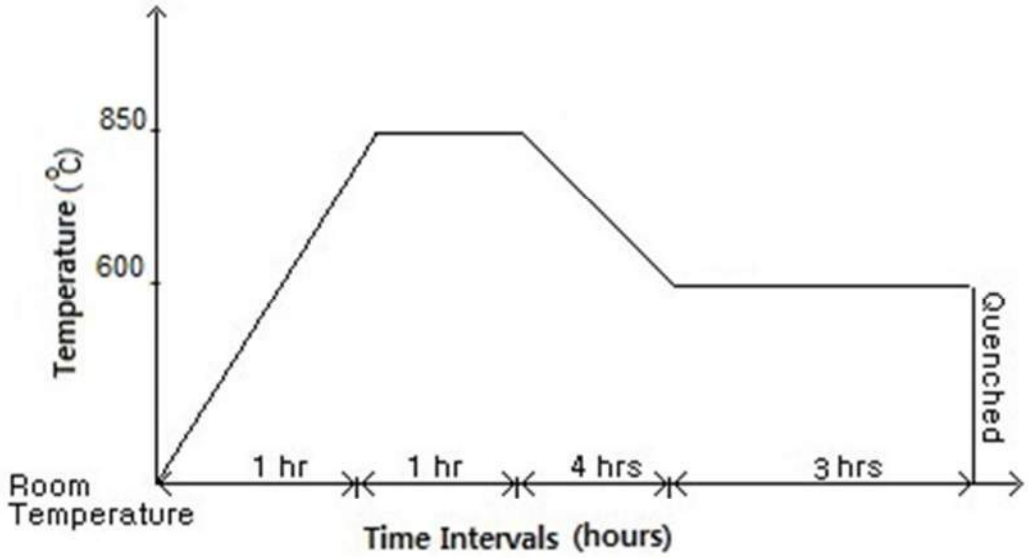


**Fig. 5.20.** Heat treatment plan for TAGS-85 + 1% Tb for Ge, sample-2.

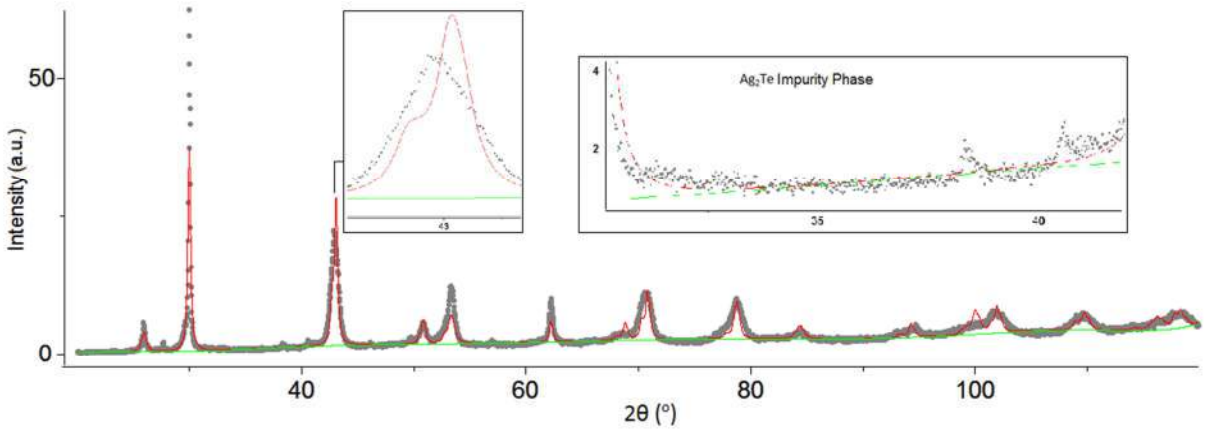


a = 4.24413(65)Å, α = 59.453(7)°

**Fig. 5.21.** X-ray diffraction of pure TAGS-85 + 1% Tb for Ge, sample-2. The gray dots correspond to the measured data points. "a" is the lattice parameter, "α" is the rhombohedral angle. The fitted curve is plotted in red. In the inset some small peaks corresponding to the $Ag_2Te$ impurity phase and the splitting of the (220) peak is shown.

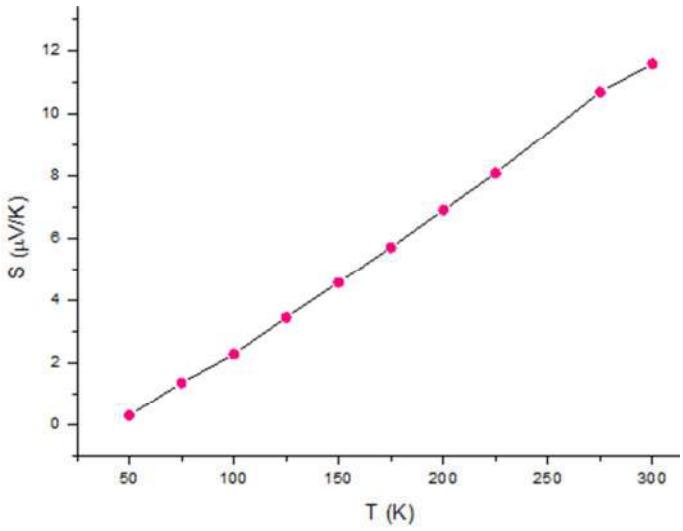


**Fig. 5.22.** Seebeck coefficient plotted against temperature for TAGS-85 + 1% Tb for Ge, sample-2.

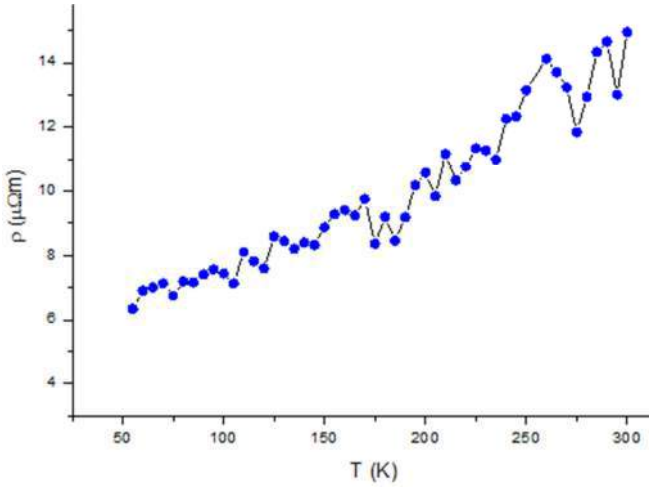


**Fig. 5.23.** Electrical resistivity of TAGS-85 + 1% Tb for Ge, sample-2 plotted against temperature.

## 5.3.3 Sample-3

### i) Material Synthesis

Reaction temperature: 850$^{o}$C
Annealing temperature: 600$^{o}$C
Annealing time: 3 hours

### ii) X-ray Powder Diffraction

The X-ray powder diffraction showed that the sample contains only one phase and has a rhombohedral structure. The splitting of the (220) peak at $2\theta \approx 43^{o}$ is evident.

### iii) Seebeck Coefficient

The Seebeck coefficient was measured over 50K to 300K temperature range with a step of 25K without applying any magnetic field. The Seebeck coefficient is almost double that of the pure TAGS-85 (figure 4.3).

### iv) Electrical Resistivity

The electrical resistivity of the sample was measured over 50K to 300K temperature range with a step of 5K without applying any magnetic field. The IV-curves obtained for each temperature point were linear.

Like the Seebeck coefficient, the electrical resistivity of this sample is also double that of the pure TAGS-85 sample (figure 4.4).

These results indicate that the 1% Tb substitution for Ge in TAGS-85 is the best candidate for further investigations and applications. The chances of having a sharp peak in the density of states near the Fermi level corresponding to the resonant states are high. The resonant states may come from the f-orbitals of Tb, as discussed for the case of Ce and Eu based alloys in section 2.3. The role played by the long annealing time is also crucial in the chemistry of this material. The high thermoelectric response of the first and the third sample can be attributed to the long annealing times. The third sample contained no impurity phases, but the first sample had traces of silver telluride grains, which indicates that substituting Tb for Ag may also result in improved thermoelectric efficiency.

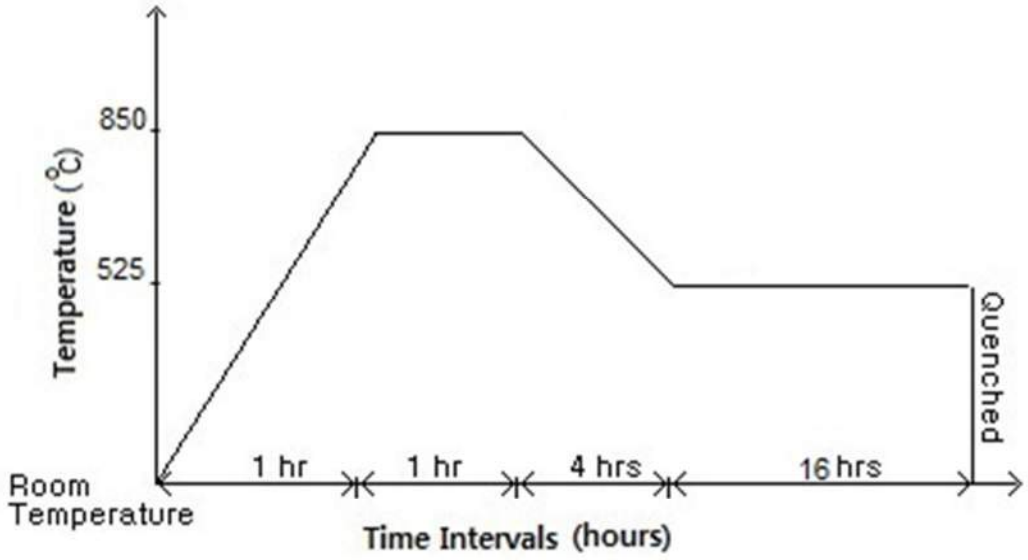


**Fig. 5.24.** Heat treatment plan for TAGS-85 + 1%Tb for Ge, sample-3.

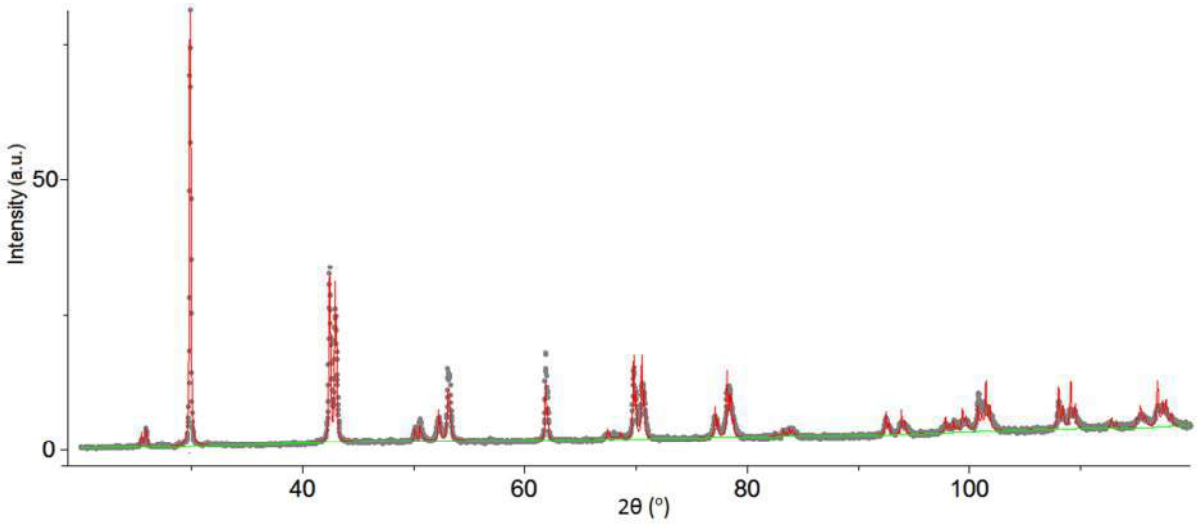


a = 4.27294(8)Å, α = 59.232(1)°

**Fig. 5.25.** X-ray diffraction of pure TAGS-85 + 1% Tb for Ge, sample-3. The gray dots correspond to the measured data points. The fitted curve is plotted in red. “a” is the lattice parameter, “α” is the rhombohedral angle.

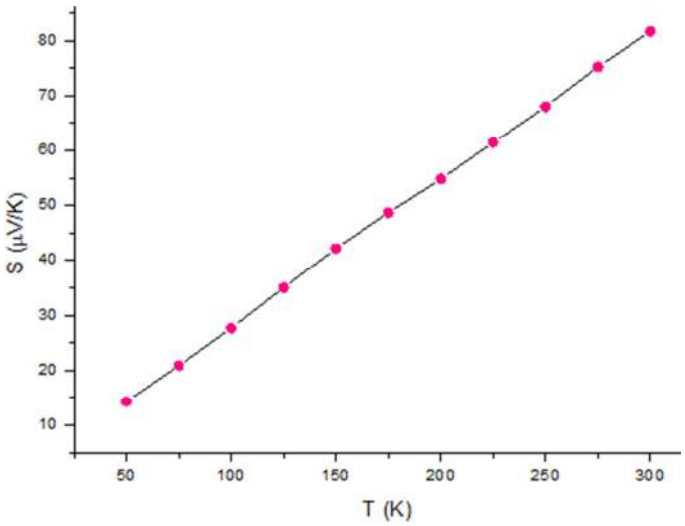


**Fig. 5.26.** Seebeck coefficient plotted against temperature for TAGS-85 + 1% Tb for Ge, sample-3.

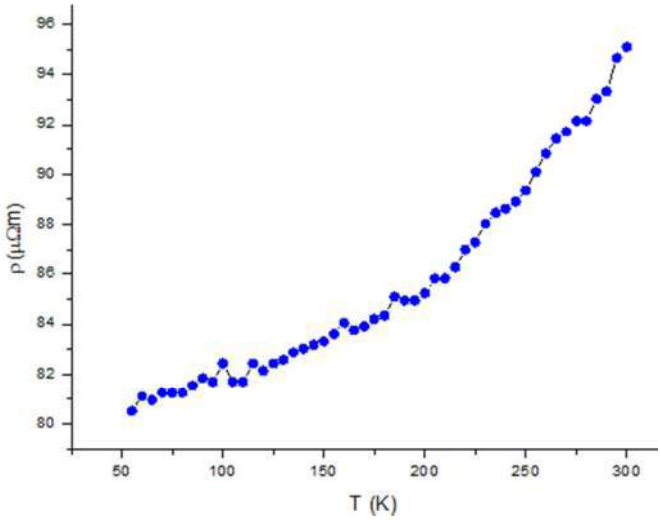


**Fig. 5.27.** Electrical resistivity of TAGS-85 + 1% Tb for Ge, sample-3 plotted against temperature.

# 5.4 TAGS-85 + 0.5% Tb for Ge

Chemical formula: $Te_{50}Ag_{6.52}Ge_{36.42}Sb_{6.52}Tb_{0.5}$

Molecular weight: 243.8515amu

The details of the synthesis and characterization of the samples are the following:-

## i) Material Synthesis

Reaction temperature: 850$^{o}$C
Annealing temperature: 600$^{o}$C
Annealing time: 3 hours

## ii) X-ray Powder Diffraction

The X-ray powder diffraction showed that the sample has a rhombohedral structure but contains few traces of $Ag_2Te$. The splitting of the (220) peak at $2\theta \approx 43^{o}$ is evident. The existence of silver telluride impurity can be attributed to the deficiency of Ge which could have increased the probability of Te atoms reacting with Ag atoms to form telluride. The high intensity $Ag_2Te$ peaks appear at $2\theta \approx 31.2^{o}$, $38.8^{o}$, $39.25^{o}$ and $40.25^{o}$. The chances are high that the dopant atoms have gone to the Ag sites.

## iii) Seebeck Coefficient

The Seebeck coefficient was measured over 50K to 300K temperature range with a step of 25K without applying any magnetic field. The values of the Seebeck coefficient were about 45% higher than that of the pure TAGS-85 (figure 4.3). The chances of a small peak in the density of states due to resonant levels can not be ruled out.

## iv) Electrical Resistivity

The electrical resistivity of the sample was measured over 50K to 300K temperature range with a step of 5K without applying any magnetic field. The IV-curves obtained for each temperature point were linear.

The electrical resistivity of this sample is of the same order of magnitude as that of the pure TAGS-85 sample (figure 4.4). There is no minimum in the resistivity and it increases with temperature.

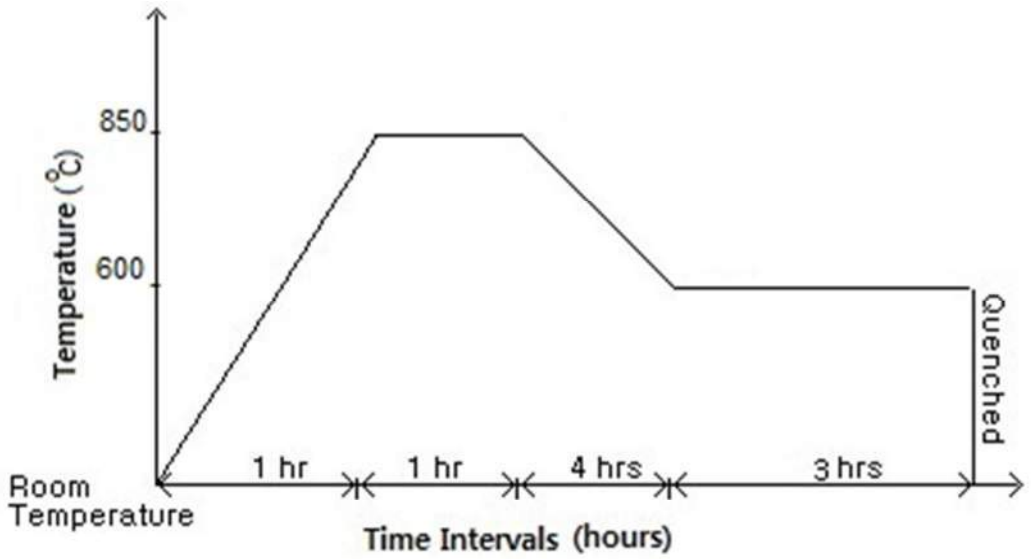


**Fig. 5.28.** Heat treatment plan for TAGS-85 + 0.5% Tb for Ge.

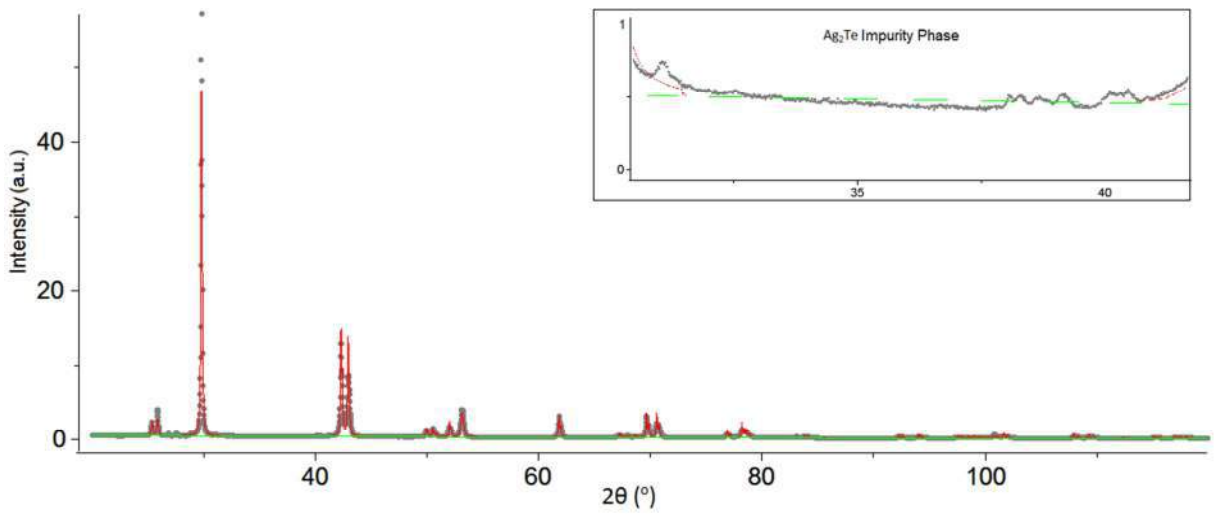


a = 4.27584(7)Å, α = 59.048(1)°

**Fig. 5.29.** X-ray diffraction of pure TAGS-85 + 0.5% Tb for Ge. The gray dots correspond to the measured data points. "a" is the lattice parameter, "α" is the rhombohedral angle. The fitted curve is plotted in red. In the inset are some small peaks corresponding to the $Ag_2Te$ impurity phase.

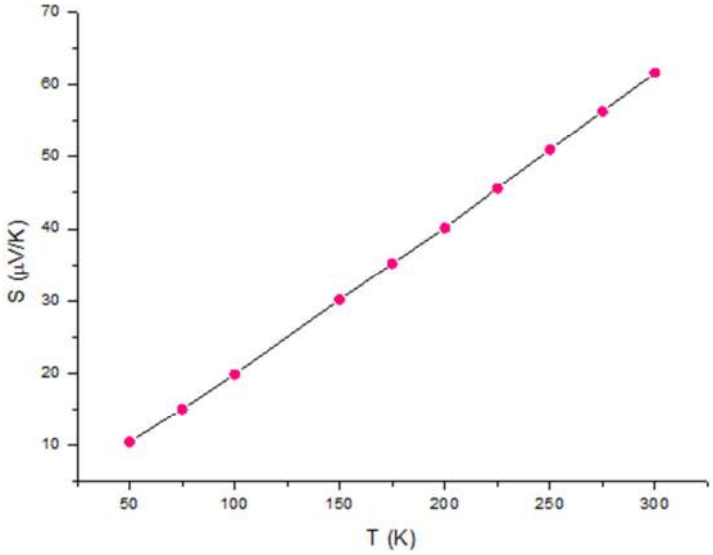


**Fig. 5.30.** Seebeck coefficient plotted against temperature for TAGS-85 + 0.5% Tb for Ge.

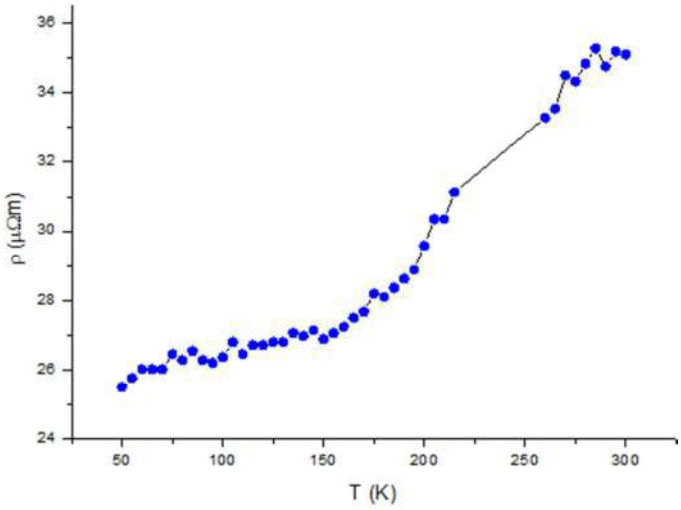


**Fig. 5.31.** Electrical resistivity of TAGS-85 + 0.5% Tb for Ge plotted against temperature.

Chapter–6

# Conclusions and Prospects

In this project the possibilities of improving the electrical part of the thermoelectric figure of merit of TAGS-85 have been explored. The material was doped with different molar concentrations of Holmium and Terbium. The dopants were substituted first for Terbium and then for Germanium. The thermoelectric power factor, PF = $S^2/\rho$, is a measure of the electrical part of the figure of merit (equation 1.5). Figure 6.1 compares the power factors of the pure TAGS-85 and the doped samples as measured in this project.

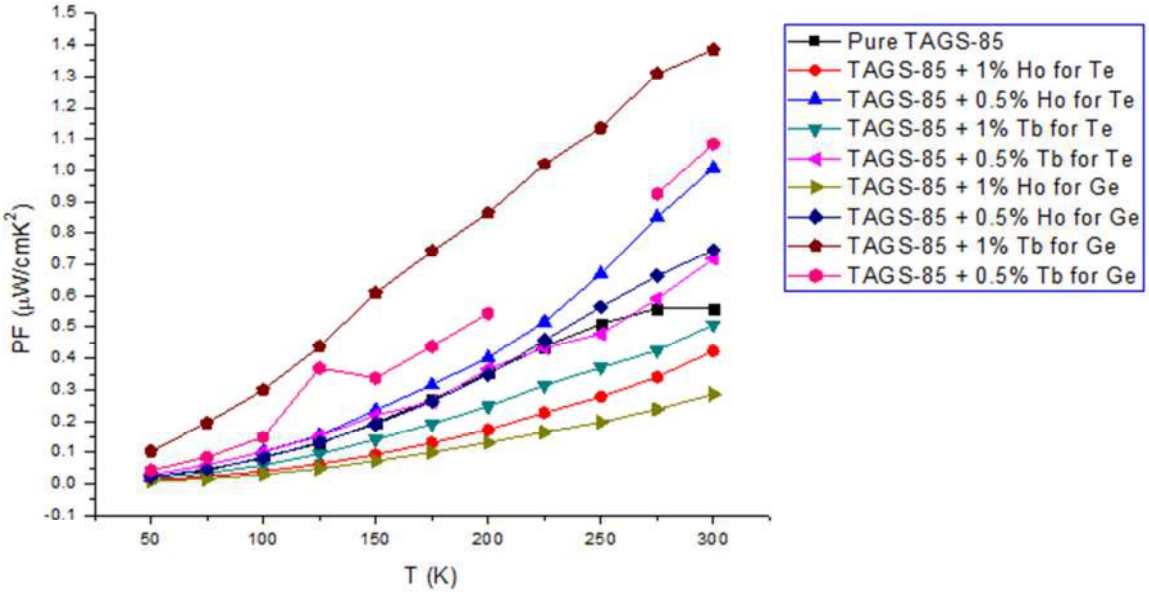


**Fig. 6.1.** Thermoelectric power factors, $S^2/\rho$, of pure and doped TAGS-85 samples plotted against temperature.

The power factor for the pure TAGS-85 sample is almost one order of magnitude less than the literature values (figure 2.9). This is because of some instrumental error in measuring the electrical resistivity, which appears in all of the measurements. The power factors of TAGS-85 + 1% Tb for Ge, annealed at 600$^{o}$C for 14 hours, seems to be almost three times higher than that of the pure TAGS-85 sample. This observation indicates that doping TAGS-85 with 1% Tb for Ge causes the distortion of the electronic density of states of the material as reported for the case of 2% Tl doped PbTe by Heremans et al. [39], a manifestation of Mahan and Sofo's model [40] of ideal thermoelectric materials described in section 1.3.5. There can be resonant levels coming from the f-states of the rare earth dopants. Keeping in view the differences in atomic masses of the dopants and the host, an improvement in the thermal part of the material is also expected.

Other samples of interest are TAGS-85 + 0.5% Tb for Te, TAGS-85 + 0.5% Tb for Ge and TAGS-85 + 0.5% Ho for Te for which almost a 100% increase of the power factor has been observed. It is suggested that for these samples and the 1% Tb for Ge doped sample, high temperature measurements be performed. Optical measurements for these samples can also help in understanding the physical origin of this enhancement. The resonant levels are supposed to give a sharp peak in the density of states, a few meV close to the Fermi energy. Once the peak position is identified, further improvements can be made by changing the doping concentration to shift the peak closer to the Fermi level.

Ab initio calculations have been very useful in predicting the Dirac delta function like peak of Mahan and Sofo in Tl-doped PbTe. For further research on TAGS-85, it is strongly recommended to do these calculations for the 1% Tb for Ge doped material. Knowing that this material contains traces of the $Ag_2Te$ impurity phase, it is also suggested that these calculations be performed for the 1% Tb for Ag doped TAGS-85. TAGS-85 + 0.5% Tb for Te, 0.5% Tb for Ge and 0.5% Ho for Te are also potential candidates for theoretical investigations.

A minimum in resistivity is observed for the pure TAGS-85, and 1% Ho for Te and 0.5% Ho for Ge doped TAGS-85. Below a certain temperature, the resistivity of these samples starts to increase. In the literature on TAGS, no structural transition has been reported to occur at low temperatures, so it doesn't seem to be a Peierls-distortion-type widening of the band gap. Also, the increment in the resistivity is very small, so one can not say that it is some kind of a metal-insulator transition, although the charge correlation effects can not be ignored completely. In the 0.5% Ho for Ge doped sample (section 5.2), a good fit of the resistivity data below T = 250K to the equation 1.13 was obtained to be $\rho \approx 38.5 - 2.72 \ln (0.2\ T)$. In the 1% Ho for Te doped sample (section 4.2), a good fit of the resistivity data below T = 245K to the equation 1.13 was obtained to be $\rho \approx 48 - 1.4 \ln (0.6\ T)$. This is a logarithmic increase which can be attributed to the anti-ferromagnetic interaction between the spins on the impurity sites and the ones in the conduction band, inducing the Kondo effect. For these materials, a local maxima in the Seebeck coefficient at the point of resistivity minimum was not observed, therefore it is hard to speak about the onset of Kondo effect at these temperatures. One can say that, at low temperatures, the scattering of charge carriers from the magnetic impurities increases. It is very unfortunate that the Hall effect measurements could not be performed in this project due to the time constraints. Those measurements could give further insights into the effects of doping the material with rare earths.

The chemistry of these materials seems to be very sensitive to the heat treatment. Although the highest power factors were obtained for the 1% Tb for Ge doped material when it was annealed for 14 hours, when another sample with the same stoichiometry was prepared with an annealing time of 3 hours, the enhancement of the power factor vanished (section 5.3.2). The XRD pattern of the material had very broad peaks and the grain size was estimated to be 13.2nm using the Scherrer formula. On the other hand, the XRD pattern of

the 1% Ho for Te sample annealed at 500$^{o}$C with a faster cooling rate and 3 hours annealing time showed signs of quenchability of the high temperature cubic phase which has never been reported in the literature so far (section 4.2.2).

In table 6.1, a summary of the lattice parameters and the values of the physical properties measured at room temperature is presented.

| Material | a(Å) | α | $\mu_{eff}$ ($\mu_B$) | ρ (μΩm) | S (μV/K) |
|---|---|---|---|---|---|
| Pure TAGS-85 | 4.27668(8) | 59.077(1)$^{o}$ | - | 28.806 | 40.17 |
| TAGS-85 + 1% Ho for Te (Sample-1) | 4.2776(2) | 58.904(3)$^{o}$ | 1.06 | 46.481 | 44.34 |
| TAGS-85 + 1% Ho for Te (Sample-2) | 4.27655(2) | 58.979(0)$^{o}$ | - | - | - |
| TAGS-85 + 0.5% Ho for Te | 4.27314(9) | 59.088(1)$^{o}$ | 0.680 | 47.250 | 68.96 |
| TAGS-85 + 1% Tb for Te (Sample-1) | 4.2804(1) | 58.930(2)$^{o}$ | 3.00 | 66.614 | 58.12 |
| TAGS-85 + 1% Tb for Te (Sample-2) | 4.27569(23) | 59.093(3)$^{o}$ | - | - | - |
| TAGS-85 + 1% Tb for Te (Sample-3) | 4.2736(6) | 59.125(7)$^{o}$ | - | - | - |
| TAGS-85 + 0.5% Tb for Te | 4.27389(6) | 59.135(1)$^{o}$ | 0.420 | 63.612 | 67.55 |
| TAGS-85 + 1% Ho for Ge (Sample-1) | 4.27218(15) | 59.190(1)$^{o}$ | 1.93 | 63.510 | 45.84 |
| TAGS-85 + 1% Ho for Ge (Sample-2) | 4.26471(8) | 59.264(1)$^{o}$ | - | 52.714 | 38.76 |
| TAGS-85 + 0.5% Ho for Ge | 4.27313(6) | 59.094(1)$^{o}$ | 0.800 | 28.786 | 46.32 |
| TAGS-85 + 1% Tb for Ge (Sample-1) | 4.26918(7) | 59.340(1)$^{o}$ | 0.616 | 104.03 | 120.04 |
| TAGS-85 + 1% Tb for Ge (Sample-2) | 4.24413(65) | 59.453(7)$^{o}$ | - | 14.948 | 11.60 |
| TAGS-85 + 1% Tb for Ge (Sample-3) | 4.27294(8) | 59.232(1)$^{o}$ | - | 81.650 | 95.09 |
| TAGS-85 + 0.5% Tb for Ge | 4.27584(7) | 59.048(1)$^{o}$ | - | 35.114 | 61.70 |

**Table 6.1**. A summary of the lattice parameters and the room temperature physical properties as measured in this project.

# References


[1] MEMS Caltech, Semiconductor Sensors and Actuators Course - EE40, Thermoelectric Notes.

[2] Seebeck, T. J., Magnetic polarization of metals and minerals, Abhandlungen der Deutschen Akademie der Wissenschafren zu Berlin, 265, (1822-1823).

[3] Peltier, J. C., Nouvelles experiences sur la caloricite des courans electrique, Ann. Chim., LVl 371, (1834).

[4] Altenkirch, E., Uber den Nutzeffeckt der Thermosaule, Physikalische Zeitschrifr, 10, 560, (1909).

[5] Altenkirch, E., Electrothermische Kalteerzeugung und Reversible Electrische Heizung, Physikalische Zeitschrifr, 12, 920, (191 1).

[6] Snyder, G. J. and Toberer, E. S., Complex thermoelectric materials, Nat. Materials, 7, 105-114 (2008).

[7] Ioffe, A. F., Physics of semiconductors, Academic Press Inc., New York (1960).

[8] Kasap, S., Thermoelectric effects in metals: thermocouples, (2001).

[9] Telks, M., The efficiency of thermoelectric generators, Int. J. Appl. Phys., 18, 1116, (1947).

[10] Ioffe, A. F., Airapetyants, S. V., Ioffe, A. V., Kolomoets, N. V., and Stilbans, L. S., On increasing the efficiency of semiconducting thermocouples, Dokl. Akad. Nauk SSSR, 106, 931, (1956).

[11] Hicks, L. D. and Dresselhaus, M. S., Phys. Rev. B: Condens. Matter, 47, 12727–12731, (1993).

[12] Rowe, D. M. & Min, G. Alpha-plot in sigma-plot as a thermoelectric-material performance indicator. J. Mater. Sci. Lett. 14,617–619 (1995).

[13] He, J., Kanatzidis, M. G., Dravid, V. P., High performance bulk thermoelectrics via a panoscopic approach, Materials Today, 16, 166-176, (2013).

[14] Bhandari, C. M. & Rowe, D. M. in CRC Handbook of Thermoelectrics (ed. Rowe, D. M.) Ch. 5, 43–53 (CRC, Boca Raton, 1995).

[15] Kittel, C., Introduction to Solid State Physics, John Wiley & Sons, USA, (2005).

[16] Corrosion online lectures - ME303L02.

[17] Skrabek, E. A. & Trimmer, D. S. in CRC Handbook of Thermoelectrics (ed. Rowe, D. M.) 267–275 (CRC, Boca Raton, 1995).

[18] Nolas, G. S., Poon, J. & Kanatzidis, M. Recent developments in bulk thermoelectric materials. Mater. Res. Soc. Bull. 31,199–205 (2006).

[19] Yao, T. Thermal-Properties of AlAs/GaAs Superlattices. Appl. Phys. Lett. 51, 1798–1800 (1987).

[20] Caylor, J. C., Coonley, K., Stuart, J., Colpitts, T. & Venkatasubramanian, R. Enhanced thermoelectric performance in PbTe-based superlattice structures from reduction of lattice thermal conductivity. Appl. Phys. Lett. 87, 23105 (2005).

[21] Hochbaum, A. I. et al. Enhanced thermoelectric performance of rough silicon nanowires. Nature 451,163–167 (2008).

[22] Boukai, A. I. et al. Silicon nanowires as efficient thermoelectric materials. Nature 451,168–171 (2008).

[23] Cahill, D. G., Watson, S. K. & Pohl, R. O. Lower limit to thermal conductivity of disordered crystals. Phys. Rev. B 46, 6131–40 (1992).

[24] Fox, M., Optical Properties of Solids, Oxford University Press, (2001).

[25] Vaqueiro, P. et al. Recent developments in nanostructured materials for high-performance thermoelectrics. J. Mater. Chem., 20, 9577-9584, (2010).

[26] Henry, A. S. and Chen, G., J. Comput. Theor. Nanosci., 5, 141–152, (2008).

[27] Kanatzidis, M. G., Chem. Mater., 22, 648–659, (2010).

[28] Sootsman, J.R., Pcionek, R. J., Kong, H. J., Uher, C., Kanatzidis, M. G., Strong reduction of thermal conductivity in nanostructured PbTe prepared by matrix encapsulation, Chem. Mater., 18(21), 4993-4995, (2006).
[29] Bux, S. K., Blair, R. G., Gogna, P. K., Lee, H., Chen, G., Dresselhaus, M. S., Kaner, R. B., and Fleurial, J. P., Adv. Funct. Mater.,19, 2445–2452, (2009).
[30] Brown, S. R., Kauzlarich, S. M., Gascoin, F. & Snyder, G. J. $Yb_{14}MnSb_{11}$: New high efficiency thermoelectric material for power generation. Chem. Mater. 18, 1873–1877 (2006).
[31] Fleurial, J.-P., Caillat, T. & Borshchevsky, A. in Proc. ICT'97 16th Int. Conf. Thermoelectrics1–11 (IEEE Piscataway, New Jersey, 1997).
[32] Toberer, E. S., Christensen, M., Iversen, B. B. & Snyder, G. J. High temperature thermoelectric efficiency in $Ba_8Ga_{16}Ge_{30}$. Phys. Rev. B.
[33] Kurosaki, K., Kosuga, A., Muta, H., Uno, M. & Yamanaka, S. $Ag_9TlTe_5$: A high-performance thermoelectric bulk material with extremely low thermal conductivity. Appl. Phys. Lett. 87, 061919, (2005).
[34] Nolas, G. S., Poon, J. & Kanatzidis, M. Recent developments in bulk thermoelectric materials. Mater. Res. Soc. Bull. 31, 199–205 (2006).
[35] Chung, D. Y., Hogen, T., Brazis, P., Rocci-Lane, M., Ireland, J. R., Kannewurf, C. R., Bastea, M., Uher, C. and Kanatzidis, M. G., J. Am. Chem. Soc. 126, 6414, (2004).
[36] Terasaki, I., Sasago, Y. & Uchinokura, K. Large thermoelectric power in $NaCo_2O_4$ single crystals. Phys. Rev.B 56, 12685–12687 (1997).
[37] Gascoin, F., Ottensmann, S., Stark, D., Haile, S. M. & Snyder, G. J. Zintl phases as thermoelectric materials: Tuned transport properties of the compounds $Ca_xYb_{1-x}Zn_2Sb_2$. Adv. Funct. Mater. 15, 1860–1864 (2005).
[38] Slack, G. A., New Materials and Performance Limits for Thermoelectric Cooling, in CRC Handbook of Thermoelectrics, ed. D. M. Rowe, CRC Press LLC, Boca Raton, FL, p. 407, (1995).
[39] Heremans, J. P., Jovovic, V., Toberer E. S., Saramat, A., Kurosaki, K., Charoenphakdee, A., Yamanaka, S., Snyder G. J. Enhancement of thermoelectric efficiency in PbTe by distortion of the electronic density of states. Science, 321, 554-557, (2008).
[40] Mahan, G.D. and Sofo, J.O., The best thermoelectric. Proc. Natl. Acad. Sci. USA, 93, 7436-7439, (1996).
[41] Jaworski, C. M., Kulbachinskii, V., and Heremans, J. P., Phys. Rev. B: Condens. Matter Mater. Phys., 80, 233201, (2009).
[42] Heremans, J. P., Wiendlocha, B., Chamoire, A. M. Resonant levels in bulk thermoelectric semiconductors. Energy Environ. Sci., 5, 5510-5530, (2012).
[43] Falkov'skii, L. A., Sov. Phys. JETP, 41, 767, (1976).
[44] Kaidanov, V. I., Nemov, S. A., Parfenév, R. V., Shamshur, D. V., Effect of additional doping with an acceptor impurity on the superconducting transition in PbTe <Tl>, JEPT Lett., 35, 12, (1982).
[45] Fritts, R. W., in Thermoelectric Materials and Devices, Eds. Cadoff, I. B. and Miller, E., (Reinhold, New York, 1960), pp. 143–162.
[46] Ahmad, S., Mahanti, S. D., Hoang, K., and Kanatzidis, M. G., Phys. Rev. B: Condens. Matter Mater. Phys., 74, 155205, (2006).
[47] Ramaneti, R., Lodder, J. C., Jansen, R., Kondo effect and impurity band conduction in $Co:TiO_2$ magnetic semiconductor, Phy. Rev. B, 76, 195207 (2007).
[48] Daybell, M. D. and Steyert, W. A. Rev. Mod. Phys., 40, 380, (1968).
[49] Heeger, A.J. Localized moments and nonmoments in metals, in Solid State Physics, ed. Seitz, F., Turnbull, D. and Ehrenreich, H., Academic Press, New York, vol. 23, p. 284, (1969).
[50] Skrabek, E. A., Electron beam microanalysis of microconstituent phases in Te-Ge-Sb-Ag Alloys, Report AMR-2024, Advanced Metals Research Corp., July 1965.
[51] Snykers, M., Delavignette, P., Amelinckx, S., Mat. Res. Bull, 7, 831–839, (1972).
[52] Abrikosov, N. K., Dimitrova, S. K., Karpinskii, O. G., Plachkova, S. K., and Shelimova, L. E., Phase transitions and electrical properties of solid solutions on the base of GeTe across $GeTe-AgSbTe_2$ cross section, Inorg. Mater., 20, 42, (1984).

[53] Cook, B. A., Kramer, M. J., Wei, X., Harringa, J. L., Nature of the cubic to rhombohedral structural transformation in $(AgSbTe_2)_{15}(GeTe)_{85}$ thermoelectric material, J. Appl. Phy, 101, 053715, (2007).
[54] Yang, S. H., Zhu, T. J., Sun, T., He, J., Zhang, S. N., Zhao, X. B., Nanostructures in high-performance $(GeTe)_x(AgSbTe_2)_{100-x}$ thermoelectric materials, Nanotechnology, 19, 245707, (2008).
[55] Zhu, T., Gao, H., Chen, Y., Zhao, X., Ioffe-Regel limit and lattice thermal conductivity reduction of high performance $(AgSbTe_2)_{15}(GeTe)_{85}$ thermoelectric materials, J. Mater. Chemistry A, 2, 3251-3256, (2014).
[56] Bredl, C. D., Horn S., Steglich, F., Luthi, B., Martin R. M., Low temperature specific heat of CeCu2Si2 and CeAl3: Choerence effects in Kondo lattice systems, Phys. Rev. Lett. 52, 1982, (1984).
[57] Steglich, F., Bredl, C. D., Lieke, W., Rauchschwalbe, U., Sparn, G., Heavy fermion superconductivity, Phys. Rev. Lett., 126B, 82-91, (1984).
[58] Levin, E. M., Kuzhel, B. S., Bodak, O. I., Belan, B. D., Stets, I. N., Concentrated Kondo systems in solid solutions on the base of Europium ternary compounds, Phys. Stat. Sol. (b) 161, 783-795, (1990).
[59] Levin, E. M., Cook, B. A., Harringa, J. L., Budko, S. L., Venkatasubramanian, R., Schmidt-Rohr, K., Analysis of Ce- and Yb- doped TAGS-85 materials with enhanced thermoelectric figure of merit, Adv. Fun. Mater., 21, 441-447, (2011).
[60] Levin, E. M., Budko, S. L., Schmidt, K., Enhancement of thermopower of TAGS-85 high-performance thermoelectric material by doping with the rare earth Dy, Adv. Fun. Mater., 22, 2766-2774, (2012).
[61] Hoang, K., Mahanti, S. D., Kanatzidis, M. G., Impurity clustring and impurity-induced bands in PbTe-, SnTe-, and GeTe-based bulk thermoelectrics, Phy. Rev. B., 81, 115106, (2010).
[62] Harrison, W. A., Elementary Electronic Stucture, World Scientific, Singapore, (2004).
[63] Magnetic Properties Measurement System: Reciprocating Sample Option User's Manual Part Number 1090-100C, Quantum Design, (2001).
[64] Bain, G. A., Berry, J. F., Diamagnetic corrections and Pascal's constants, J. Chem. Edu., 85, 532-536, (2008).
[65] Miller, R. C., Thermoelectricity: Science and Engineering, pp. 434-439, Interscience, New York, (1961).
[66] Damon, D. H., Lubell, M. S., Mazelsky, R., Nature of defects in germanium telluride, J. Phys. Chem. Solids, 28, 520-522, (1966).

# Acknowledgements

First and foremost, I would like to thank my supervisor Dr. Graeme Blake for all his guidance, encouragement and freedom that he provided during the year of master thesis research. I benefitted a lot from his knowledge and insight. I would also like to thank Anil Kumar, Lei Liang, Ngo Truong Mai, Aisha Aqeel, Guowei Li, Laaya Shabaani and Saeedeh Farokhipur for fruitful discussions and Jacob Baas for his technical support. I am also greatly thankful to Dr. Ron Tobey for refereeing my thesis. My special thanks go to all of my class fellows who made my stay at Groningen a pleasant memory of my life. I am proud of being a part of the multidisciplinary Top Master Nanoscience program of the Zernike Institute for Advanced Materials which has added a lot to my knowledge of physics and chemistry and I also acknowledge its financial support.